

**AFRL-SN-RS-TR-2006-343**  
**Final Technical Report**  
**December 2006**



# **LOW-COST, HIGH-PERFORMANCE ANALOG OPTICAL LINKS**

**Photonic Systems, Inc.**

**Sponsored by**  
**Defense Advanced Research Projects Agency**  
**DARPA Order No. AOJ811**

*APPROVED FOR PUBLIC RELEASE; DISTRIBUTION UNLIMITED.*

**STINFO COPY**

The views and conclusions contained in this document are those of the authors and should not be interpreted as necessarily representing the official policies, either expressed or implied, of the Defense Advanced Research Projects Agency or the U.S. Government.

**AIR FORCE RESEARCH LABORATORY**  
**SENSORS DIRECTORATE**  
**ROME RESEARCH SITE**  
**ROME, NEW YORK**

## **NOTICE AND SIGNATURE PAGE**

Using Government drawings, specifications, or other data included in this document for any purpose other than Government procurement does not in any way obligate the U.S. Government. The fact that the Government formulated or supplied the drawings, specifications, or other data does not license the holder or any other person or corporation; or convey any rights or permission to manufacture, use, or sell any patented invention that may relate to them.

This report was cleared for public release by the Air Force Research Laboratory Rome Research Site Public Affairs Office and is available to the general public, including foreign nationals. Copies may be obtained from the Defense Technical Information Center (DTIC) (<http://www.dtic.mil>).

AFRL-SN-RS-TR-2006-343 HAS BEEN REVIEWED AND IS APPROVED FOR PUBLICATION IN ACCORDANCE WITH ASSIGNED DISTRIBUTION STATEMENT.

FOR THE DIRECTOR:

/s/

JAMES R. HUNTER  
Work Unit Manager

/s/

RICHARD G. SHAUGHNESSY  
Chief, Rome Operations Site  
Sensors Directorate

This report is published in the interest of scientific and technical information exchange, and its publication does not constitute the Government's approval or disapproval of its ideas or findings.

<b>REPORT DOCUMENTATION PAGE</b>				<i>Form Approved</i> <b>OMB No. 0704-0188</b>	
<small>Public reporting burden for this collection of information is estimated to average 1 hour per response, including the time for reviewing instructions, searching data sources, gathering and maintaining the data needed, and completing and reviewing the collection of information. Send comments regarding this burden estimate or any other aspect of this collection of information, including suggestions for reducing this burden to Washington Headquarters Service, Directorate for Information Operations and Reports, 1215 Jefferson Davis Highway, Suite 1204, Arlington, VA 22202-4302, and to the Office of Management and Budget, Paperwork Reduction Project (0704-0188) Washington, DC 20503.</small>					
<b>PLEASE DO NOT RETURN YOUR FORM TO THE ABOVE ADDRESS.</b>					
<b>1. REPORT DATE (DD-MM-YYYY)</b> DEC 06		<b>2. REPORT TYPE</b> Final		<b>3. DATES COVERED (From - To)</b> Jul 00 – Sep 06	
<b>4. TITLE AND SUBTITLE</b> LOW-COST, HIGH-PERFORMANCE ANALOG OPTICAL LINKS				<b>5a. CONTRACT NUMBER</b> F30602-00-C-0128	
				<b>5b. GRANT NUMBER</b>	
				<b>5c. PROGRAM ELEMENT NUMBER</b> 63739E	
<b>6. AUTHOR(S)</b> Joelle Prince, William Burns, Edward Ackerman, Charles Cox, Harold Roussell, Frank Makrides, Michael Regan				<b>5d. PROJECT NUMBER</b> J811	
				<b>5e. TASK NUMBER</b> 00	
				<b>5f. WORK UNIT NUMBER</b> 02	
<b>7. PERFORMING ORGANIZATION NAME(S) AND ADDRESS(ES)</b> Photonic Systems, Inc. 900 Middlesex Turnpike, Bldg #5 Billerica Massachusetts 01821				<b>8. PERFORMING ORGANIZATION REPORT NUMBER</b> N/A	
<b>9. SPONSORING/MONITORING AGENCY NAME(S) AND ADDRESS(ES)</b> Defense Advanced Research Projects Agency AFRL/SNDP 3701 North Fairfax Drive 25 Electronic Parkway Arlington Virginia 22203-1714 Rome New York 13441-4515				<b>10. SPONSOR/MONITOR'S ACRONYM(S)</b>	
				<b>11. SPONSORING/MONITORING AGENCY REPORT NUMBER</b> AFRL-SN-RS-TR-2006-343	
<b>12. DISTRIBUTION AVAILABILITY STATEMENT</b> APPROVED FOR PUBLIC RELEASE; DISTRIBUTION UNLIMITED. PA#06-780					
<b>13. SUPPLEMENTARY NOTES</b>					
<b>14. ABSTRACT</b> Photonic Systems, Inc. pursued the goal stated in the RFLICs BAA (“...achieving a V <sub>pi</sub> in the range of 0.1 to 0.5 Volts [to enable a link having] zero RF insertion loss with 1 – 10 mW of optical power available from conventional laser diode sources”) on two parallel development paths. Collaborating with Sarnoff Corporation, Photonic Systems developed a Bipolar Cascade Laser that achieved a slope efficiency of 0.5 W/A by forcing the link’s input RF signal to feed a series-connected succession of multiple laser junctions whose optical outputs are collected in parallel to illuminate the link’s single photodetector. Additionally, Photonic Systems developed a Broad Bandwidth Resonant Modulator, in which two low-loss optical resonators act as a lever to reduce the effective V <sub>pi</sub> by 25% for a V <sub>pi</sub> =2.7V of the interferometric optical intensity modulator process relative to the V <sub>pi</sub> of the optical phase modulator embedded within the two resonators.					
<b>15. SUBJECT TERMS</b> Analog, Fiber, Link, External modulation, direct modulation					
<b>16. SECURITY CLASSIFICATION OF:</b>			<b>17. LIMITATION OF ABSTRACT</b>  UL	<b>18. NUMBER OF PAGES</b>  120	<b>19a. NAME OF RESPONSIBLE PERSON</b> James R. Hunter
a. REPORT U	b. ABSTRACT U	c. THIS PAGE U			<b>19b. TELEPHONE NUMBER (Include area code)</b>

## Table of Contents

1	Summary .....	1
2	Direct Modulation .....	2
2.1	Introduction .....	2
2.2	Methodology and Results: Team I - PSI, MIT and Sarnoff.....	6
	Tunnel junction design – IV model .....	6
	Laser design and characterization .....	9
	Resonant enhanced laser for greater modulation bandwidth .....	9
	Noise .....	13
	Fiber coupling .....	19
2.3	Methodology and Results: Team II - PSI and Sarnoff.....	25
	Iteration 1 .....	25
	Tunnel junction design and growth.....	25
	Laser design and characterization .....	27
	Iteration 2 .....	30
	Tunnel junction design and growth.....	31
	Laser design and characterization .....	32
	Threshold current variation with temperature.....	34
	Highest slope efficiency region .....	35
	Laser RF frequency output.....	39
	Spectral and far field measurements .....	42
	Leakage current investigations .....	44
	High threshold investigations .....	45
	Iteration 3 .....	46
	Tunnel junction design and growth – reduction of leakage current.....	46
	Laser design and characterization .....	47
	Broad area lasers .....	47
	Ridge waveguide lasers.....	48
	Iteration 4 .....	51
	Laser design and characterization .....	51
	Optimization of bipolar cascade laser .....	51
	Frequency performance of cascade laser .....	52
2.4	Conclusions.....	56
3	External Modulation .....	57
3.1	Introduction .....	57
3.2	Electro-optic Materials.....	58
	Mode conversion modulator in thin high r-coefficient material .....	58
	Fabrication of channel waveguides in BaTiO <sub>3</sub> .....	58
	Formation of electrodes on BaTiO <sub>3</sub> .....	59

Measurement of the microwave properties of BaTiO <sub>3</sub> .....	60
Thin lithium niobate material process development for Mach-Zehnder modulator .....	60
Materials investigation ended .....	61
3.3    External Modulation Techniques .....	62
Vertical Fabry-Perot modulator .....	62
Gain/bandwidth tradeoff .....	63
Broad-bandwidth Resonant (BBR) Modulator .....	68
Theoretical analysis of BBR .....	69
BBR - all fiber breadboard.....	72
BBR hybrid –glass $\mu$ -ring and LiNbO <sub>3</sub> phase modulator .....	75
BBR in LiNbO <sub>3</sub> .....	85
BBR – integrated hybrid .....	90
BBR modulation linearity .....	100
3.4    Conclusions .....	105
Appendix A - Published papers/Conference presentations.....	107
Appendix B - List of Symbols, Abbreviations, and Acronyms .....	109
Appendix C - References .....	110

## List of Figures

Figure 1. Concept diagram of the cascade laser wherein individual lasers are connected electrically in series and their optical outputs are coupled in parallel onto a photodetector. ....	2
Figure 2. Main approaches to obtain cascaded semiconductor diode lasers.....	4
Figure 3. Directly-modulated semiconductor laser slope efficiency versus bandwidth (research devices – not fiber coupled). ....	5
Figure 4. Estimated slope efficiency and bandwidth for various types of cascade lasers. The bipolar cascade was investigated under RFLICs. ....	6
Figure 5. Composition and doping used for the first bipolar cascade laser which operated CW at room temperature under the quick start RFLICs program.....	7
Figure 6. Modeled vs measured tunneling current.....	8
Figure 7. Effect of indium mole fraction on tunneling current.....	9
Figure 8. MIT experimental setup for testing resonant enhancement to increase diode laser modulation bandwidth. ....	10
Figure 9. Experimental bandwidth of slave laser without (unlocked) and with (locked) master laser injection. ....	11
Figure 10. Measured injection locking range for the DBR laser. ....	12
Figure 11. Adiabatic chirp of the master-slave DBR laser (with left plot) and without (right plot) optimally detuned loading.....	13
Figure 12. Types of semiconductor cascade lasers.....	14
Figure 13. Signal-to-Noise Ratio (SNR): simulation results. ....	15
Figure 14. Energy band diagram of semiconductor quantum well laser showing the various processes contributing to the current noise. The carrier recombination and leakage in the SCH regions also contribute to the current and photon noise. ....	16
Figure 15. Spectral density (in dB) of photon noise (normalized to shot noise) of a 1.55 $\mu\text{m}$ laser. The inclusion of current partition noise increases the noise level by several dB above that predicted by the model presented in references 2 and 3. Boxes are the experimentally measured results in reference . ....	17
Figure 16. The high frequency noise on the current through the semiconductor laser is measured with an RF spectrum analyzer attached to the RF port of the bias-tee. The current noise is amplified with an LNA before entering the spectrum analyzer.....	17
Figure 17. Spectra (in dB) of current noise measured at different bias currents for a 1.55 $\mu\text{m}$ semiconductor laser. The spectra are normalized to the spectrum a little below threshold (measurement bandwidth 100MHz – 2GHz).....	18
Figure 18. InGaAsP/InP single junction laser fabricated at MIT. This laser was used to test the hypothesis that the optical noise is being coupled back into the current noise. Epitaxial material obtained from EPI. ....	19
Figure 19. Far-field radiation patterns. ....	20
Figure 20. Guiding and anti-guiding waveguides.....	20
Figure 21. Near- and far-field patterns for bipolar ARROW cascade lasers, for three different active region and waveguide spacings.....	22

Figure 22. Threshold gain (left graph) and threshold current density (right graph) versus width of active region core in a bipolar ARROW cascade laser.....	23
Figure 23. Proposed MIT design for the first, long-wavelength bipolar cascade laser. ....	24
Figure 24. Near-field pattern of cascade laser chip H1 (100 $\mu\text{m}$ stripe, 1 mm cavity length), pulsed with 1.6 A. Transverse pattern, showing two spatial lobes, is at right, and lateral scans of the two lobes are shown at left.....	28
Figure 25. Lateral and transverse scans of the far-field pattern of cascade laser chip H1.....	28
Figure 26. Lateral and transverse scans of the far-field pattern of cascade laser chip I6. ....	29
Figure 27. Measured P-I characteristic of cascade laser chip A10 (100 $\mu\text{m}$ stripe, 1 mm cavity length, p-side down), biased with 200 ns pulses at 25 kHz repetition frequency.....	30
Figure 28. Measured I-V characteristic of cascade laser chip I6 (same wafer as A10, CW operation). ....	30
Figure 29. Plot of measured P vs. I curve with substrate temperature as the parameter for a fundamental mode device. ....	34
Figure 30. Plot of threshold current density vs. temperature for the Sarnoff cascade lasers.....	35
Figure 31. Power and voltage versus current.....	36
Figure 32. Spectra below threshold (point A in Figure 31). ....	36
Figure 33. Spectra in high slope region (point B in Figure 31). ....	37
Figure 34. Spectra above high slope region (point C in Figure 31).....	37
Figure 35. Close-up of spectra below threshold (point A in Figure 31). ....	38
Figure 36. Close-up of spectra in high slope region (point B in Figure 31). ....	38
Figure 37. Close-up of spectra above high slope region (point C in Figure 31).....	39
Figure 38. Voltage and Power versus current. This laser showed more than one mode in the vertical direction. Into multi-mode fiber coupling efficiency was about 52%. ....	40
Figure 39. RF frequency output of same laser of Figure 38 at 200 mA. ....	40
Figure 40. RF frequency output of same laser of Figure 38 at 201 mA. ....	41
Figure 41. Expanded view of RF frequency output of same laser of Figure 38 at 201 mA. ....	41
Figure 42. Power and voltage versus current.....	42
Figure 43. Spectral and far field measurements for a current below threshold (150 mA). ....	43
Figure 44. Spectral and far field measurements for a current above threshold (203 mA).....	43
Figure 45. Spectral and far field measurements for a current above threshold (209 mA).....	44
Figure 46. P-I and V-I curves of a ridge waveguide laser in anti-symmetric mode. ....	45
Figure 47. Mode intensity distribution in a cascade laser structure. The Internal P-cladding (IPC) is marked by arrow.....	46
Figure 48. DQE and electrical properties of 50 $\mu\text{m}$ stripe broad area lasers.....	48
Figure 49. Ridge waveguide lasers with 2 active regions. These devices are uncoated with cavity length of 0.5 mm. ....	49
Figure 50. Ridge waveguide lasers with 2 active regions. These devices are uncoated with a cavity length of 0.5 mm. This laser has a high dqe of 76%. ....	50
Figure 51. The P-I and I-V characteristics were measured over a range of temperatures from 0 to 50 $^{\circ}\text{C}$ of a 3 $\mu\text{m}$ ridge waveguide laser with HR 97%/AR 3% coatings. ....	51
Figure 52. Frequency response of two active region cascade laser. ....	53
Figure 53. Laser in lab configuration package.....	54
Figure 54. Frequency response of laser package. ....	54

Figure 55. Frequency response of two active region cascade laser without the package response. ....	55
Figure 56. Waveguides formed on a surface by wet etching. The waveguide structure is shown at right, and a photograph of a top-view AFM image of the structure is shown at left. ....	59
Figure 57. Grating electrodes on LiNbO <sub>3</sub> for the fabrication process test. In photograph at left, a titanium in-diffused waveguide is aligned in a gap (horizontal region) between electrodes (lighter comb-shaped lighter regions). The schematic diagram shows how this four-step electrode alignment procedure was successfully used in the past to fabricate a chirped grating structure in LiNbO <sub>3</sub> . ....	60
Figure 58. Comparison of the thinnest conventional lithium niobate and the new thin lithium niobate developed by Columbia. ....	61
Figure 59. Cross section sketch of the vertical Fabry-Perot modulator. ....	63
Figure 60. Representation of a Fabry-Perot Cavity of length $L$ with reflectivities $R1$ and $R2$ ..	67
Figure 61. Representation of a ring resonator of circumference $C$ and reflectivities $k1$ and $k2$ ..	67
Figure 62. Novel modulator that combines a non-resonant phase modulator with a resonant loop. ....	68
Figure 63. Transfer functions of a Mach-Zehnder and broad bandwidth resonant modulators. .	69
Figure 64. Transfer function of BBR as a function of optical frequency. ....	70
Figure 65. Slope of transfer function of BBR as a function of optical frequency. ....	70
Figure 66. Results of MATLAB time-domain analysis of Gain for two links with different resonant modulator types having the same resonator roundtrip time $\tau = 100$ psec. Left axis: link Gain for Fabry-Perot modulator with mirror reflectivity $R=0.9$ (magenta curve); Right axis: link gain for novel ring resonator-based modulator with $k=0.5$ . ....	71
Figure 67. Results of MATLAB analysis of the resonant modulator-based link with $k = 0.4$ , $L \sim 2.5$ mm, $\theta = 1.9723 \pi$ , and $\alpha = 0.95$ biased at $\phi = 20.3^\circ$ . The link gain is flat at $\sim 1$ dB (corresponding to $V_{\pi,eq} \sim 0.3$ V) over a bandwidth of approximately 1–54 GHz. ....	72
Figure 68. All fiber BBR breadboard. ....	73
Figure 69. Modeled and measured gain of the all fiber BBR breadboard. ....	73
Figure 70. Experimental set up of broadband resonant (BBR) modulator. Disconnecting the fibers at the location marked “x” arranges the set up into a Mach-Zehnder configuration. ....	74
Figure 71. The experimental performance comparison of a phase modulator in the BBR vs. a MZ configuration. ....	74
Figure 72. Diagram of the hybrid $\mu$ -ring/LiNbO <sub>3</sub> phase modulator BBR with optional erbium doped waveguide amplifier (EDWA). ....	75
Figure 73. Experimental setup of the first hybrid BBR. ....	76
Figure 74. Measured and modeled gain of the first hybrid BBR without an EDWA. ....	76
Figure 75. Set up of second hybrid BBR. ....	77
Figure 76. Link data with/without amplifier. ....	78
Figure 77. Transfer function of BBR for (a) higher insertion loss of phase modulator arm (b) zero insertion loss of phase modulator arm. ....	79
Figure 78. RF link gain of BBR for (a) higher insertion loss of phase modulator arm (b) zero insertion loss of phase modulator arm. ....	79
Figure 79. Measured transfer function of BBR hybrid with EDWA. ....	80
Figure 80. Lasing of the EDWA in the BBR configuration with no optical input to the BBR. .	81



Figure 81. Detail of BBR identifying lengths, time delays and noise sources. ....	81
Figure 82. Noise power for two different linewidths and different unbalanced MZ lengths. ....	83
Figure 83. BBR modulator design. ....	84
Figure 84. Available gain enhancement over regular MZI vs. $\alpha$ and $t_2$ . Assumes current LO ring design, $k_z=45\text{deg}$ . ....	84
Figure 85. $V\pi$ reduction factor with BBR vs. optical power losses. ....	85
Figure 86. BBR in $\text{LiNbO}_3$ . ....	86
Figure 87. Mask layout of preliminary BBR. ....	87
Figure 88. Mask layout of preliminary MZ with electrode length the same as the BBR. ....	88
Figure 89. BBR frequency dependence (does not include effect of resonance) with $V\pi L=12$ Vcm, $L=11$ cm, $a_1=0.0015(\text{GHz}\cdot\text{cm})^{-1}$ , $R=35$ Ohms. ....	89
Figure 90. $V\pi$ vs. frequency (does not include effect of resonance $\sim 0.6$ GHz). ....	89
Figure 91. Integrated hybrid BBR. ....	90
Figure 92. Loss budget- standard transformer, $w_x=w_y=4.9\mu\text{m}$ . ....	91
Figure 93. TM performance with new mode transformer to eliminate rotators, redesign mode transformers to reduce hydex/LN mode mismatch loss, TM operation only. ....	93
Figure 94. Schematic of a $\text{LiNbO}_3$ chip co-packaged with a microring resonator chip. ....	94
Figure 95. Schematic of a ring resonator chip having a single ring and dual sided input/output ports. ....	95
Figure 96. Broad bandwidth resonant modulator in an integrated package. ....	96
Figure 97. Modeled transfer functions MZ, 1st & 2nd BBR assuming the same phase modulator $V\pi$ . ....	98
Figure 98. Modeled slope (left) and link gain (right) at 1.7GHz assuming $P=11.5\text{mW}$ , $\text{RPD}=0.68\text{A/W}$ , and $V\pi$ (large signal) = 3.1V. ....	98
Figure 99. Small signal modulation link gain of 1st and 2 <sup>nd</sup> BBR. ....	99
Figure 100. Relative measurement of link loss. ....	99
Figure 101. Broad bandwidth resonant modulator (BBR). ....	101
Figure 102. The transfer functions of the Mach-Zehnder modulator (MZ) and the Broad Bandwidth Resonant Modulator (BBR). ....	102
Figure 103. Equivalent $V\pi$ of the BBR, normalized to that of an MZ modulator. ....	103
Figure 104. Third order intercept point (IP3) of the MZ as a function of radians or applied voltage, and of an MZ having the same $V\pi_{\text{equivalent}}$ . ....	104
Figure 105. Third order intercept point (IP3) of the MZ as a function of radians or applied voltage over a smaller range than Figure 106, and of an MZ having the same $V\pi_{\text{equivalent}}$ . ....	104
Figure 106. Model for $V_{\pi, \text{eff}}$ vs. $t_1$ (phase modulator arm loss) at 2 GHz. ....	106

## List of Tables

Table 1. The progress in optical RF link performance that occurred during RFLICs .....	1
Table 2. MIT growth layers for the laser structure shown in Figure 23. ....	25
Table 3: Comparison of modulator materials. ....	62
Table 4. Loss budget for entire modulator- standard transformer, $w_x=w_y=4.9\mu\text{m}$ .....	92
Table 5. Loss budget for entire modulator- new transformer , $w_x=4.9\mu\text{m}$ , $w_y=3\mu\text{m}$ . ....	92
Table 6. Optical insertion loss tabulation in phase modulator only.....	97
Table 7. Optical insertion of phase modulator arm of BBR including coupling to ring.....	97
Table 8. Link gain and $V\pi$ of BBR and MZI type devices.....	100

# 1 Summary

The realization of true lossless, high bandwidth and high dynamic range optical RF links has been hindered by the low performance and high cost of its constituent optical components. In particular, the inefficiency of RF modulation in both directly and externally modulated laser sources is recognized as a root cause of high link loss and noise figure. In our program, we pursued both direct and external modulation links. Table 1 shows the progress in link performance that occurred during RFLICs from 2000 - 2006. Note that there has been no COTS direct modulation improvement. External modulation links continue to provide the highest gain. Our approach to obtain the results in Table 1 included:

- Development of directly modulated bipolar cascade and resonantly-enhanced lasers
- Investigation of external modulation techniques
- Exploration of electro-optic materials for external modulators

**Table 1.** The progress in optical RF link performance that occurred during RFLICs

	3-dB Bandwidth (GHz)	Link Gain (dB)
Directly modulated laser (COTS 1999)	3 20	-20 to -25 -25 to 30
Directly modulated laser (COTS 2006)	3 20	-20 to -25 -25 to 30
Directly modulated bipolar cascade - RFLICs	4	-13 (if properly fiber coupled)
Resonantly-enhanced (in-plane) - RFLICs	21	-40
Mach-Zehnder external modulator (COTS 1999)		
Lumped-element electrode	3	-5
Traveling-wave electrode	20	-15
Mach-Zehnder external modulator (COTS 2006)		
Lumped-element electrode	3	-5
Traveling-wave electrode	20	-11
Broad bandwidth resonance modulator – RFLICs with internal EDWA	15	-23

This work was divided into a direct modulation and an external modulation effort. Therefore, this report will be divided into two sections, one representing each modulation effort. Each section will have an introduction to the key issues for that particular modulation technique, followed by a detailed review of our methodologies and results. Each section will end with conclusions about our results.

## 2 Direct Modulation

### 2.1 Introduction

To date, applications of direct modulation analog photonics technology have been limited by the fact that high-performance fiber-optic links are limited by the quantum limit for the slope efficiency of one laser. One aim of this program was to address the need for high-performance RF photonic links by developing an innovative device approach called the *cascade laser*. The slope efficiencies achievable from cascade lasers should permit direct modulation links to enter the realm of performance that had heretofore been unattainable even using the more costly external modulation link approach.

Semiconductor cascade lasers are capable of producing multiple photons for each injected electron. The slope efficiency of cascade laser devices can therefore be made in excess of the fundamental limit  $\hbar\omega/e$ . These laser devices may play a very important role in RF photonic links since link gain increases as the square of the laser slope efficiency. In addition, cascade lasers have higher series resistances and can be better impedance matched to the driving electronic circuit. There have been several recent demonstrations of cascade lasers and the various implementation schemes reported in edge emitting and vertical cavity surface emitting configurations.

Cox et al.<sup>1</sup> were the first to apply the cascade laser – which is shown in concept form in Figure 1 – to improve the performance of analog optical links. They derived the fact that the slope efficiency of the cascade is simply the sum of the slope efficiencies of the individual lasers in the cascade. This fact permits the cascade laser to attain slope efficiencies above the quantum limit for the slope efficiency of an individual laser.

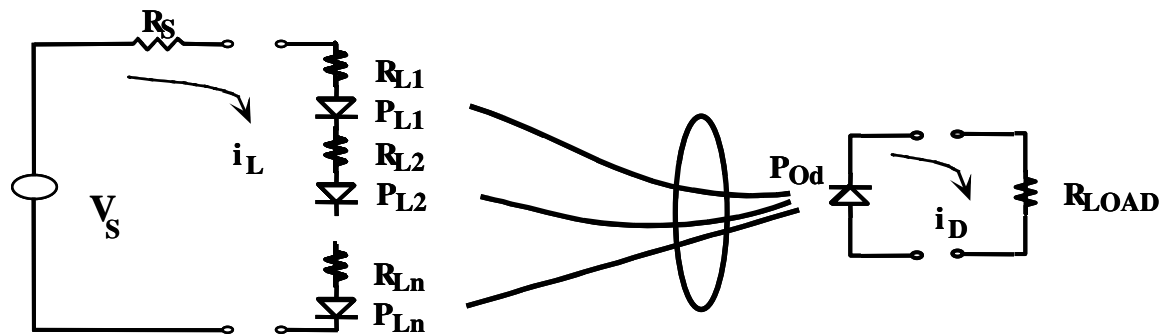


**Figure 1.** Concept diagram of the cascade laser wherein individual lasers are connected electrically in series and their optical outputs are coupled in parallel onto a photodetector.

During the quick start RFLICs program, MIT fabricated the first CW, room temperature, monolithically integrated cascade laser that consisted of two lasers for a total length of 450  $\mu\text{m}$

long and 5  $\mu\text{m}$  wide. With this cascade system, there were two distinct thresholds. When the second laser junction reached threshold, the slope efficiency abruptly switched from 0.313 W/A to 0.622 W/A per facet. This slope efficiency corresponds to a differential quantum efficiency of 99.3% at an average wavelength of 992 nm. For comparison a state-of-the-art single laser would have a quantum efficiency of less than 50%. The I-V characteristics of this structure indicate a threshold voltage of 3.2 V and differential resistance of 8 ohms.

To summarize what has been previously verified by PSI and others, Figure 2 shows demonstrated cascade lasers. In these lasers, photons are emitted by an interband transition from conduction to valence bands. The cascade process requires the recently arrived valence electrons to be somehow converted into conduction electrons. These lasers were designed by connecting multiple lasers in series electrically. The number of lasers in the cascade can be increased until the total impedance is  $50\Omega$ . The effectiveness of the cascade is diminished if the total impedance of the cascade is not  $50\Omega$ . Another design consideration is the laser topography design which maximizes the collection of light from multiple lasers onto a single fiber coupled photodetector without the use of a conventional combiner whose optical loss would cancel the slope efficiency improvements of the cascade.

One possible cascade configuration is an edge-emitting lasers configuration with the in-plane laser connected in series both optically and electrically as in Figure 2b. The cascade process of re-excitation is achieved with the reinjection of an electron from an ohmic contact. This has been demonstrated by PSI/University of Illinois at Urbana-Champaign (UIUC) under an SBIR and University of California at Santa Barbara (UCSB) under another program. Individual lasers of the cascade are short and have high series resistance; connecting these electrically in series results in still higher overall device series resistance. Keeping overall device resistance acceptable for modulation limits the total number of devices that can be cascaded. These lasers also have performance degradation due to carrier leakage over the heterobarrier.

The second type of laser was pursued at the University of Ulm in Germany, and is shown in Figure 2c. It is a stacked vertical cavity surface-emitting laser (VCSEL) cascade in which individual laser layers are connected electrically in series by tunnel junctions and situated optically in series within a single optical mode. Since they have a small single transverse mode, these lasers have high series resistance and limited output power.

The third type of cascade laser shown in Figure 2d and supported by an SBIR awarded to PSI consists of individual surface-emitting lasers connected electrically in series with the individual optical outputs collected into one fiber. The pitch of the lasers for efficient fiber coupling is difficult to achieve. Also, just as in the other VCSEL case, the series resistance is high due to the small devices.

The first step in determining a better cascade laser was to review and understand cascade laser technology to date. Some of the limitations to obtaining high slope efficiency are listed below:

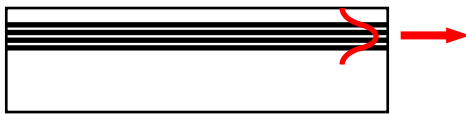
- Intracavity optical loss
- Fiber coupling efficiency

- Carrier leakage over heterobarrier
- Non-radiative recombination
- Temperature dependence of carrier confinement
- Materials issues

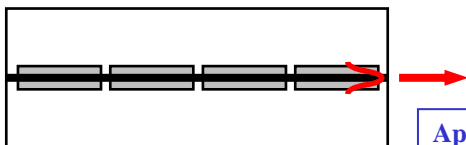
Under this DARPA RFLICs program, PSI/Sarnoff tried to overcome the above limitations by developing the edge-emitting bipolar cascade lasers as shown in Figure 2a. For this type of laser, the cascade process of re-excitation is achieved by the electron tunneling from the valence to conduction band. This laser utilizes vertically stacked active regions separated by tunnel junctions in a single optical cavity. The tunnel junctions eliminate the parasitics associated with interconnect coupling and permit high speed transport of electrons from one active region to the next. Since vertical stacking does not allow for the heatsink to scale as the number of cascade sections, the maximum number of cascade sections is limited to between three and four. These lasers had limited slope efficiency due to the excess optical loss in the tunnel junction. Also, it was difficult to fit many laser layers within a thin single transverse mode waveguide. The maximum number of lasers in the cascade achieved during this program was three.

### Edge-Emitting Lasers

(A) Bipolar Cascade: Individual laser layers connected electrically in series by tunnel junctions and situated optically in parallel within a single waveguide (PSI/Sarnoff)



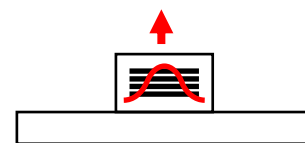
(B) In-plane individual lasers connected electrically in series and situated optically in series within a single waveguide (UCSB, PSI/UIUC)



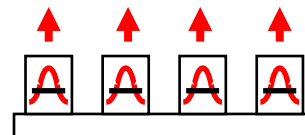
Approach (A) was pursued in this program

### Vertical Cavity Surface-Emitting Lasers (VCSEL)

(C) Individual laser layers connected electrically in series by tunnel junctions and situated optically in series within a single optical mode (Ulm)



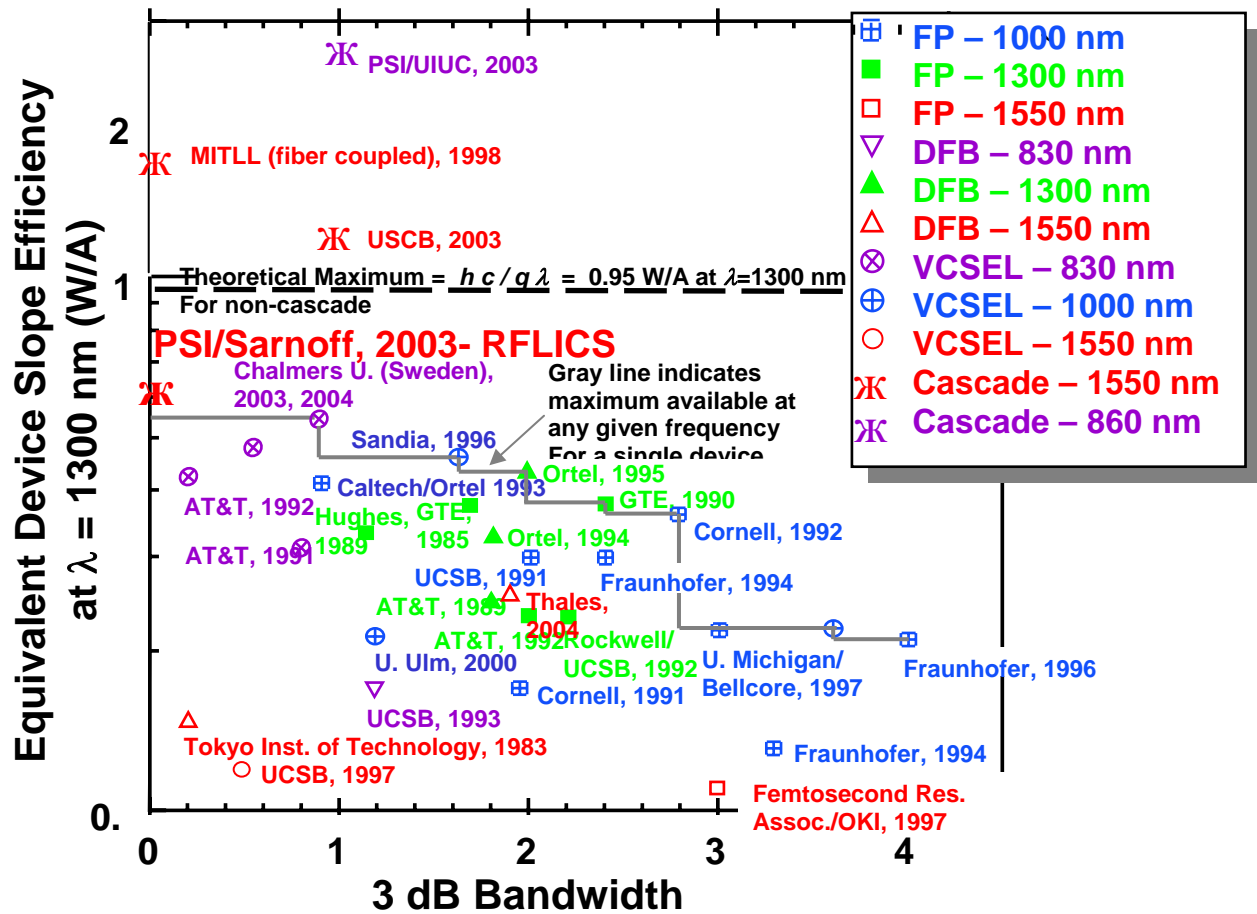
(D) Individual lasers connected electrically in series with the individual optical outputs collected into one fiber (PSI/UIUC)



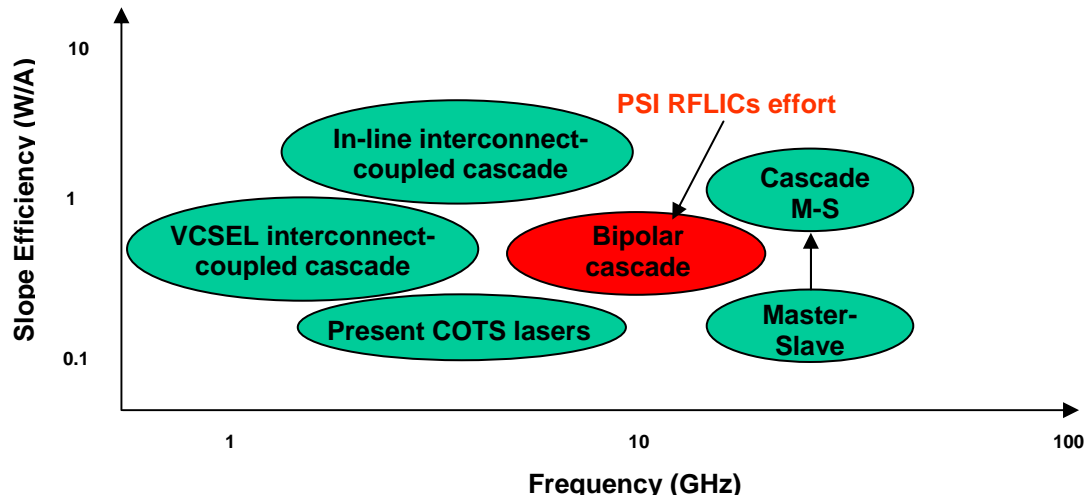
**Figure 2.** Main approaches to obtain cascaded semiconductor diode lasers.

Figure 3 summarizes the progress in improving slope efficiencies by various researchers for single and cascade lasers. Figure 4 is a variation of Figure 3 and includes the lasers grouped by type that are likely to yield better slope efficiency and/or bandwidth than present COTS devices (which are single-laser devices) as a function of frequency. Due to the higher frequency requirements of RFLICs, we planned to investigate the bipolar cascade with Dr. Ram at the

Massachusetts Institute of Technology and complete a technology transfer for production to Sarnoff Corporation. As the RFLICs contract progressed, the priorities in Dr. Ram's laboratory changed in early 2002 and he chose to withdraw from the program. Dr. Ram no longer desired to investigate the cascade laser under RFLICs due to MIT's inability to meet the RFLICs schedule with respect to wafer growth and device processing. To continue the work on the bipolar cascade laser, PSI then revised the program plan to include the development of laser design, materials growth, laser processing, and preliminary testing with Sarnoff Corporation.



**Figure 3.** Directly-modulated semiconductor laser slope efficiency versus bandwidth (research devices – not fiber coupled).



**Figure 4.** Estimated slope efficiency and bandwidth for various types of cascade lasers. The bipolar cascade was investigated under RFLICs.

## 2.2 Methodology and Results: Team I - PSI, MIT and Sarnoff

### Tunnel junction design – IV model

The bipolar cascade laser consists of active lasing regions that are connected by tunnel junctions, which permit the forward conduction of current when they are reverse biased. Hence a key step in the development of the bipolar cascade laser was the tunnel junction. The development of InP based bipolar cascade lasers to achieve at laser at 1550 nm proceeded with the design and testing of InGaAs and InGaAsP tunnel junctions. The first generation bipolar cascade—fabricated in GaAs—incorporated one tunnel junction between the two cascaded lasing junctions. The fabrication of the bipolar cascade laser required that a number of layers of different composition and doping be grown on a wafer. An example of the layers MIT used to make the first bipolar cascade laser to operate CW at room temperature for the quick start up is shown in Figure 5.



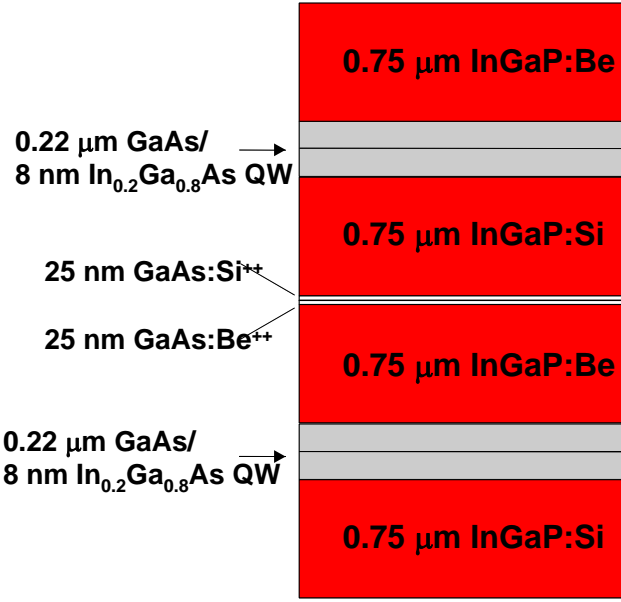


**Figure 5.** Composition and doping used for the first bipolar cascade laser which operated CW at room temperature under the quick start RFLICs program.

In turn, one of the keys to the design of a successful tunnel junction was an accurate IV model. Figure 6 is a plot of tunneling current vs. bias voltage, where the measured IV is shown by the dotted curve. The common tunnel junction IV model assumed a triangular-shaped band structure. A more rigorous IV model assumed a parabolic band shape. The calculated IV based on this assumption is plotted as the solid line in Figure 6. These calculated IVs matched up well with the measured IV. Consequently we had a tunnel junction IV model that was sufficiently accurate that we could base design decisions on it.

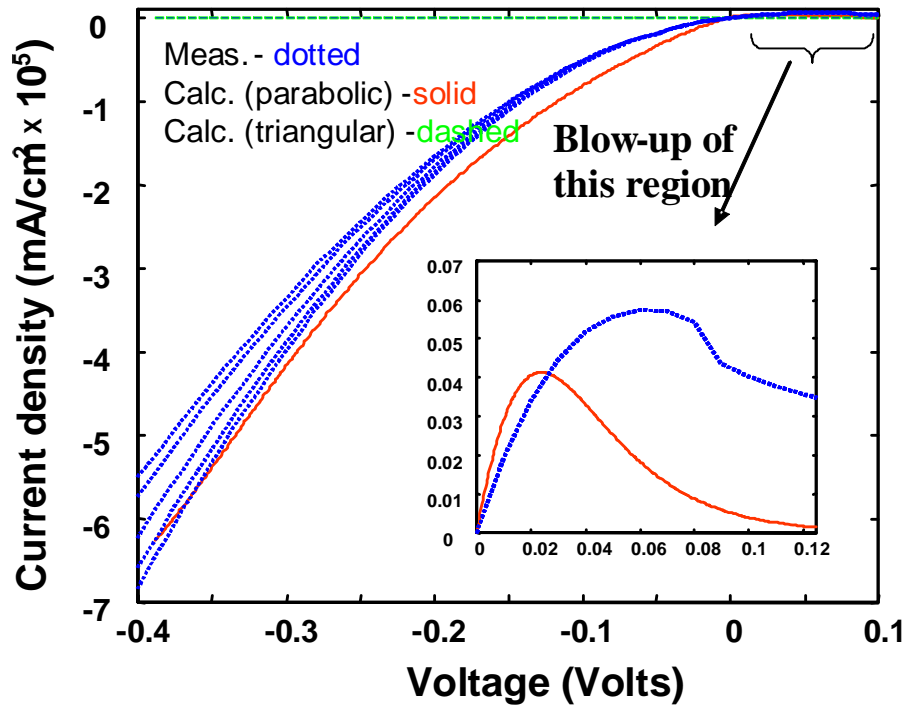


**Figure 6.** Modeled vs measured tunneling current.

One of the key differences in moving from GaAs to InP, as far as the tunnel junction goes, was that it was more difficult to achieve the high doping density required for tunnel junctions in InP than it was in GaAs. We attacked this problem from two fronts: developed growth techniques to achieve as high a doping density as possible and investigated tunnel diode band designs to reduce the doping density required.

An example of the latter approach is shown in Figure 7. In the work summarized here, we investigate the effect on the IV of moving from a pure GaAs tunnel junction to a junction in which up to 15% of the Ga has been replaced with In. The left hand graph shows the impact of this change on the IV; the higher the In concentration, the lower the potential barrier and hence the higher the current at a given voltage.

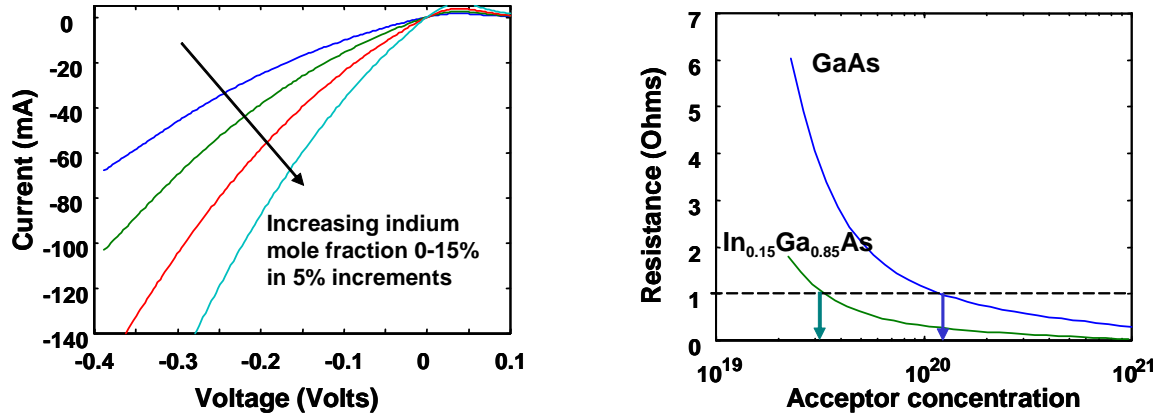


**Figure 7.** Effect of indium mole fraction on tunneling current

The right hand graph plots the resistance vs. the doping concentration for the two extremes investigated: pure GaAs and 15% InGaAs. In the tunnel junction design, we are typically trying to achieve a given resistance. For the example shown here we have assumed 1 ohm, which is represented by the horizontal dashed line. By comparing the intersection of this line with the curves for pure GaAs and 15% InGaAs, we see that the doping concentration can be reduced by a factor of more than 3 by adding just 15% In. Consequently these analyses showed that band modification can be an effective tool in our arsenal for achieving the required tunnel junction performance.

## Laser design and characterization

### *Resonant enhanced laser for greater modulation bandwidth*

The Cox<sup>1</sup> demonstration previously discussed was a low frequency solution for high slope efficiency. RFLICs required modulation devices to have a greater than 20 GHz bandwidth. The direct modulation bandwidth of a semiconductor laser is determined by how strongly the carrier and photon reservoirs are coupled to each other. We investigated resonant enhancement as a technique for increasing the modulation bandwidth of diode lasers. This involves optical resonant excitation of a semiconductor laser for the purpose of enhancing the RF modulation bandwidth.

We began the investigation by measuring experimentally the injection locking range as a function of the detuning and the injection ratio. The stronger the coupling, the faster changes in the carrier density affect the photon density and vice versa. Modulation bandwidth enhancement occurs because the coupling between the carriers and photons is enhanced, which in turn occurs because the injection locking introduces a coupling between the carrier density and phase offset of the injection and the cavity resonance. This phase offset is in turn coupled very strongly to the photon density. The bandwidth of a laser depends on the strength of the coupling between

the inverted carrier population,  $N$ , and the photon population,  $S$ . This coupling is represented by the off diagonal terms in the small signal rate equations, viz:

$$\frac{d}{dt} \begin{bmatrix} \Delta S \\ \Delta N \end{bmatrix} = \begin{bmatrix} 0 & \Gamma v_g a_N S \\ -\frac{1}{\Gamma \tau_p} & -v_g a_N S \end{bmatrix} \begin{bmatrix} \Delta S \\ \Delta N \end{bmatrix}$$

Thus to increase the bandwidth, one wants to increase the coupling. One way that was proposed to do this was to inject photons from one laser (the master) directly into the cavity of another laser (the slave). There are a range of effects one can obtain from such injection; for example if it is strong enough, one gets mode locking.

The injection ratio is defined as the ratio of the injected master power to the slave power. An experimental setup at MIT to test this approach is shown in Figure 8. Since the relative wavelength of the two lasers is also a critical experimental parameter, both the master and slave lasers were made tunable.

Frequency response data using this setup are shown in Figure 9. With no injection (unlocked) into the slave laser, the 3 dB bandwidth was 4.25 GHz. With the master laser power 1.9 dB below the slave laser power, the bandwidth of the slave laser (locked) increased to 21 GHz – almost a factor of 5x the unlocked bandwidth.

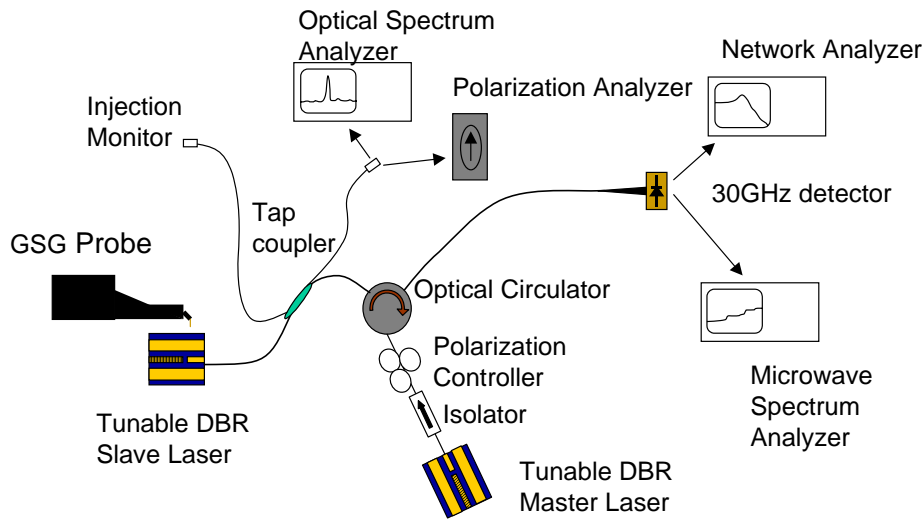


**Figure 8.** MIT experimental setup for testing resonant enhancement to increase diode laser modulation bandwidth.

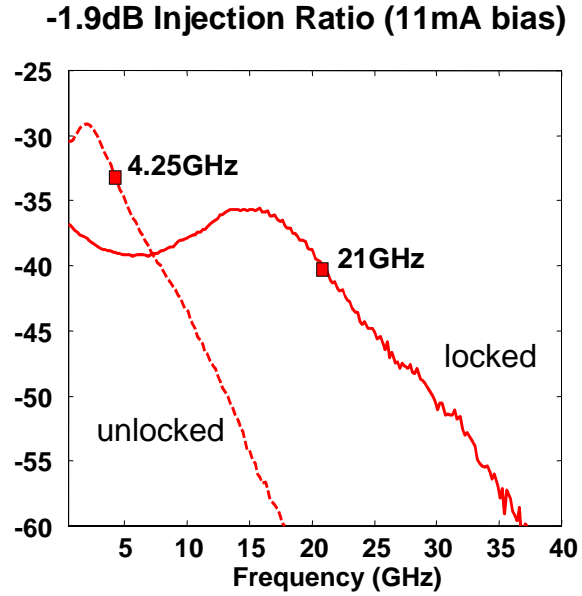


**Figure 9.** Experimental bandwidth of slave laser without (unlocked) and with (locked) master laser injection.

One important piece of information in understanding the operation of the master-slave configuration is the locking range. The top half of Figure 10 shows the measured locking range as a function of master/slave detuning and injection ratio for two cases: when the injected light from the master laser is on the short or long wavelength side of the slave laser. The first fact to notice is that the wider locking range at high injection ratios on the long wavelength side vs. the short wavelength side. This can be readily seen by comparing the length of the arrows marked “A” and “B” in the figure.

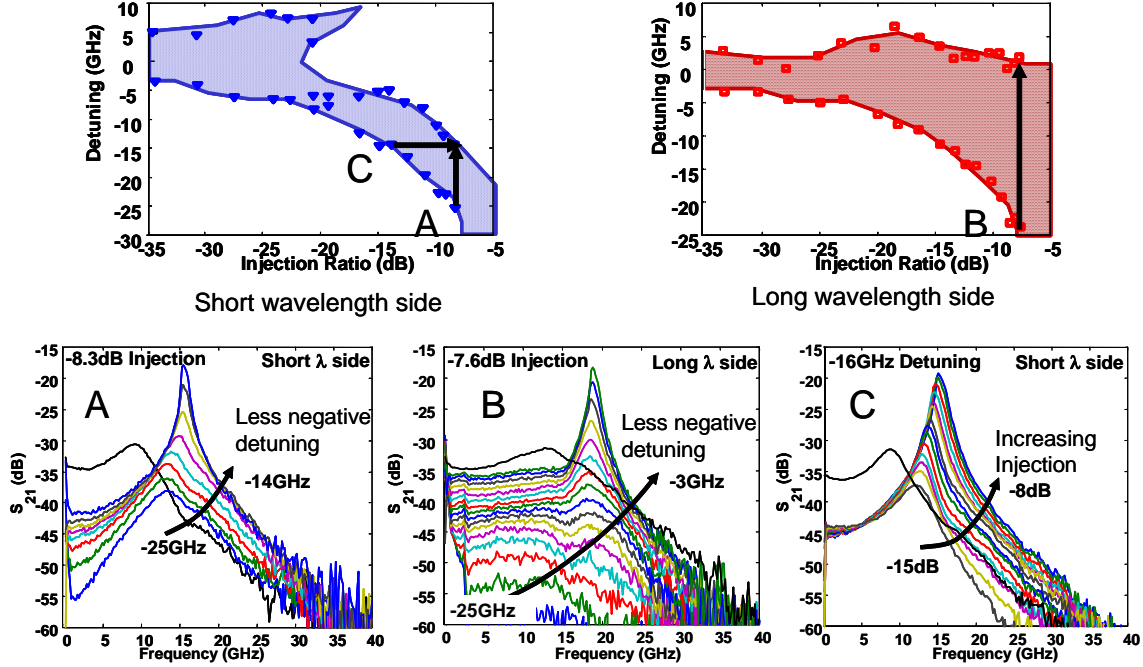


**Figure 10.** Measured injection locking range for the DBR laser.

Detailed snap shots of the locking performance are shown in the three plots across the bottom of Figure 10. The letters in the upper left corner of each of these plots corresponds to the lettered arrows in the top half plots. For example compare cases “A” and “B” where the injected optical power is constant and the detuning is changed. Under these conditions we see that the “A” case suffers  $\sim 5$  dB lower modulation efficiency—as measured by  $S_{21}$ —below the relaxation peak, whereas case “B” does not. Further note that the efficiency decreases as the detuning increases. Note that the injection optical power is about the same in both cases.

Case “C” investigates in detail the performance when the detuning is held constant and the injection power is changed. Similar to case “A”, the “C” case modulation efficiency is  $\sim 5$  dB below the low frequency response. But unlike the “A” case, the “C” case modulation efficiency remains constant as the injection power changes.

We also investigated a side benefit of resonant modulation: the elimination of laser chirp. Normally intensity modulation of a diode laser introduces a change in the wavelength of the laser as well; this is the so called laser chirp. Variations in the carrier density lead to variations in the cavity resonance and hence in the lasing frequency. However, consider the case of the resonant modulation we are investigating here. In this case the master laser determines the wavelength of the slave laser because the oscillation frequency is locked to the master frequency independent of the cavity resonance. Hence intensity modulation of the slave laser cannot introduce chirp, at least as long as the slave laser remains locked to the master.

To test this hypothesis we measured the wavelength of the slave laser as a function of bias with and without injection from the master. The data from a representative experimental run are shown in Figure 11. When the slave was free-running, i.e. when there was no power injected from the master, we saw a change in the wavelength as a function of bias, as expected; these data are plotted as the “free-running” points in the graphs.

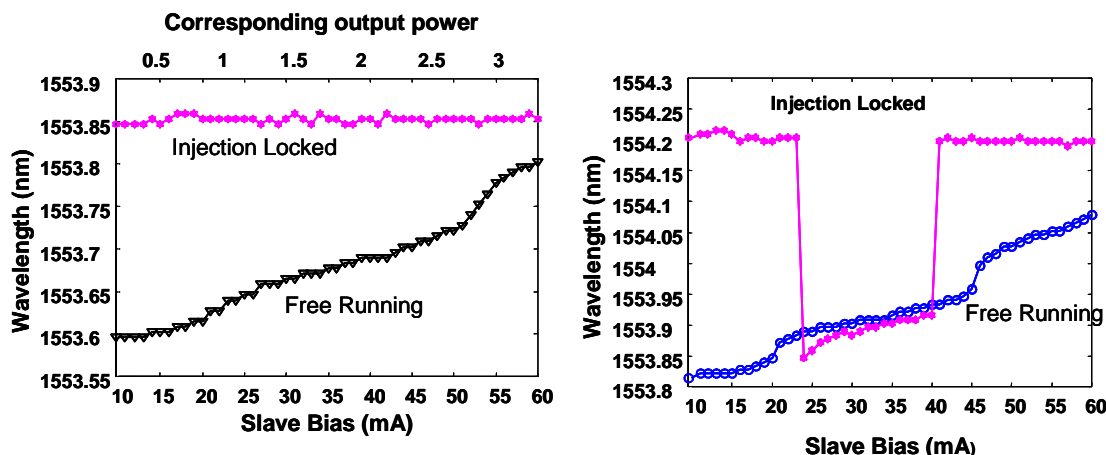


**Figure 11.** Adiabatic chirp of the master-slave DBR laser (with left plot) and without (right plot) optimally detuned loading.

When the slave was locked to the master, the wavelength of the slave was constant as the slave bias was changed. These data are plotted as the “injection locked” points in the graphs of Figure 11. However we again found that the injection locking range was a function of the locking wavelength relative to the spectrum of the slave laser DBR (distributed Bragg reflector). On one side of the DBR the locking range was continuous over more than a 6:1 range of slave laser optical power. However, locking the slave on the other side of the DBR spectrum resulted in a large range of laser bias where the slave laser dropped out of lock. This is another manifestation of the asymmetry in locking performance we have seen before; see for example the different injection locking maps shown in Figure 10.

Progress was made on the resonant enhanced laser. MIT was able to demonstrate a couple of interesting aspects of this technique: a 5x bandwidth enhancement (over the relaxation resonance of a single laser) and zero chirp modulation under certain conditions. However the budget pressure that was put on our effort due to MIT’s lack of performance on the cascade laser meant that something had to be trimmed. Therefore, it was decided to suspend this work.

### *Noise*

Besides focusing on achieving high frequency performance, there are other design issues as well, such as noise and fiber coupling efficiency. For the laser noise, MIT has modeled four laser configurations, as shown in Figure 12. A first principles theory regarding the degree of correlation among the noise sources in each of the various laser sections was developed and

coded as a computer program. Multiple simulations were run using this model; a sample of the output is shown in Figure 13. The left hand plot in this figure shows the SNR as a function of bias above threshold for a fixed number of stages in the cascade, in this case 4. The simulation results show that the bipolar cascade—the configuration chosen for investigation under RFLICs—has 5 dB higher SNR than any other configuration. Further the right hand plot in this figure, which plots the SNR vs. the number of sections in the cascade for a fixed bias above threshold, shows that the SNR advantage of the bipolar cascade increases with the number of sections. However present fabrication limitations preclude us from reaching the higher number of stages in the bipolar cascade.

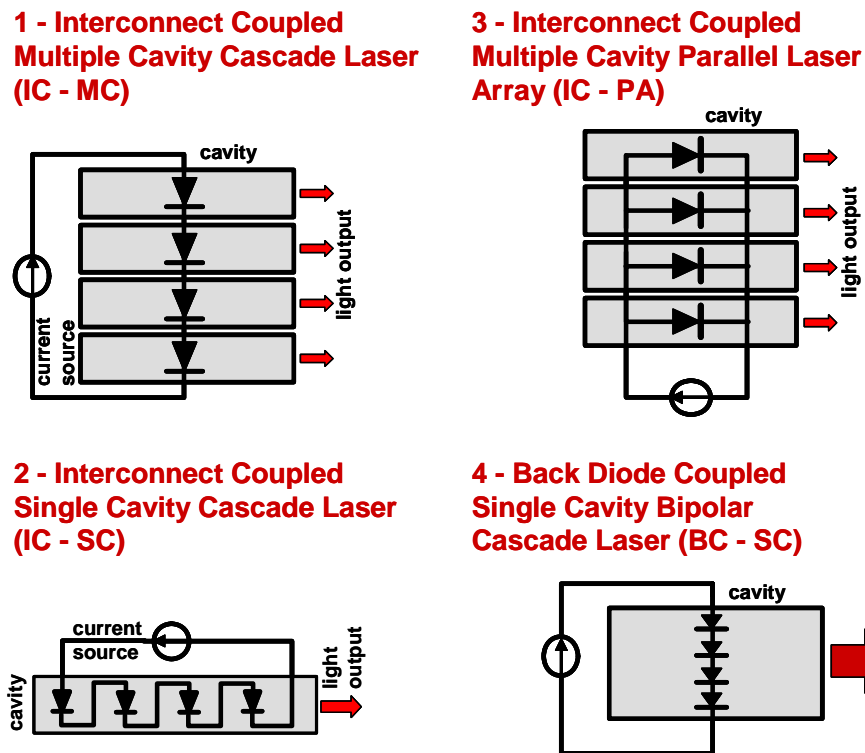


**Figure 12.** Types of semiconductor cascade lasers



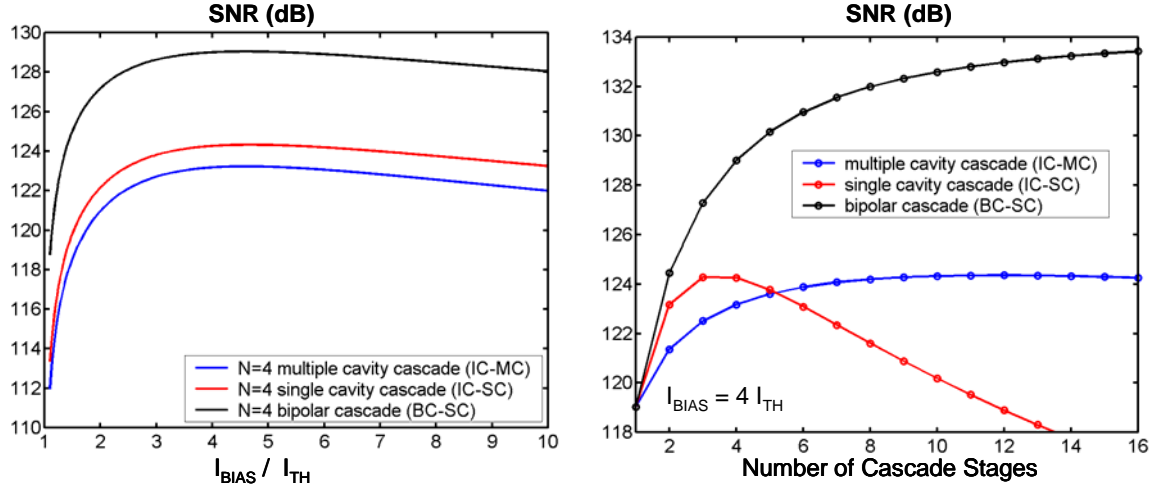


**Figure 13.** Signal-to-Noise Ratio (SNR): simulation results.

Accurate modeling of the current noise in semiconductor lasers is desired for many different applications. It is well known that high impedance suppression of the current noise in semiconductor lasers leads to photon number squeezing in the laser output – RIN below the shot noise limit<sup>2,3</sup>. However, the magnitude of the current noise is not well known and, therefore, it is difficult to predict the limits on the amount of squeezing achievable in semiconductor lasers. Accurate modeling of the current noise is also important in semiconductor cascade laser structures in which PN junctions are connected electrically in series<sup>4,5,6,7</sup>. In such devices the degree of correlation in photon emission events in different junctions depends on the magnitude of the current noise. In addition, our work has shown that high frequency current noise measurements can also be used to measure the modulation bandwidth of semiconductor lasers without using any photodetector.

Many laser noise models that have appeared in the literature simply assume statistics for the current noise from the beginning and feed these into the standard laser noise models to calculate the photon noise<sup>4,8</sup>. Such an approach is not self-consistent since a significant portion of the current noise is in fact a circuit response to the carrier density fluctuations inside the active region. In references 2 and 3 self-consistent models of the current noise in semiconductor lasers have been presented. These models assume from the start a fixed relation between the carrier density fluctuations inside the active region and the fluctuations in the potential difference across the active region. This assumption, although valid for homo-junction semiconductor lasers, does not hold for hetero-junction lasers and overestimates the current noise in the later devices. In addition, all the current noise models ignore the carrier density fluctuations inside the cladding regions. The partition noise associated with carrier recombination and carrier leakage in the cladding regions, which as we show sets the upper limit on the amount of photon number squeezing, is consequently neglected.

Under the RFLICs program we have developed a detailed model for the current noise in semiconductor hetero-junction lasers and have correlated the theoretical results with

experimental measurements. The model is fully self-consistent and includes the carrier density fluctuations in the cladding regions.

The different processes contributing to the current noise are shown in Figure 14. The noise associated with carrier injection into the active region, carrier recombination and leakage in the cladding regions, carrier capture into and carrier emission from the quantum wells, and radiative and non-radiative carrier recombination in the quantum wells is included in the model. In references 2 and 3 it is shown that the maximum amount of photon number squeezing achievable in semiconductor lasers is  $10\log(1-\eta_o)$  dB, where  $\eta_o$  is the laser output coupling efficiency<sup>8</sup>. We show that the partition noise associated with carrier recombination and leakage in the cladding regions limits the maximum amount of squeezing achievable in semiconductor lasers to  $10\log(1-\eta_o\eta_i)$  dB, where  $\eta_i$  is the current injection efficiency defined as the fraction of the total number of carriers injected into the active region that recombine in the quantum wells. This result explains the discrepancy between the maximum amount of squeezing observed experimentally (typically  $\sim 1-4$  dB after correcting for less than unity detection efficiency) and that which is calculated by ignoring the partition noise (typically  $\sim 7-10$  dB)<sup>9</sup>. In reference 10 it has been argued that non-zero current injection efficiency would not lead to increased photon noise since coulomb correlations suppress the noise associated with current partitioning in parallel resistive paths. We show that this argument does not hold in charge neutral active regions of semiconductor lasers. Figure 15 shows the calculated and measured spectral density of photon noise using the model we have developed and also using the model presented in references 2 and 3.

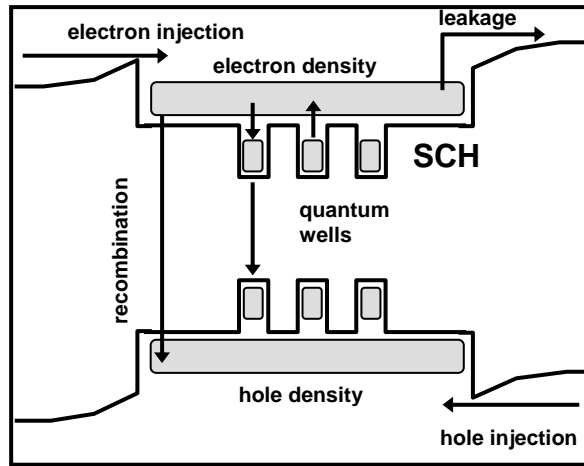


**Figure 14.** Energy band diagram of semiconductor quantum well laser showing the various processes contributing to the current noise. The carrier recombination and leakage in the SCH regions also contribute to the current and photon noise.

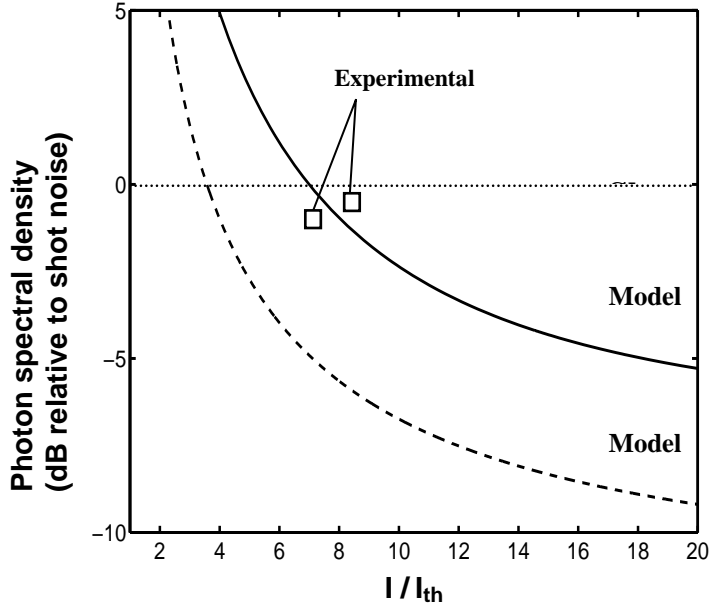


**Figure 15.** Spectral density (in dB) of photon noise (normalized to shot noise) of a 1.55  $\mu\text{m}$  laser. The inclusion of current partition noise increases the noise level by several dB above that predicted by the model presented in references 2 and 3. Boxes are the experimentally measured results in reference 11.

The analysis has shown theoretically—and is now confirmed experimentally—that a significant portion of the current noise in semiconductor lasers is a circuit response to the carrier density fluctuations inside the active region. Current noise measurements can therefore provide important information about the high frequency dynamics inside the laser. A block diagram of the experimental setup is shown in Figure 16.

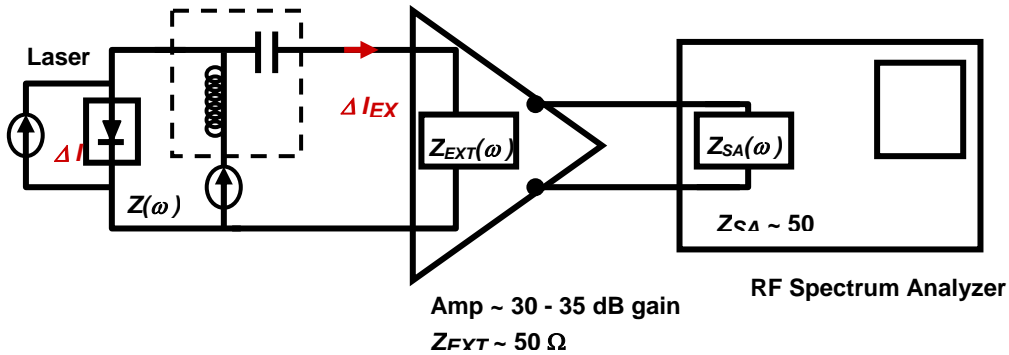


**Figure 16.** The high frequency noise on the current through the semiconductor laser is measured with an RF spectrum analyzer attached to the RF port of the bias-tee. The current noise is amplified with an LNA before entering the spectrum analyzer.

Figure 17 shows the experimentally measured high frequency current noise spectra as a function of the bias current in an InGaAsP/InP laser operating at  $1.55\ \mu\text{m}$  (Figure 18). The current noise spectra show peaks at the laser relaxation oscillation frequency. This is to our knowledge the first observation of relaxation oscillation peaks in the laser current noise. Current noise measurements can therefore also be used to study the modulation dynamics of semiconductor lasers completely in the electrical domain without using photodetectors. Figure 17 also shows low frequency measurements of the current noise. Further Figure 17 shows the noise predicted by our theory. The agreement between theory and experiment is excellent and is realized with only a single fitting parameter – the gain compression factor in the active region - across all bias currents.

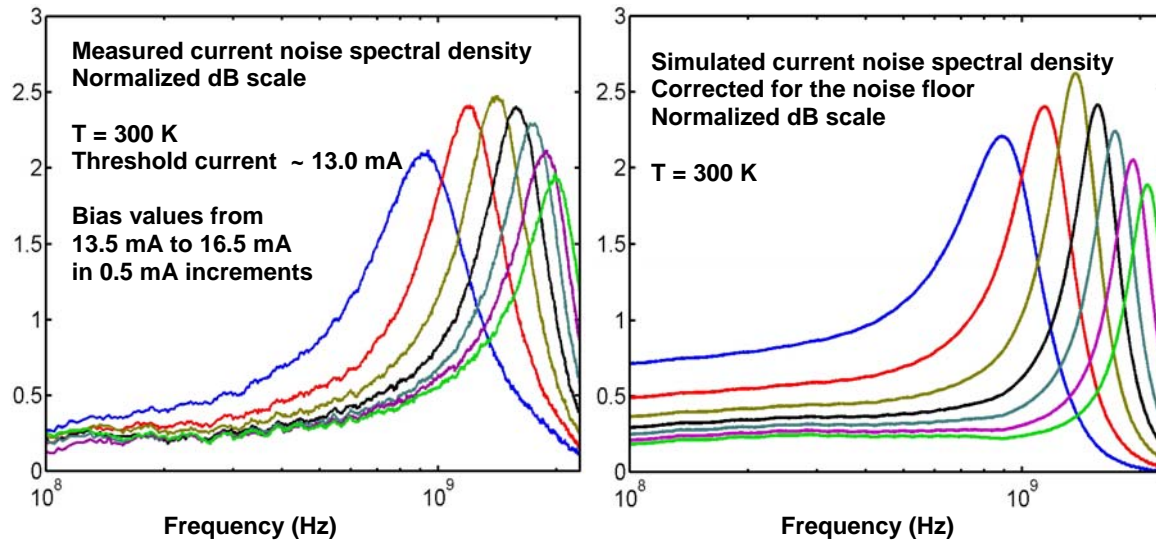


**Figure 17.** Spectra (in dB) of current noise measured at different bias currents for a  $1.55\ \mu\text{m}$  semiconductor laser. The spectra are normalized to the spectrum a little below threshold (measurement bandwidth 100MHz – 2GHz).

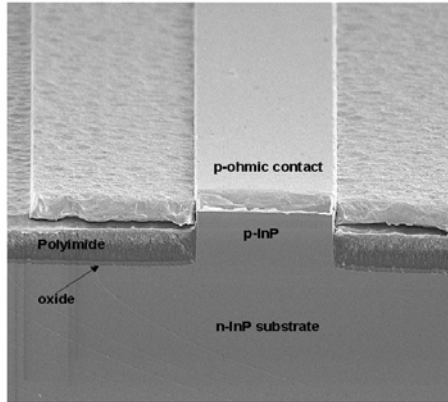


**Figure 18.** InGaAsP/InP single junction laser fabricated at MIT. This laser was used to test the hypothesis that the optical noise is being coupled back into the current noise. Epitaxial material obtained from EPI.

### *Fiber coupling*

The other major outstanding issue with the cascade laser is coupling the outputs of the multiple lasing sections into one, single-mode fiber. Consider a two laser cascade. As shown in the top half of Figure 19, without taking any specific measures for efficient fiber coupling, the light in the two lasing regions will combine to produce a two lobe pattern which has a null on axis. Therefore virtually no light will be coupled into an on-axis fiber. The reason for this is that in conventional lasers, the light is guided in the waveguide by total internal reflection. This process is shown schematically on the right hand side of Figure 20.

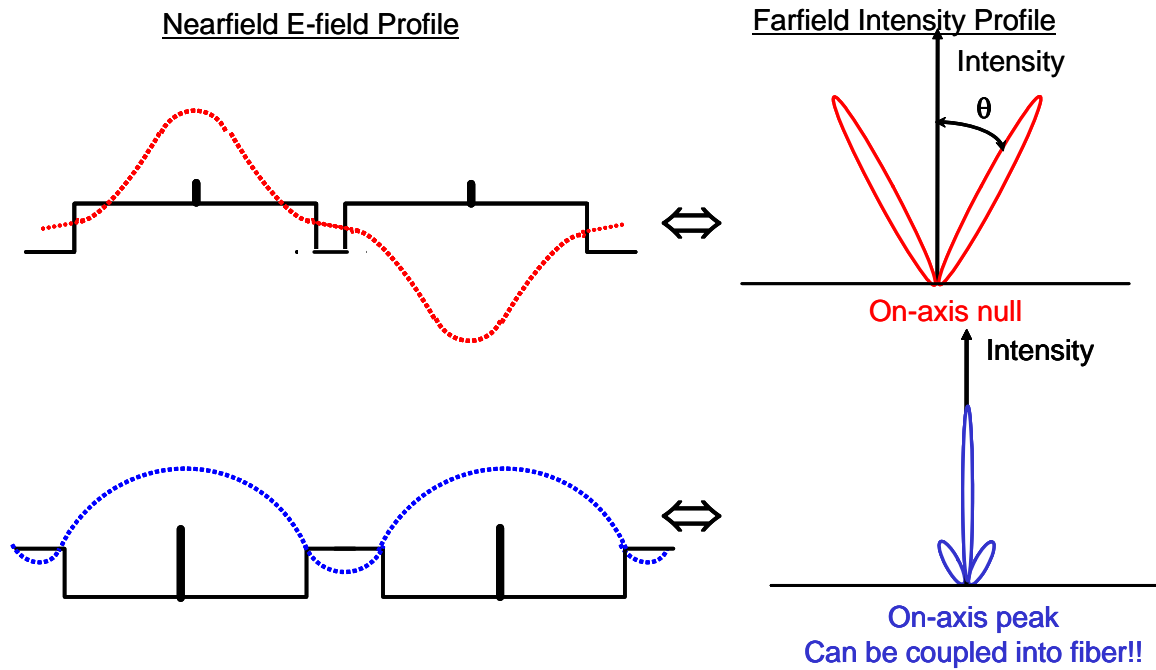


**Figure 19.** Far-field radiation patterns.

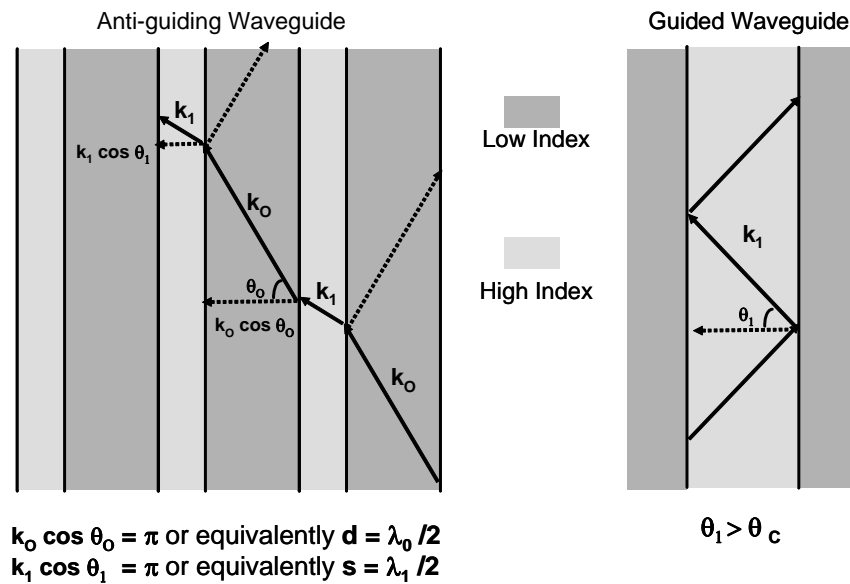


**Figure 20.** Guiding and anti-guiding waveguides.

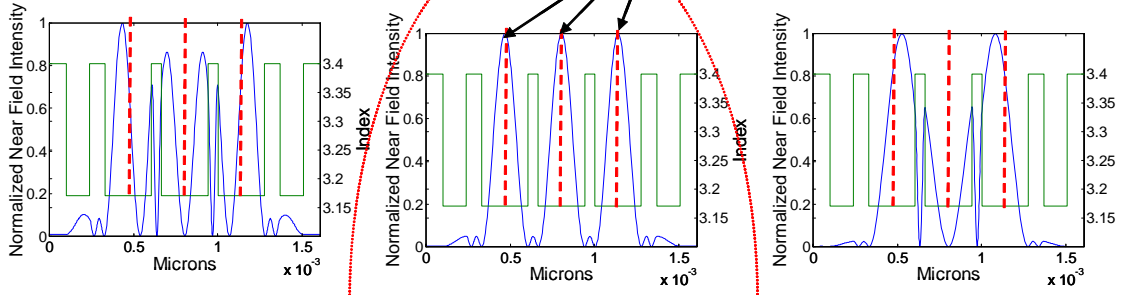
A more desirable situation is shown in the bottom half of Figure 19, wherein the beams from each laser combine to produce an on-axis maximum. It has been demonstrated that such a

pattern can be generated using anti-guiding. In this case some of the light leaks out of the waveguide at each bounce, as shown schematically in the left hand side of Figure 20, where MIT simulated using an ARROW (AntiResonant Reflector Optical Waveguide) structure for the bipolar cascade laser. An ARROW provides a high-quality beam<sup>12</sup> that has been used to couple edge emitting laser arrays for high-power applications. The optical mode of the cascade arrow has a small overlap with the tunnel junction; in fact the ARROW actually exploits these losses to ensure stable single-mode operation. The results showed that it should be possible to achieve 80% of the optical power in the two beams in the central (*i.e.* on-axis) lobe.

One of the key constraints that drove the design of the 2<sup>nd</sup> generation bipolar cascade laser was the need to achieve low fiber coupling loss while still achieving a laser with high slope efficiency. High fiber coupling efficiency implies coherent combining of adjacent optical modes in such a manner that most of the optical power is in the central lobe of the far field and there is low power in the side lobes. In the first generation bipolar cascade design the waveguides were far enough apart that the optical modes were incoherent, resulting in an on-axis null in the far field, which had low fiber coupling efficiency. Simply moving the waveguides closer together would lead to coherent coupling between the modes, but the modes would be in anti-phase, which would also result in an on-axis null.

There are two principal factors to achieving high slope efficiency. One is low optical loss within the laser cavity. This implies a low optical field where the loss is high (*i.e.* the heavily doped tunnel junctions). The second principal factor to achieving high slope efficiency is a good overlap of the optical mode with active region. These factors are also illustrated by the simulation results in Figure 21. Focusing on the near field plots, we see that for the center diagram the peaks of the optical mode do align with the active regions and that the minima align with the highly doped tunnel junctions, where the index is high.

## Near Field:



## Far Field:

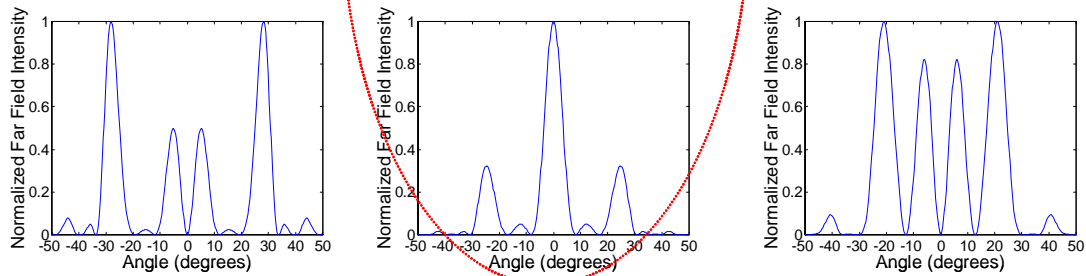


**Figure 21.** Near- and far-field patterns for bipolar ARROW cascade lasers, for three different active region and waveguide spacings.

These considerations are what led us to consider applying the ARROW structure to the bipolar cascade. In this structure, the waveguides are also close enough for coherent coupling, but in this case in an in-phase configuration, which has an on-axis peak in the far field and therefore efficient fiber coupling. Figure 21 shows the result of our simulation for the 2<sup>nd</sup> generation bipolar cascade laser we are planning to fabricate. Across the top row of diagrams are three spacings for the waveguides and active regions. Across the bottom row are the corresponding far field patterns. By adjusting the spacing, this figure makes clear that it is possible to concentrate the majority of the optical power in an on-axis (which corresponds to 0 degrees) mode.

It is imperative that the laser only lases on one mode and that that one mode be the desired one. In turn this implies that the lowest threshold current density is for the desired mode. Figure 22 summarizes the results of simulations of laser threshold gain and current for the laser design alternatives shown in Figure 21. The scale in both the graphs has been adjusted so that the curves for all three alternatives can be seen on each plot. However, the consequence of this constraint is that the curves for two configurations appear to be quite close together, when in fact there is more than sufficient distance between them to ensure that only one mode lases.



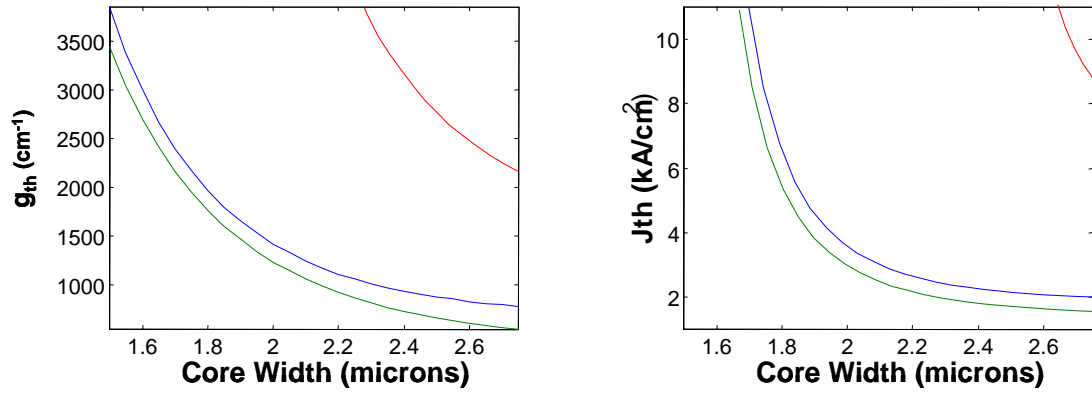
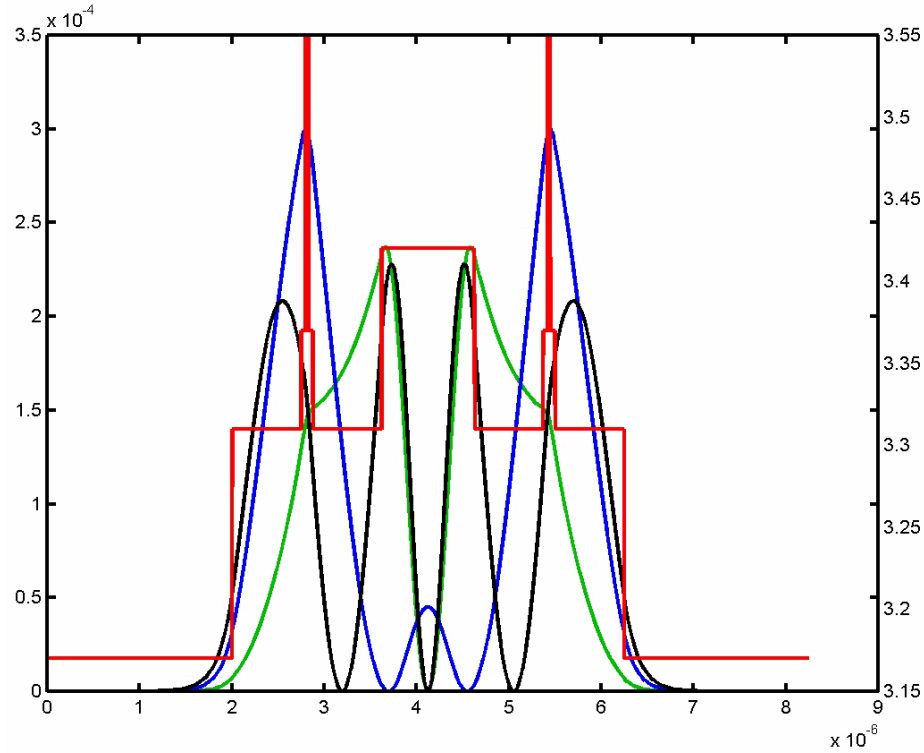


**Figure 22.** Threshold gain (left graph) and threshold current density (right graph) versus width of active region core in a bipolar ARROW cascade laser.

Professor Ram's proposed a design for the first iteration of the long-wavelength, bipolar cascade laser. The general waveguide structure is shown in Figure 23 and the growth layers are shown in

Table 2. Professor Ram and MIT withdrew from the RFLICs program with PSI. Sarnoff then initiated a design effort for bipolar cascade lasers to replace the design effort carried out by MIT. Sarnoff initiated an effort to complete design, growth, processing, and preliminary testing of bipolar cascade lasers.



**Confinement Factors :**

**Blue Mode :** 0.0145, **Green Mode :** 0.0070, **Black Mode :** 0.0074

**Figure 23.** Proposed MIT design for the first, long-wavelength bipolar cascade laser.

**Table 2.** MIT growth layers for the laser structure shown in Figure 23.

Layers	Thickness	Composition (y) Ga(x)In(1-x)As(y)P(1-y) (x ~ 0.467y)	Doping (cm <sup>-3</sup> )	Index at 1.55 μm
InGaAs Cap Layer	0.100 μm	1.00	1e19 p-type	
InP Ridge	0.500 μm	0.00	1e18 p-type	3.17
InGaAsP (cladding)	0.750 μm	0.40 (PL λ = 1.15 μm)	5e17 p-type	3.31
InGaAsP (SCH)	0.050 μm	0.55 (PL λ = 1.25 μm)		3.37
InGaAsP (QW)	0.008 μm	(Lasing at λ = 1.55 μm)		3.55
InGaAsP (barrier)	0.009 μm	0.55 (PL λ = 1.25 μm)		3.37
InGaAsP (QW)	0.008 μm	(Lasing at λ = 1.55 μm)		3.55
InGaAsP (SCH)	0.050 μm	0.55 (PL λ = 1.25 μm)		3.37
InGaAsP (cladding)	0.750 μm	0.40 (PL λ = 1.15 μm)	5e17 n-type	3.31
InGaAsP (tunnel)	0.500 μm	0.68 (PL λ = 1.35 μm)	1e18 n-type	3.42
InGaAsP (tunnel)	0.500 μm	0.68 (PL λ = 1.35 μm)	1e18 p-type	3.42
InGaAsP (cladding)	0.750 μm	0.40 (PL λ = 1.15 μm)	5e17 p-type	3.31
InGaAsP (SCH)	0.050 μm	0.55 (PL λ = 1.25 μm)		3.37
InGaAsP (QW)	0.008 μm	(Lasing at λ = 1.55 μm)		3.55
InGaAsP (barrier)	0.009 μm	0.55 (PL λ = 1.25 μm)		3.37
InGaAsP (QW)	0.008 μm	(Lasing at λ = 1.55 μm)		3.55
InGaAsP (SCH)	0.050 μm	0.55 (PL λ = 1.25 μm)		3.37
InGaAsP (cladding)	0.750 μm	0.40 (PL λ = 1.15 μm)	5e17 n-type	3.31
InP (substrate)		0.00	1e18 n-type	3.17

### 2.3 Methodology and Results: Team II - PSI and Sarnoff

#### Iteration 1

##### *Tunnel junction design and growth*

Measurements on the MIT/Sarnoff/PSI designed in-plane, long-wavelength, bipolar-cascade laser suggested that the tunnel junction used to connect the lasing regions of this device were not sufficiently localized to minimize the optical loss introduced by the heavily doped regions. Therefore an effort was undertaken to fabricate an improved tunnel junction. Sarnoff investigated an improved tunnel junction structure using an AlInAs/InP heterojunction. Using this heterojunction allows improved band offsets as well as higher bandgap material that is transparent to the laser wavelengths of interest. Additionally, for these materials *carbon* can be used as a p-type dopant in AlInAs while *silicon* can be used as an n-type dopant in InP. These dopants have much lower diffusion than the previously used zinc and selenium dopants. It is

also suspected that residual selenium from the tunnel junction growth is producing some undesired background doping during the growth of subsequent layers.

Carbon tetrachloride was used as the carbon dopant source in AlInAs. Post growth annealing under  $N_2$  is required since  $H_2$  passivates the carbon doping. Growth was optimized at  $540^\circ C$ . Under these conditions a pre-annealing doping level of  $1 \times 10^{18} \text{ cm}^{-3}$  was measured by C-V profiling. Following annealing at  $490^\circ C$  for 5 minutes under  $N_2$ , a doping level of approximately  $3 \times 10^{19} \text{ cm}^{-3}$  was measured. Doping of InP with silicon using a silane source was calibrated and doping level of  $2 \times 10^{19} \text{ cm}^{-3}$  was measured. Using these conditions, 3 tunnel junction samples were grown. One sample had 10 nm thickness for each of the tunnel junction layers while a second had 20 nm thickness for each of the tunnel junction layers. The third sample also had 10 nm thickness for each layer but with the addition of a  $1.5 \mu m$  thick layer of InP grown on top of the tunnel junction. This is to test for diffusion of the dopants under actual cascade laser growth conditions. A quarter wafer of each growth was annealed under  $N_2$ .

The three tunnel junction samples were processed into  $125 \mu m$  diameter mesa diodes for I-V testing. The best results were measured for the sample that had 10 nm thickness for each of the tunnel junction layers. These diodes showed good tunneling characteristics with negative differential resistance and a resistance under reverse bias around  $12 \Omega$ . This was higher than the previously grown InGaAs tunnel junction but still much lower than the InGaAsP tunnel junction that was actually used in the initial cascade laser growth (MIT design). The sample with the addition of a  $1.5 \mu m$  thick layer of InP grown on top of the tunnel junction showed a slight increase in the resistance to  $14 \Omega$ .

Annealed and non-annealed tunnel junction samples were sent out for secondary ion mass spectroscopy (SIMS) analysis to measure accurately the abruptness of the doping interface. The results showed that the C/Si interface was much sharper than the Zn/Se interface used in the initial cascade laser growth. There was some discrepancy with the Si doping level measurement. SIMS showed  $5 \times 10^{18} \text{ cm}^{-3}$  while we had measured  $2 \times 10^{19} \text{ cm}^{-3}$  by Hall and C-V profiling.

Another iteration of tunnel junction samples was grown trying to maximize further the doping level while minimizing tunnel junction thickness. Measurements on the first, in-plane, long-wavelength, bipolar-cascade laser suggested that the tunnel junction used to connect the lasing regions of this device were not sufficiently localized to minimize the optical loss introduced by the heavily doped regions. Therefore an effort was undertaken to fabricate an improved tunnel junction.

The approach was to see if the tunnel junction could be made sufficiently thin so that it does not adversely affect the optical loss. Since the previous 10 nm thick samples were considerably better than the 20 nm thick samples, 5 nm thick layers were used in this iteration. The carbon tetrachloride during the growth of AlInAs was increased and a post-annealing doping level of  $5 \times 10^{19} \text{ cm}^{-3}$  was measured by C-V profiling. Doping of InP with Si using a silane source was

further calibrated and doping level of  $4 \times 10^{19} \text{ cm}^{-3}$  was measured. Two further samples were grown both with and without a  $1.5 \text{ }\mu\text{m}$  thick layer of InP grown on top of the tunnel junction.

These samples were fabricated into mesa diodes and their I-V characteristics were measured. These diodes showed *worse* tunneling characteristics than the previous  $10 \text{ nm}$  thick samples!

### ***Laser design and characterization***

After Sarnoff completely characterized a small sample of the devices designed and fabricated by MIT, Sarnoff fabricated devices at room temperature with standard facet coatings. These devices do not lase in the desired mode owing, we believe, to excess losses of the current tunnel junctions. Unless the optical loss of those tunnel junctions can be significantly reduced, through the optimized materials Sarnoff has been developing, the zero<sup>th</sup> order mode will not lase with high efficiency.

Measurements of the optical emission were made in both the near and far field. Figure 24 shows the near field pattern, both laterally and vertically. The two lobes in the near field confirm that both junctions are lasing.

Figure 25 contains plots of both the lateral and transverse far field patterns. They show two lobes in the transverse direction, thereby confirming that this laser is operating in a single antisymmetric mode. The antisymmetric mode is of order 1, i.e., it has a single node. This is as distinguished from the fundamental mode with no nodes, which was not expected to lase in this laser. This is further distinguished from the next higher order mode of index 2 having two nodes, which was the mode designed to lase in this structure. To confirm that this behavior was not an artifact specific to this one device, the far field pattern of another device was measured. The results, which are shown in Figure 26, show a similar lobe pattern to the device of Figure 25.

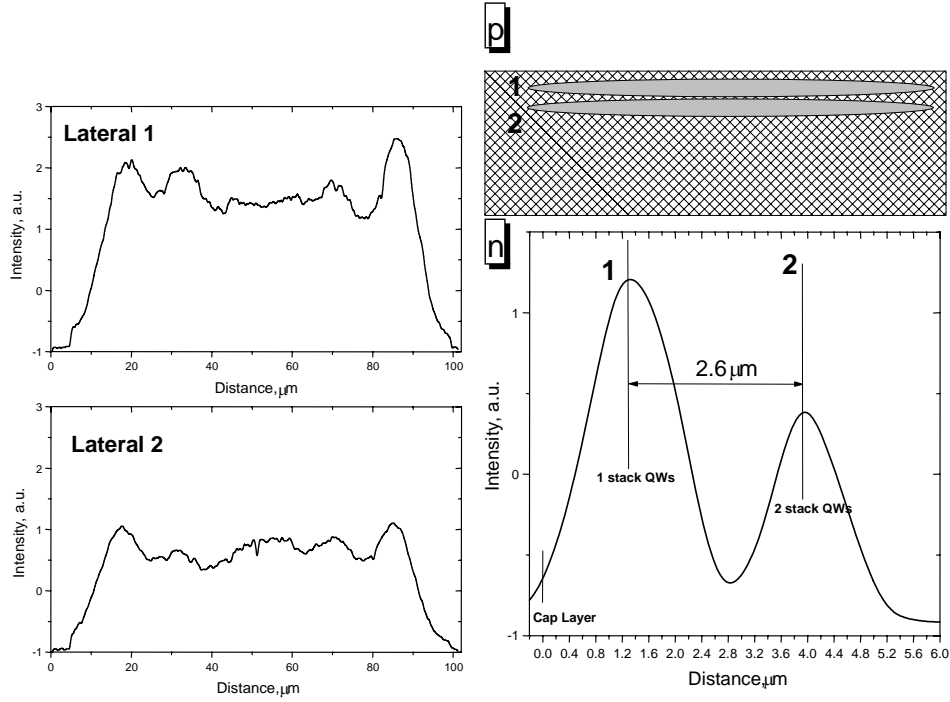


**Figure 24.** Near-field pattern of cascade laser chip H1 (100  $\mu\text{m}$  stripe, 1 mm cavity length), pulsed with 1.6 A. Transverse pattern, showing two spatial lobes, is at right, and lateral scans of the two lobes are shown at left.

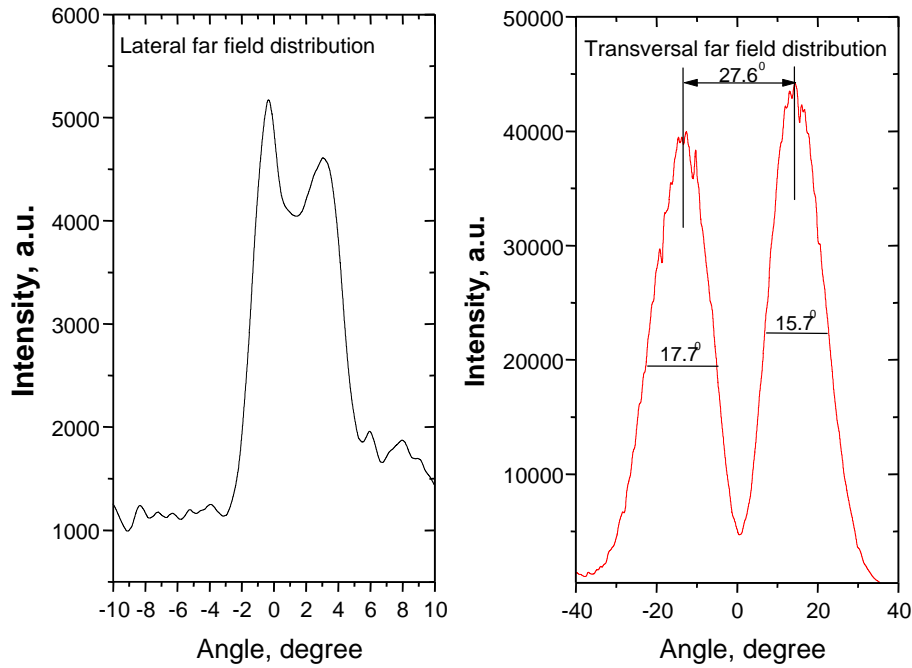


**Figure 25.** Lateral and transverse scans of the far-field pattern of cascade laser chip H1.

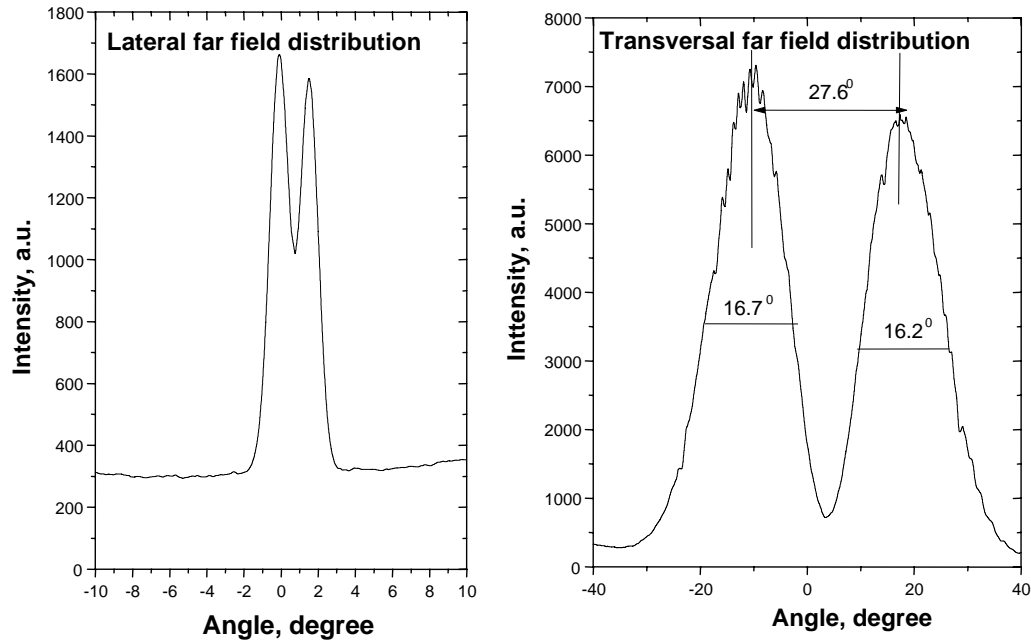


**Figure 26.** Lateral and transverse scans of the far-field pattern of cascade laser chip I6.

The fact that the MIT-designed, Sarnoff-fabricated laser operated in the antisymmetric mode 1—when the model predicted that mode 2 would have lower loss and higher gain—strongly suggests that the optical losses precisely at the tunnel junction layers were significantly higher than previously estimated. It also led to the need for tunnel junctions that are narrower. For example the heavy doping in the present tunnel junctions extends about 0.6 mm either side of the junction, which is about a factor of 50x wider than it needs to be.

Figure 27 is a plot of the optical power vs. bias current for one of the devices. The relatively high threshold current reflects both the large losses of the device and the large area as well. Figure 28 is a plot of the bias current vs. bias voltage of a similar device from the same wafer. The high voltage is to be expected since we have two lasing junctions in series. It was possible to measure this device under CW conditions. Both devices were mounted p-side down to reduce the thermal resistance and thereby improve the power dissipation.

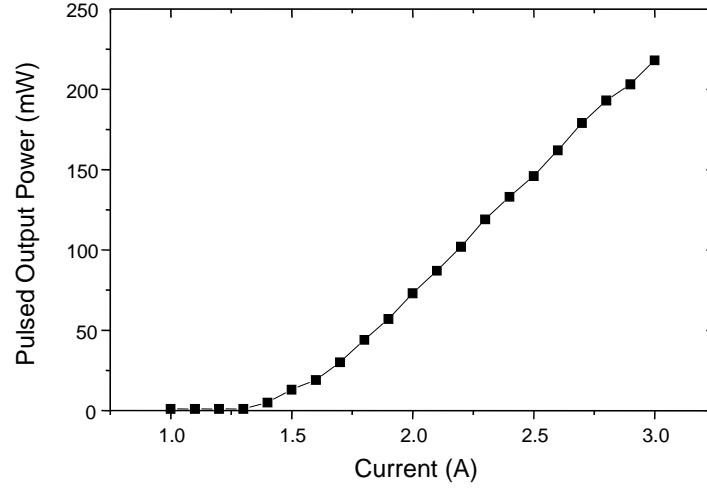


**Figure 27.** Measured P-I characteristic of cascade laser chip A10 (100  $\mu\text{m}$  stripe, 1 mm cavity length, p-side down), biased with 200 ns pulses at 25 kHz repetition frequency.

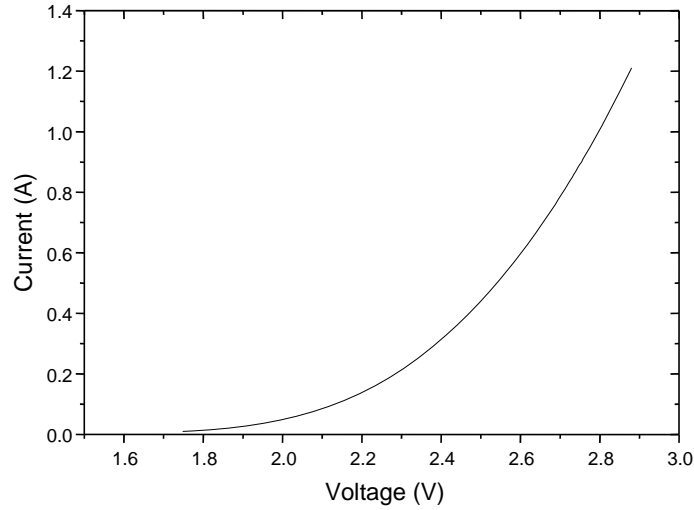


**Figure 28.** Measured I-V characteristic of cascade laser chip I6 (same wafer as A10, CW operation).

## Iteration 2

For the next iteration laser, work included three potential designs:

- #1 Node at the null of the tunnel junction
- #2 Anti-resonant (ARROW) design
- #3 “Conventional” laser (i.e., no node at the tunnel junction)



Design #1 was projected to have low fiber coupling efficiency: ~40% at best. Since link gain depends on the square of this parameter, it was necessary to rule out this design.

Design #2 (which was the basis for the MIT design) can have high fiber coupling efficiency—thereby overcoming the primary disadvantage of design #1—by placing a single lobe in the middle of the far field. Design #2 achieves this by requiring a 360-degree phase shift between emitting regions. However by delving into the details, Sarnoff uncovered several disadvantages. There is a conflict between the desire to have as narrow separation between lasing regions as possible (for efficient fiber coupling) and the limits on  $\Delta n$  imposed by the material system (which forces a wide separation). The second concern is that for the ARROW design the mode must both propagate through and radiate out of the guide. It turns out that this “lost” radiation represents a significant waveguide loss (on the order of  $50 \text{ cm}^{-1}$ ). Consequently much of the available gain is taken up overcoming these leakage losses. This led to a concern about whether this design can ever meet the high slope efficiency that was essential to the success of this program.

Design #3 would use a “conventional” laser design, which of course has the potential disadvantage of having the highly doped—and hence highly lossy—tunnel junction at the peak of the lasing mode. The approach that Sarnoff pursued to overcome this drawback was to manage the loss by making the tunnel junction very thin.

### ***Tunnel junction design and growth***

Another iteration of tunnel junction samples was grown trying to further reduce the resistance. Since lower bandgap material is generally better for tunnel junctions, we explored replacing the n-type InP with InGaAsP with bandgap wavelength of 1400 nm. Wavelengths longer than 1400 nm would be too absorbing at the laser wavelength. Doping of InGaAsP with Si using silane was calibrated and a doping level of  $1 \times 10^{19} \text{ cm}^{-3}$  was measured. Also p-type doping InGaAsP using DEZn was calibrated and a doping level of  $8 \times 10^{18} \text{ cm}^{-3}$  was measured. InGaAsP cannot be highly p-type doped with carbon since carbon is an n-type dopant in InP.

Two tunnel junction test structures were grown, one with p-InAlAs/n-InGaAsP and one with p-InGaAsP/n-InGaAsP. These two samples were fabricated into mesa diodes for I-V testing. Both samples looked similar with resistances of about  $14 \Omega$  and no negative differential resistance.

Another iteration of tunnel junctions using InGaAlAs with bandgap wavelength of 1400 nm was grown. InGaAlAs can be doped with carbon and has favorable band offsets with InGaAsP. The growth parameters for InGaAlAs with bandgap wavelength 1400 nm were determined. The doping of p-type InGaAlAs with carbon was calibrated and a doping level of  $7 \times 10^{18} \text{ cm}^{-3}$  was measured. Also n-type doping of InGaAlAs using silane was calibrated and a doping level of  $5 \times$

$10^{18} \text{ cm}^{-3}$  was measured. Two tunnel junction test structures were grown, one with p-InGaAlAs/n-InGaAsP and one with p-InGaAlAs/n-InGaAlAs.

These two samples were fabricated into mesa diodes for I-V testing. The first sample had a resistance of about  $7 \Omega$  and showed definite negative differential resistance. This is the best result to date besides the InGaAs tunnel junction sample, which was undesirable due to its absorption at 1550 nm. The second sample had a resistance about  $17 \Omega$  and showed no negative differential resistance. Very high doping levels ( $> 1 \times 10^{19} \text{ cm}^{-3}$ ) have not been achieved yet for either the 1400 nm InGaAlAs or InGaAsP. The p-type doping of InGaAlAs may be increased by using a lower V/III ratio, while the n-type doping of InGaAsP may be increased by using a lower growth temperature.

### *Laser design and characterization*

The feasibility of using the vertical ARROW structure for cascade lasers was analyzed with the help of numerical modeling. In the ARROW structure, active elements (quantum wells and surrounding waveguide layers as well as directly biased injection p-n junctions) are placed in regions with low refractive index. These regions are separated by thick layers having high refractive index. Tunnel junctions are placed inside the high refractive index layers. The precise position of the tunnel junctions should be determined in the mode structure analysis. Structures with three cascaded active regions and two intermediate high index “spacer” regions were analyzed. The optimum design was determined.

However, there are a number of problems with this design. First, there are concurrent modes that should be discriminated against by absorption in the tunnel junctions. So the composition of the thick, high index, quaternary regions needs to be very closely maintained. Second, the far field of this structure contains three lobes with only about half of the mode energy contained in the central lobe. This implies that the best the fiber coupling efficiency could be is 50%. Third, it looks very difficult to produce stripe waveguides from this sort of structure.

As a preferable alternative, a more traditional structure with three densely packed active regions spaced  $\sim 0.2 \mu\text{m}$  from each other and tunnel junctions in between was considered. This structure should generate a fundamental waveguide mode that can be effectively coupled into the fiber; in principal the fiber coupling efficiency should approach 100%. The final decision about the optimal structure depends on the level of optical losses in the tunnel junction layers. Estimations show that if the level of losses in the heavily doped tunnel layers is less than  $\sim 300\text{-}500 \text{ cm}^{-1}$ , and if there are no specific losses connected with the tunnel junction itself, this traditional design is preferable.

Using the new laser design discussed above that has three densely packed active regions spaced  $0.2 \mu\text{m}$  from each other and tunnel junctions in between a new cascade laser structure was grown. This structure should generate a fundamental waveguide mode that can be efficiently coupled into the fiber. The AlInAs/InP tunnel junction with 10 nm thickness for each layer was

used, since this produced the best tunnel junctions. Each active region consisted of 5 quantum wells with barriers. The room temperature photoluminescence had high intensity with a peak wavelength of 1556 nm. X-ray diffraction measurement results looked as expected, with good lattice matching of all layers and appropriate strain in the quantum wells.

Broad area lasers with stripe widths of 5 and 100  $\mu\text{m}$  were processed from this wafer and chips with cavity lengths of 0.5, 1.0 and 2.0 mm were cleaved. Initial testing of the lasers was conducted with the following results. First, the efficiency of the lasers was very low, less than 1%. Second, near field and far field measurements indicate that the lasers are operating in a fundamental mode. Third, the lasers all saturate at high current levels.

To narrow down the cause of the low efficiency, a laser structure consisting of one active region with one tunnel junction was also grown and processed concurrently with the cascade laser wafer. Initial testing results looked similar to the cascade laser. This indicated the problem was inherent to the structure and not due solely to the use of a large number of quantum wells. Additionally, a structure consisting of a single tunnel junction in the middle of a 1250 nm InGaAsP waveguide layer was grown. Direct measurements of optical loss on this wafer as well as a control sample consisting just of the InGaAsP waveguide are being attempted using a Metricon model 2010 prism coupler.

The investigation into what is causing the low efficiency of the cascade laser continued. Possible causes were optical loss due to the tunnel junction, high electrical resistance of the tunnel junction, and low gain from the active region for some reason. To begin validating these hypotheses, three laser structures were grown. One structure had a single active region identical to that used in the cascade laser structure but *no* tunnel junction. This was a control sample to make sure that the gain from the active region was okay. The second structure had a single active region and the p+ region of the tunnel junction used in the cascade laser structure. This should have had little electrical effect. Poor results from this sample would indicate high optical loss in the p+ layer or damage to the active region during growth of this layer. A third structure consisting of a single active region and single tunnel junction spaced 1.5  $\mu\text{m}$  apart was grown. This eliminated the effects of optical loss due to the tunnel junction and poor results from this sample should be an indication that the electrical performance of the tunnel junction is the major problem.

Concurrent with this investigation, a new cascade laser structure using an asymmetrical mode with a node at the tunnel junction was designed. In this structure, optical loss in the tunnel junction would be negligible effect. Initially, a structure with only two active regions and one tunnel junction was used. The negative effect of this design is a reduced coupling efficiency, without some form of additional optics, such as a mode converter. Consequently we viewed this as a backup to the primary bipolar cascade development path.

### Threshold current variation with temperature

Following testing of broad area lasers, the structures were fabricated into ridge-waveguide lasers with ridge widths of 5  $\mu\text{m}$  and cavity lengths of 1.0 mm. Several of the structures operated CW at room temperature. Results were similar to what was seen on some broad area lasers with thin tunnel junctions. As shown in Figure 29, the P-I curve had high slope for some region changing to a lower value at higher current as well as high threshold current (4  $\text{kA}/\text{cm}^2$ ) and high voltage. Figure 30 arranges the data in terms of the of threshold current density vs. temperature for the Sarnoff cascade lasers. Some lasers looked like they had high differential quantum efficiency, dqe, (90%) at room temperature while others showed an obvious switch-on characteristic. However, varying the laser temperature shows that it is all part of the same effect. This seems due to some sort of saturable absorber. Several of the ridge-waveguide lasers from SPIN-2 with ridge widths of 5  $\mu\text{m}$  and cavity lengths of 1.0 mm were tested at PSI. Measurement of the P-I curves gave similar results to those obtained at Sarnoff showing a high threshold current with a very high slope (snap-on) region after threshold followed by a leveling off to a high dqe region. For all cases the switch-on characteristic reduces with increasing temperature. It should be noted that dqe is still high (75%) above the switch-on region then the curve starts to roll over. The power versus current for these lasers is stable and reproducible. Further testing was conducted to determine if these lasers can be used effectively in the highest slope efficiency region.

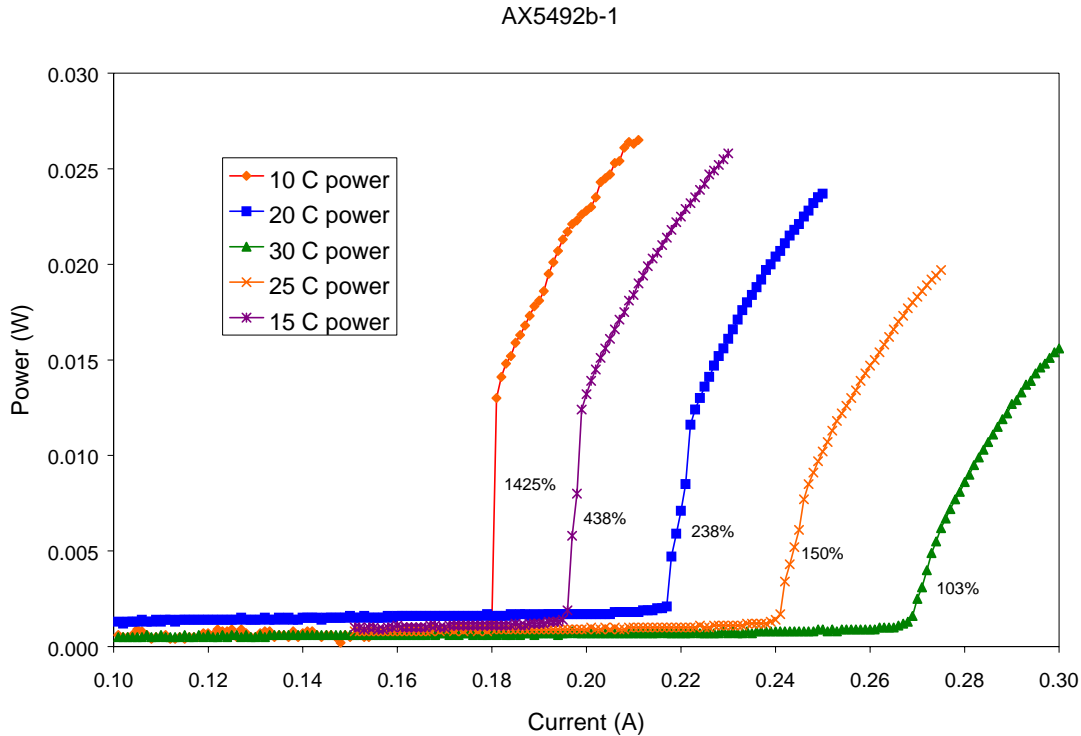


**Figure 29.** Plot of measured P vs. I curve with substrate temperature as the parameter for a fundamental mode device.

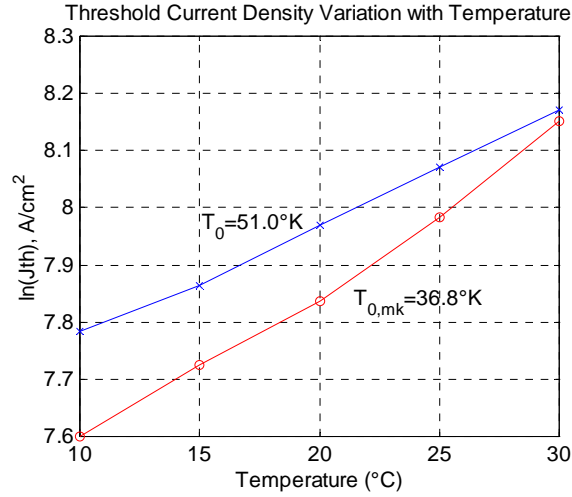


**Figure 30.** Plot of threshold current density vs. temperature for the Sarnoff cascade lasers.

Two features stand out from the analysis of the data. First, the threshold current, Figure 29, appears to be varying rapidly with heatsink temperature with  $T_0 \sim 37^\circ$ . The other factor is that the slope efficiencies for the Sarnoff lasers are  $\sim 0.4$  W/A, compared to the values of  $\sim 0.2$  W/A reported in the literature (Note: 0.78 W/A is the maximum at  $1.55\mu\text{m}$ ).

### Highest slope efficiency region

Based on the hypothesis that the high threshold and snap-on characteristic may be due to some interaction between transverse and lateral modes, very high-resolution spectral measurements were made below threshold, near threshold, and above threshold. These data for one laser is given in Figure 31 - Figure 37. The second set of curves, Figure 35, Figure 36, and Figure 37, shows the spectra over a very narrow wavelength range and clear splitting of the peaks can be seen for the spectrum taken in the high slope region.

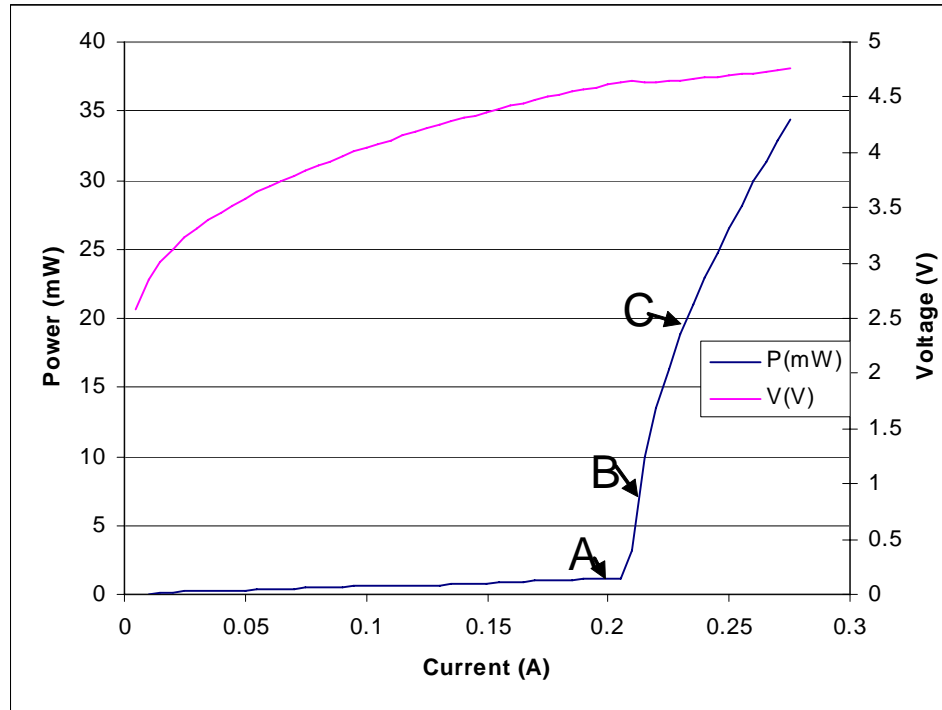


**Figure 31.** Power and voltage versus current.

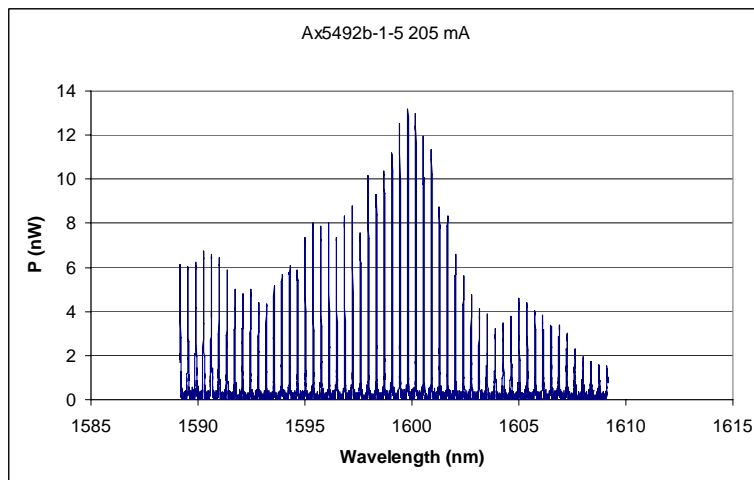


**Figure 32.** Spectra below threshold (point A in Figure 31).

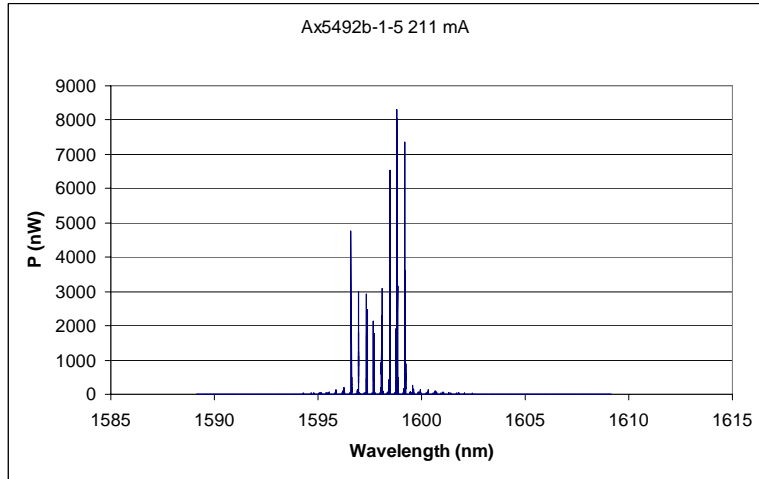


**Figure 33.** Spectra in high slope region (point B in Figure 31).

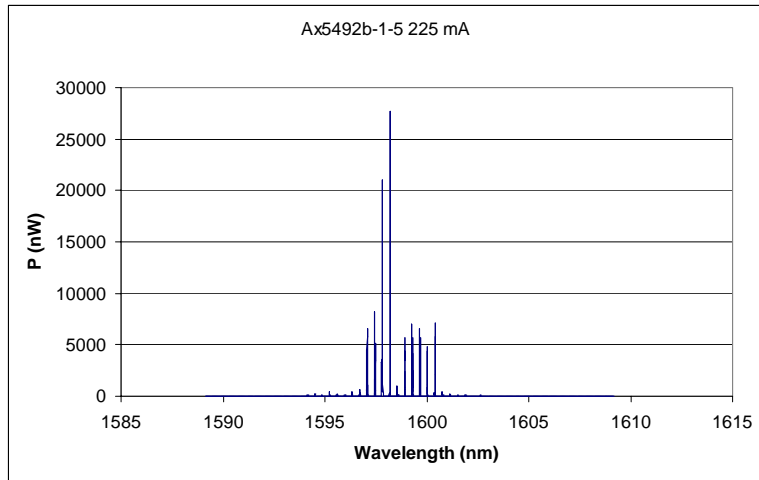


**Figure 34.** Spectra above high slope region (point C in Figure 31).

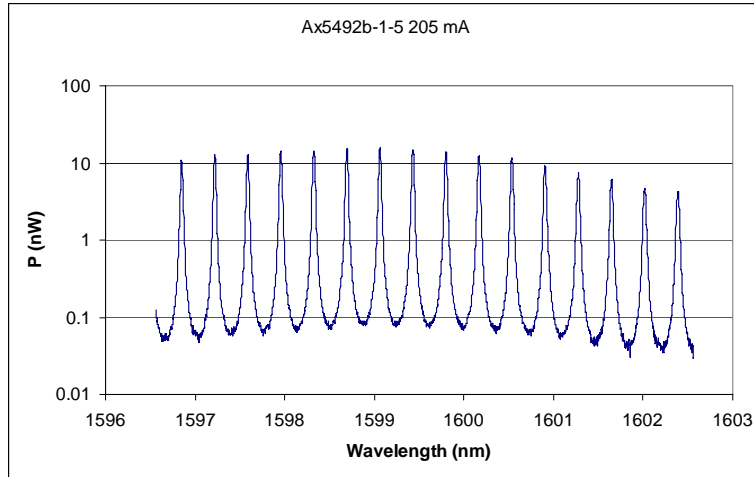


**Figure 35.** Close-up of spectra below threshold (point A in Figure 31).

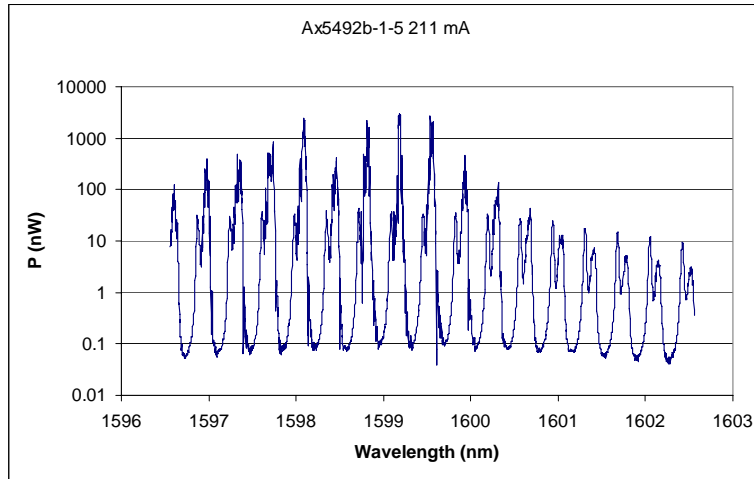


**Figure 36.** Close-up of spectra in high slope region (point B in Figure 31).



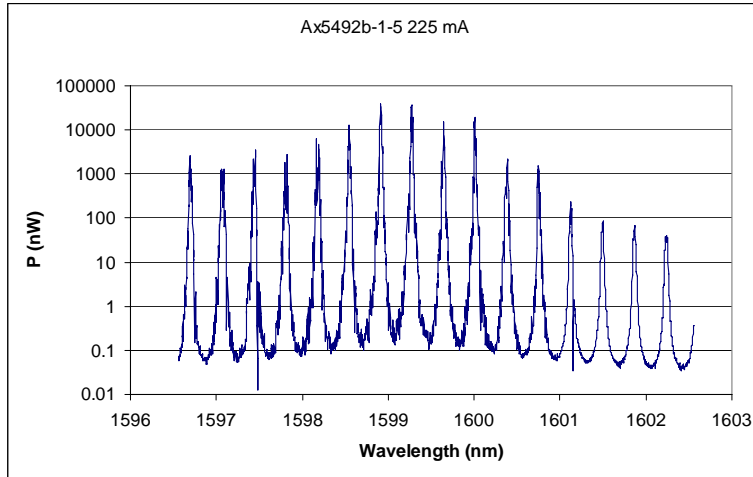


**Figure 37.** Close-up of spectra above high slope region (point C in Figure 31).

### **Laser RF frequency output**

PSI conducted further testing of the laser frequency response which showed a large oscillation in the high slope region which was not present either below or above it. The data for one laser are given in Figure 38, Figure 39, Figure 40, and Figure 41. This too implies a change of modal output of the laser around the highest efficiency region.

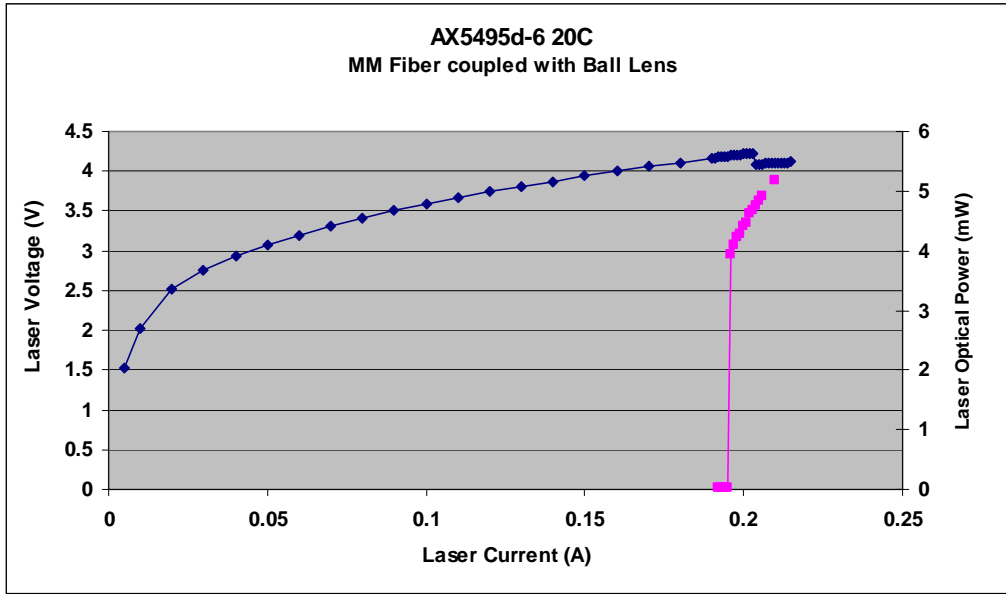


**Figure 38.** Voltage and Power versus current. This laser showed more than one mode in the vertical direction. Into multi-mode fiber coupling efficiency was about 52%.

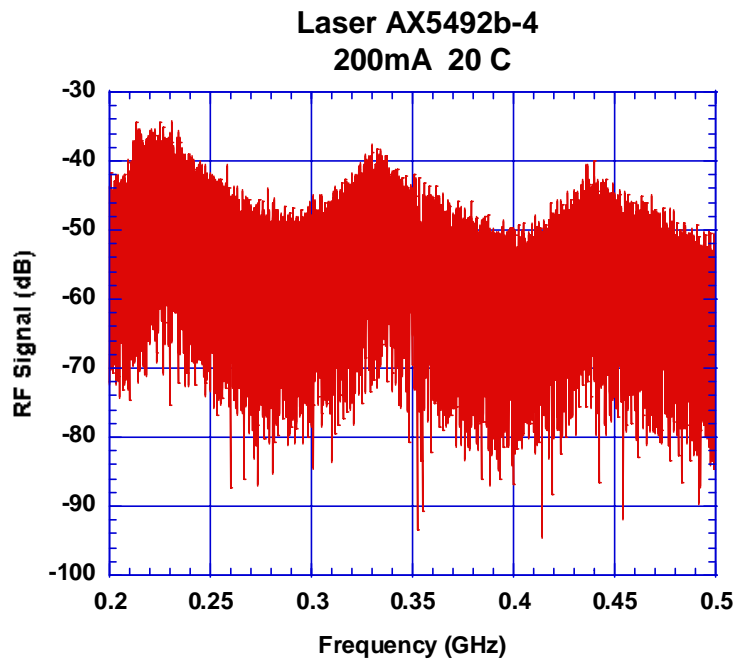


**Figure 39.** RF frequency output of same laser of Figure 38 at 200 mA.

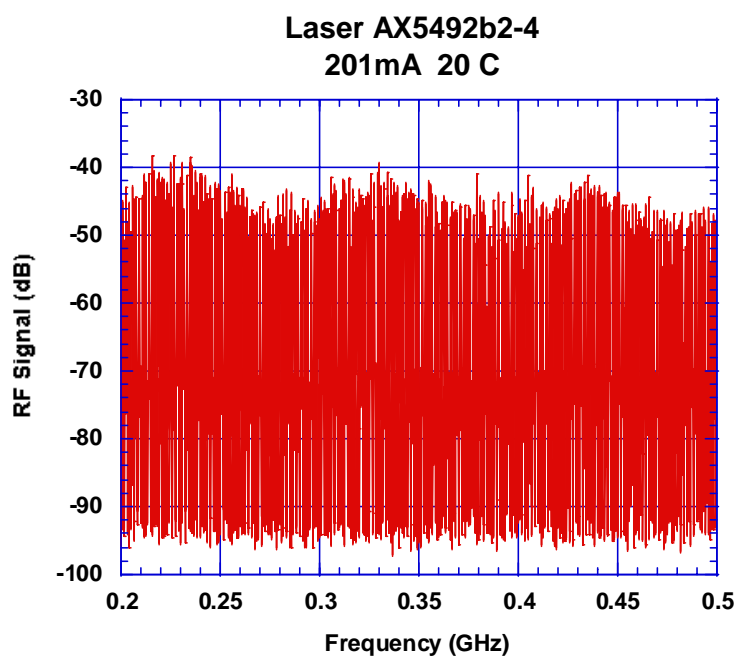


**Figure 40.** RF frequency output of same laser of Figure 38 at 201 mA.

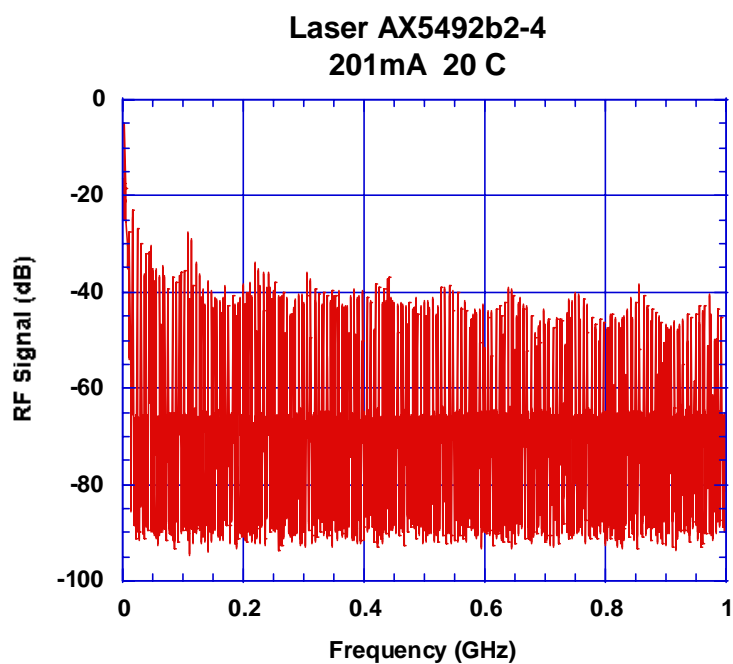


**Figure 41.** Expanded view of RF frequency output of same laser of Figure 38 at 201 mA.

The data may indicate the presence of a second non-longitudinal mode competing for gain in the lasers. The spectra above threshold show evidence of multiple transverse modes, which is demonstrated with observations of multiple maxima when coupling into single mode fibers. This may explain the high threshold, and snap-on characteristics as well as the oscillation observed by PSI. Further high resolution spectra as well as far field measurements were used to analyze the mode behavior and this information was to redesign the laser cavity for a next iteration.

### Spectral and far field measurements

High resolution spectra and corresponding far field measurements over a range of currents were used to analyze the mode behavior. Figure 42 shows the P-I curve for laser AX5492b-1-5. These data for one laser is given for different currents in Figure 43, Figure 44 and Figure 45. As seen in the data, once threshold is reached the far field maintains a normal shape. This seems to indicate that the oscillation is not due to the presence of a second lateral mode competing for gain in the lasers.

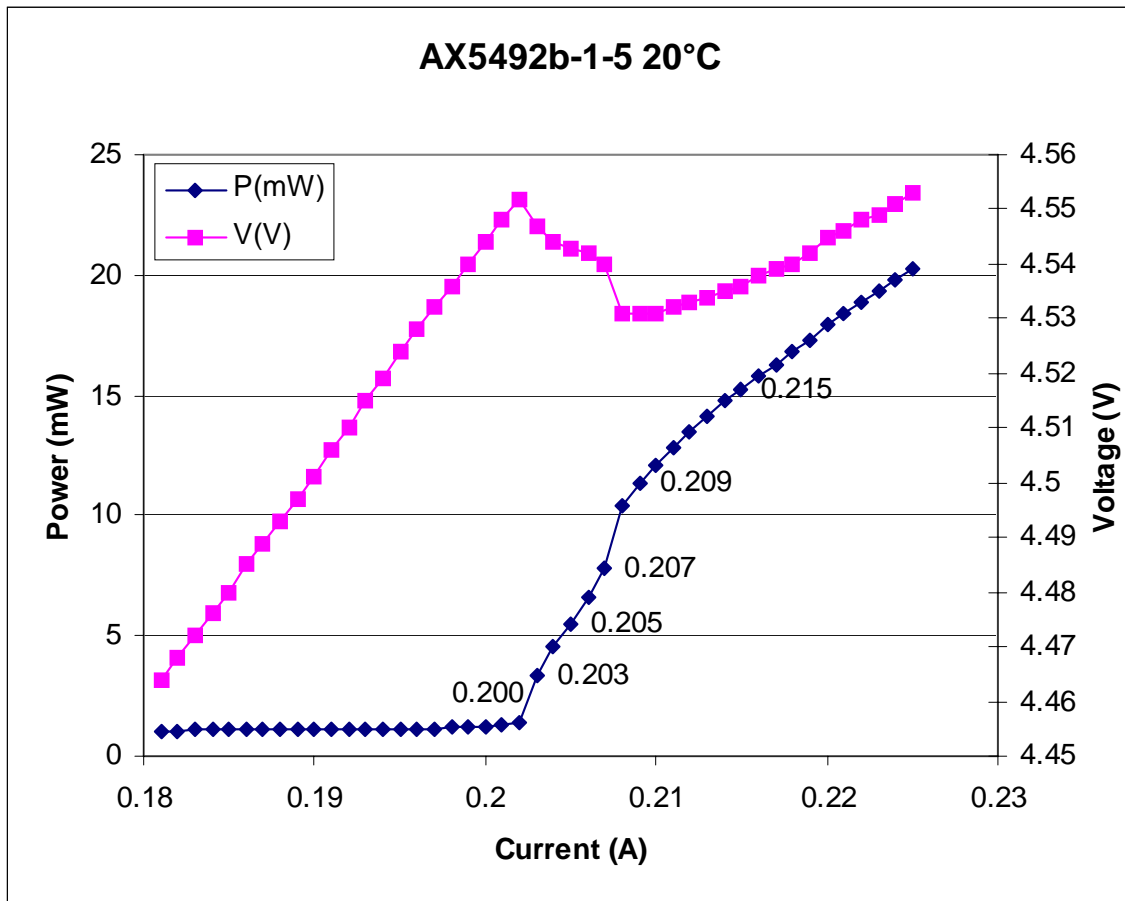


**Figure 42.** Power and voltage versus current

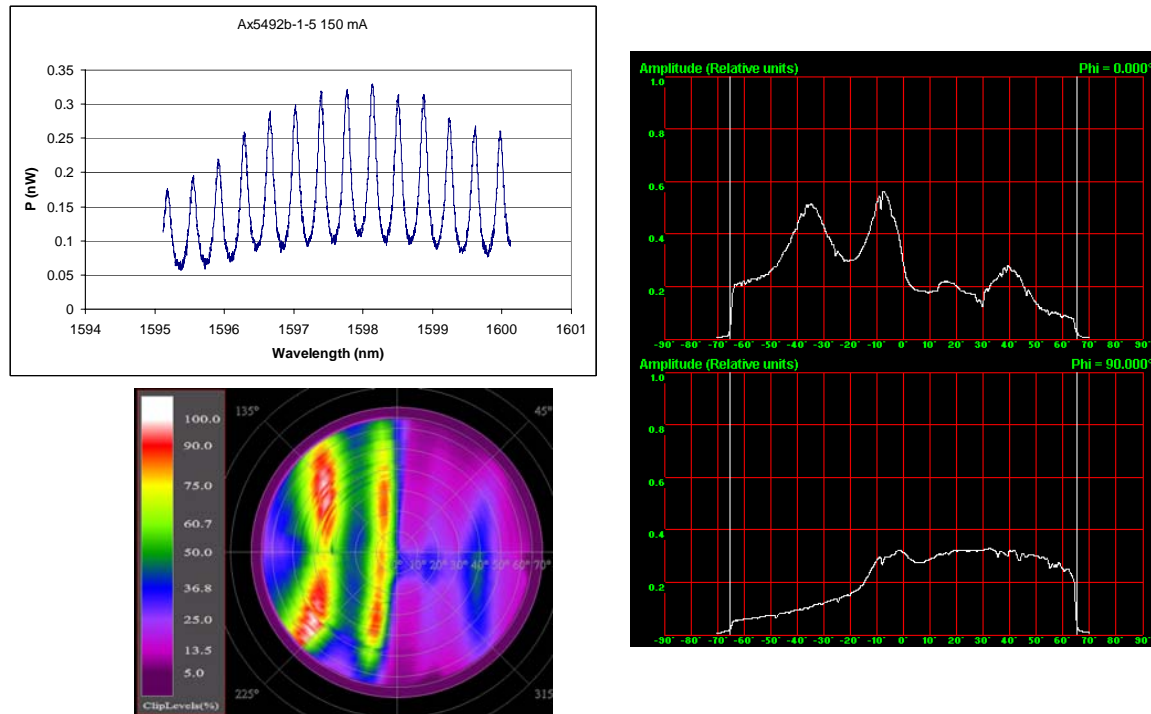


**Figure 43.** Spectral and far field measurements for a current below threshold (150 mA).

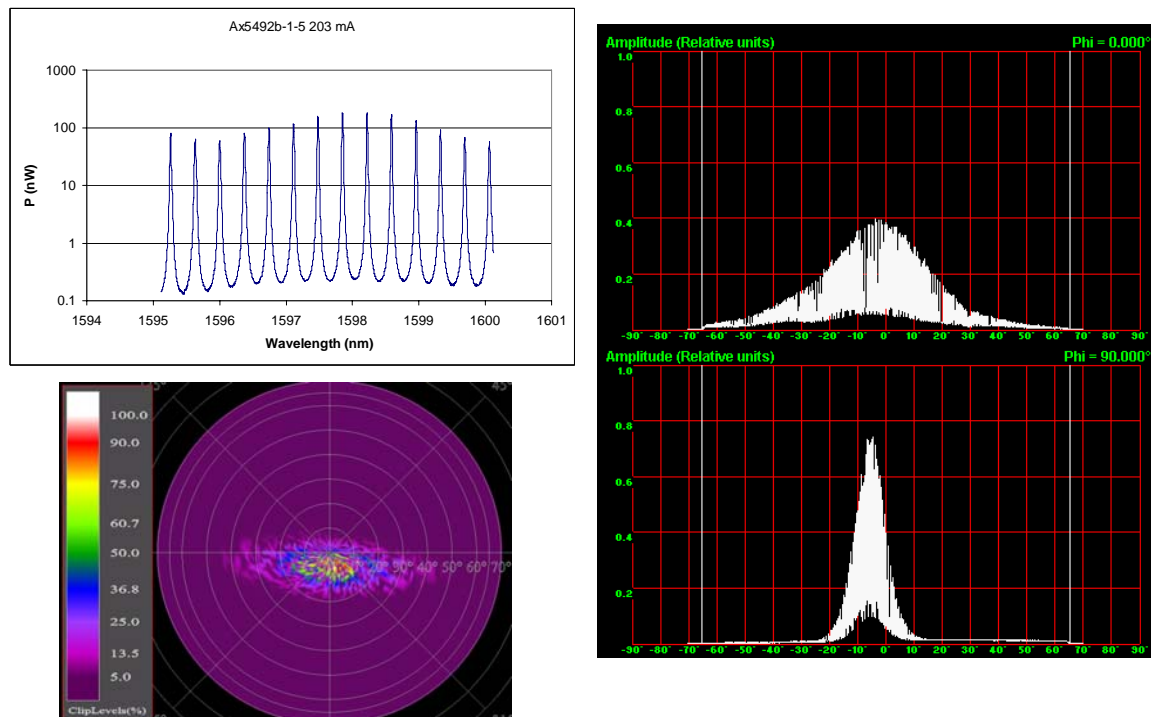


**Figure 44.** Spectral and far field measurements for a current above threshold (203 mA).

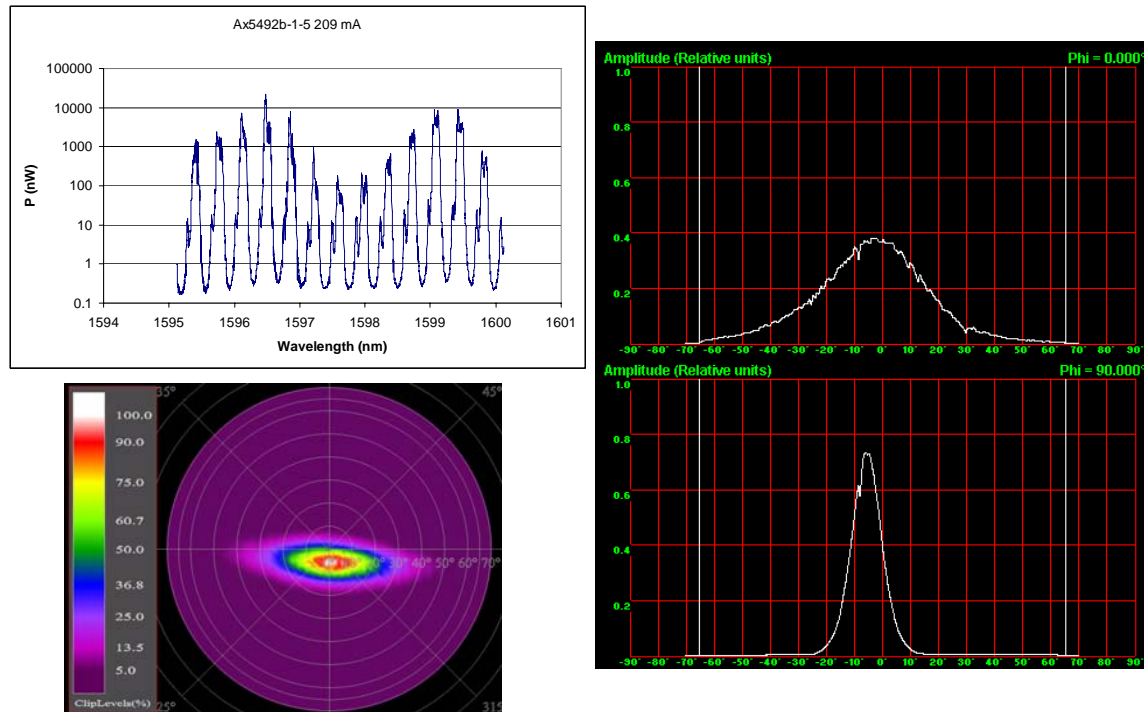


**Figure 45.** Spectral and far field measurements for a current above threshold (209 mA).

### Leakage current investigations

To test the theory that there is current leakage between the two active regions of the fundamental mode structure some testing of previous lasers was conducted. For consistency, only uncoated, broad area lasers were used. Additional cavity lengths were chipped as necessary so that each had lengths of 0.75 mm, 1.0 mm, and 1.5 mm. For most devices the dqe remained near 30% regardless of cavity length. This is an indication that optical loss is not the problem, supporting the current leakage theory.

A method to reduce possible current leakage was determined. The asymmetric mode laser has a much thicker (5X) barrier between the two active regions which would explain why it performs as expected. Modeling showed that the internal cladding for the fundamental mode structure can not be made much thicker and still maintain the fundamental mode. A better alternative is to use InAlAs instead of InP for the internal p-cladding. InAlAs has higher bandgap and better band offset to prevent current leakage.

### High threshold investigations

It was theorized that the characteristics (snap-on, high threshold current) of the previous laser iteration were caused by high resistance of the thin (10 nm total) tunnel junction leading to a large electric field and electro-absorption at the tunnel junction. To test this theory a cascade laser wafer with thicker tunnel junction (20 nm total) layers was processed into ridge-waveguide lasers with ridge widths of 5  $\mu\text{m}$  and cavity lengths of 1.0 mm. This tunnel junction has been shown to have good electrical characteristics (low resistance) and was used in the anti-symmetric mode laser which performed as expected. The P-I and I-V data for one laser is shown in Figure 46. As expected, the electrical properties were improved. The snap-on characteristic was completely eliminated and  $V_{\text{th}}$  was reduced to about 2.5 V. However the dqe was low at 25% and the threshold current was still very high.

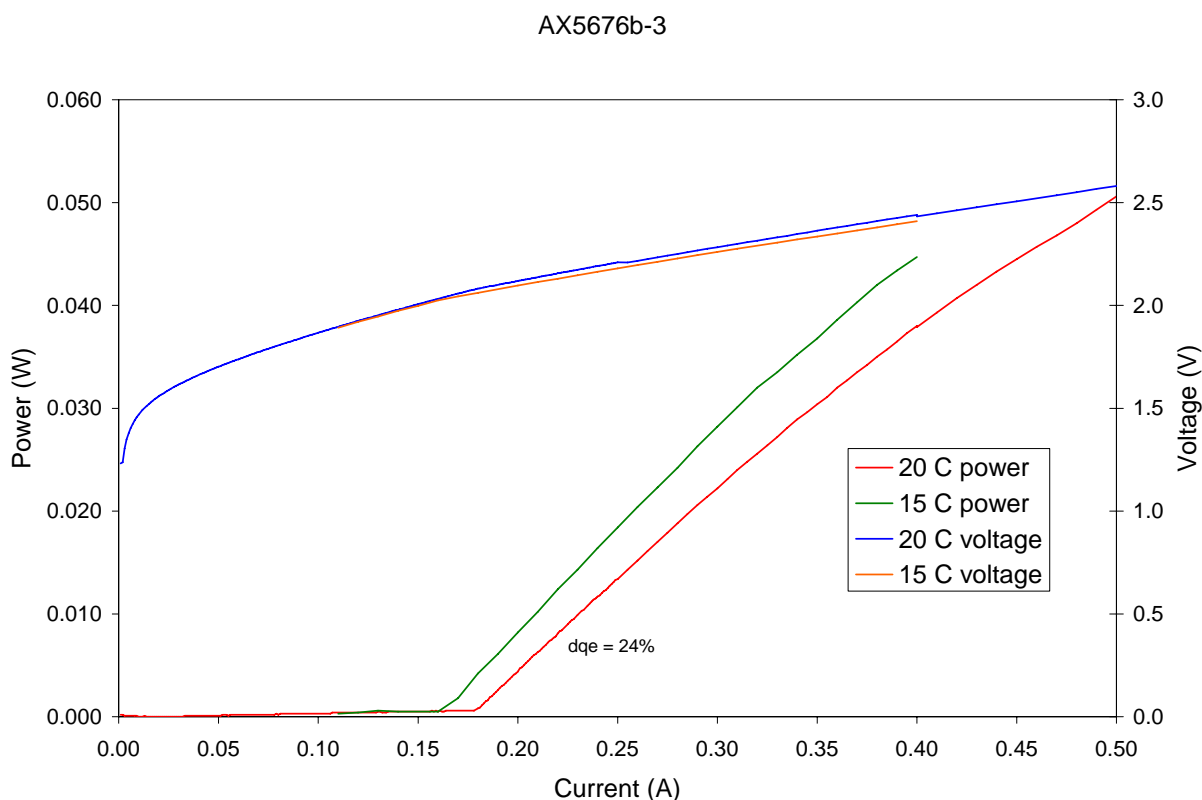


**Figure 46.** P-I and V-I curves of a ridge waveguide laser in anti-symmetric mode.

This result would be consistent with increased optical loss due to the tunnel junction. If in the laser with snap-on, the thin (10nm total) tunnel junction is fully depleted giving high resistance but also low loss, then when the tunnel junction has even a small amount that is not depleted the optical loss could be very high. This would mean there may still be some optimum thickness of the tunnel junction between 10 and 20 nm. However, analysis shows that 10 nm of highly doped material should not provide free carrier absorption that would lead to this significant optical loss.

Also the internal cladding layers surrounding the tunnel junction should not be able to provide the necessary loss either. This analysis is shown in Figure 47.

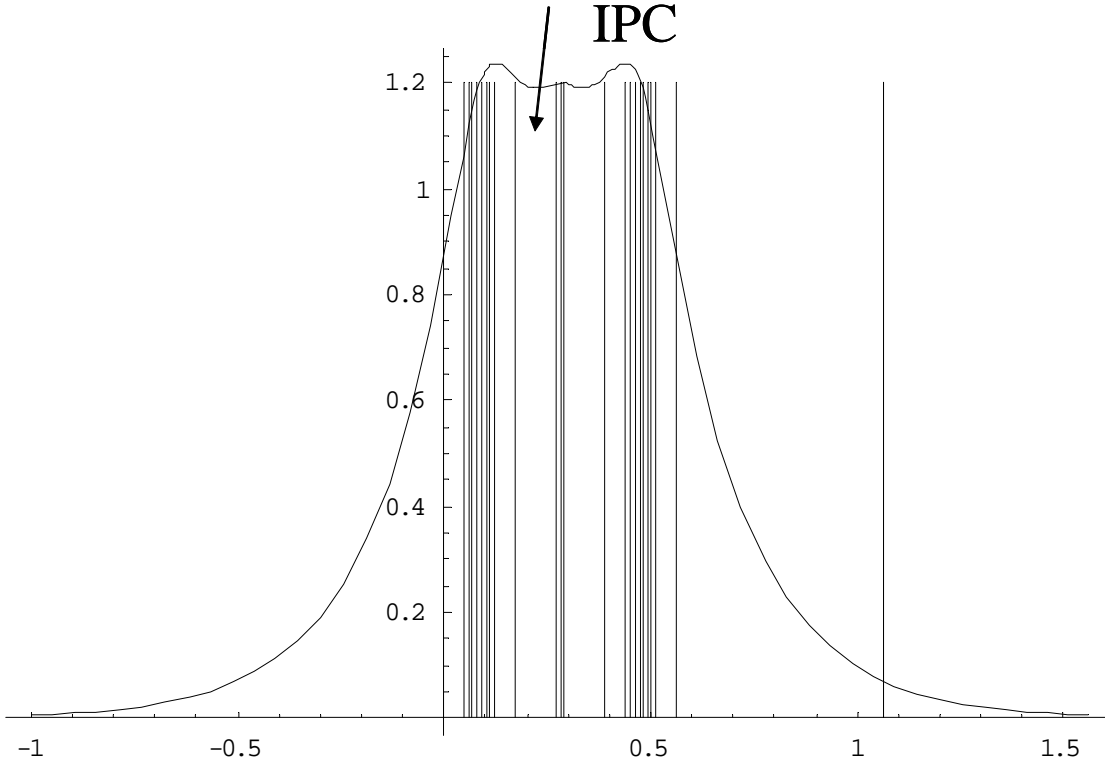


**Figure 47.** Mode intensity distribution in a cascade laser structure. The Internal P-cladding (IPC) is marked by arrow.

Confinement factor for the IPC is  $\sim 0.11$  and for tunnel layers (TL) themselves are  $\sim 0.02$ . The free carrier absorption in the IPC is  $\sim 20\text{-}30\text{ cm}^{-1}$ , and in the TL is  $< 100\text{-}200\text{ cm}^{-1}$ . Therefore the total absorption losses are  $\sim 5\text{-}7\text{ cm}^{-1}$ . To explain our value of the effectiveness, we need to account for additional losses of  $20\text{-}30\text{ cm}^{-1}$ . The conclusion is that free carrier absorption in the tunnel junction and p-cladding cannot explain low efficiency.

### Iteration 3

#### *Tunnel junction design and growth – reduction of leakage current*

A new structure using InAlAs instead of InP for the internal p-cladding was investigated as a way to reduce possible current leakage between the active regions as explained in the previous



monthly report. InAlAs has higher bandgap and better band offset to prevent current leakage. InAlAs composition and doping were calibrated and a laser structure incorporating the InAlAs layer was grown. Additionally, during the calibration for this growth it was observed that the photoluminescence for the 1400 nm wavelength n+ InGaAsP used for the tunnel junction had a large band tail extending past 1550 nm. In order to remove this as a possible source of absorption, n+ InP with doping of  $2 \times 10^{19} \text{ cm}^{-3}$  was substituted in some structures. Four wafers were grown as follows:

- AX6059: Fundamental mode cascade with InAlAs for internal p-cladding.
- AX6061: Fundamental mode cascade with InP:Si for n-tunnel junction layer.
- AX6062: Single active region laser with 100 nm InAlAs for first part of p-cladding.
- AX6063: Fundamental mode cascade with both the InAlAs p-cladding and InP:Si n-tunnel junction.

### ***Laser design and characterization***

#### **Broad area lasers**

These wafers were processed initially as 50  $\mu\text{m}$  stripe broad area lasers. Chips with cavity lengths of 1.0 mm were tested. Only the lasers from AX6063 showed an increase in dqe to 56% (28% from one uncoated facet). Also the threshold current and threshold voltage were much better than previous fundamental mode structures at 600 A/cm<sup>2</sup> and 2.1 V respectively. In order to determine the effects of optical loss, different cavity lengths of 0.25, 0.5, and 2.0 mm were also tested for AX6063. This gave further improvement for 0.5 mm cavity length to 84% (42% from one uncoated facet). The dqe and electrical properties of these lasers are much closer to what is expected for a laser operating in bipolar cascade mode. Data for these devices are shown in Figure 48.

## AX6063 Cascade Lasers

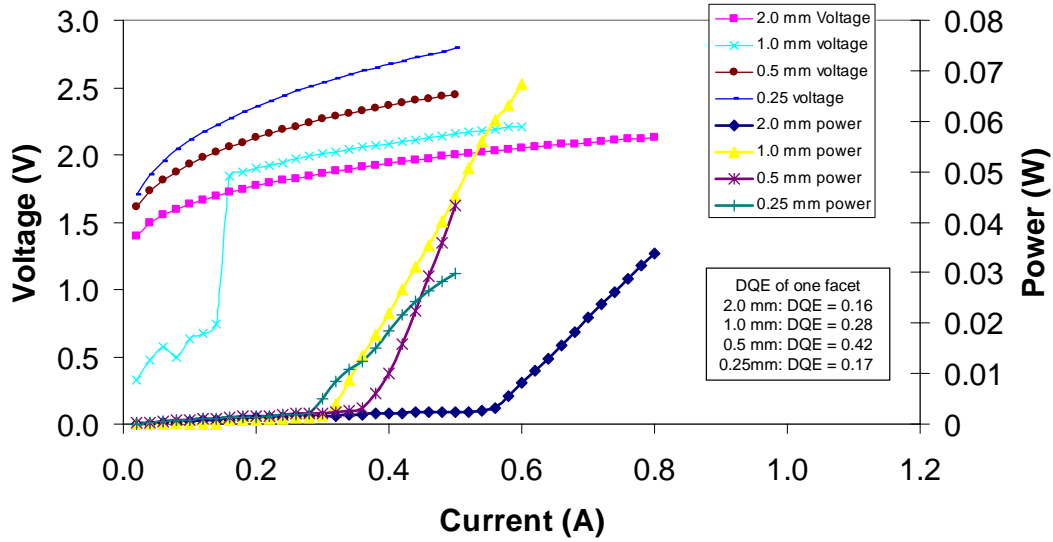


**Figure 48.** DQE and electrical properties of 50  $\mu\text{m}$  stripe broad area lasers

### Ridge waveguide lasers

Another sample of the material which showed high dqe as broad area lasers (AX6063) during the last reporting period was processed as ridge waveguide lasers. Ridge width was 3  $\mu\text{m}$ . The first type to be tested has both facets uncoated. Various cavity lengths are being tested. For the uncoated devices with cavity length of 0.5 mm, dqe as high as 76% (38% from one uncoated facet) was measured at 20  $^{\circ}\text{C}$ . Data for these devices is given in Figure 49 and Figure 50. Threshold current and threshold voltage were 4.7  $\text{kA}/\text{cm}^2$  and 2.2 V respectively.

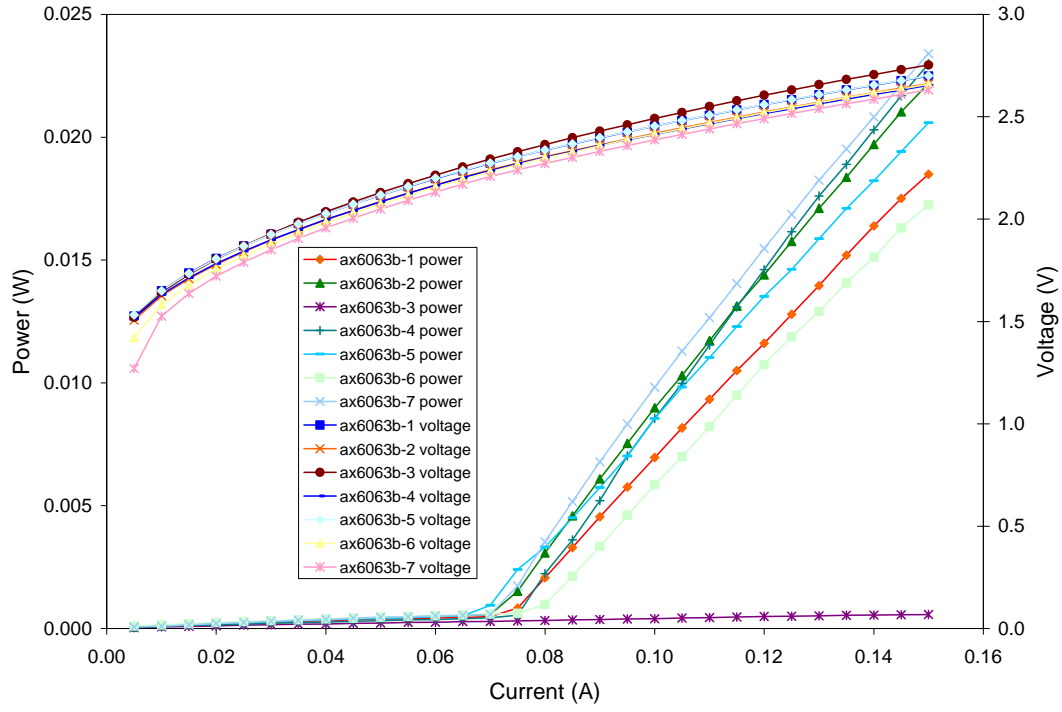


**Figure 49.** Ridge waveguide lasers with 2 active regions. These devices are uncoated with cavity length of 0.5 mm.

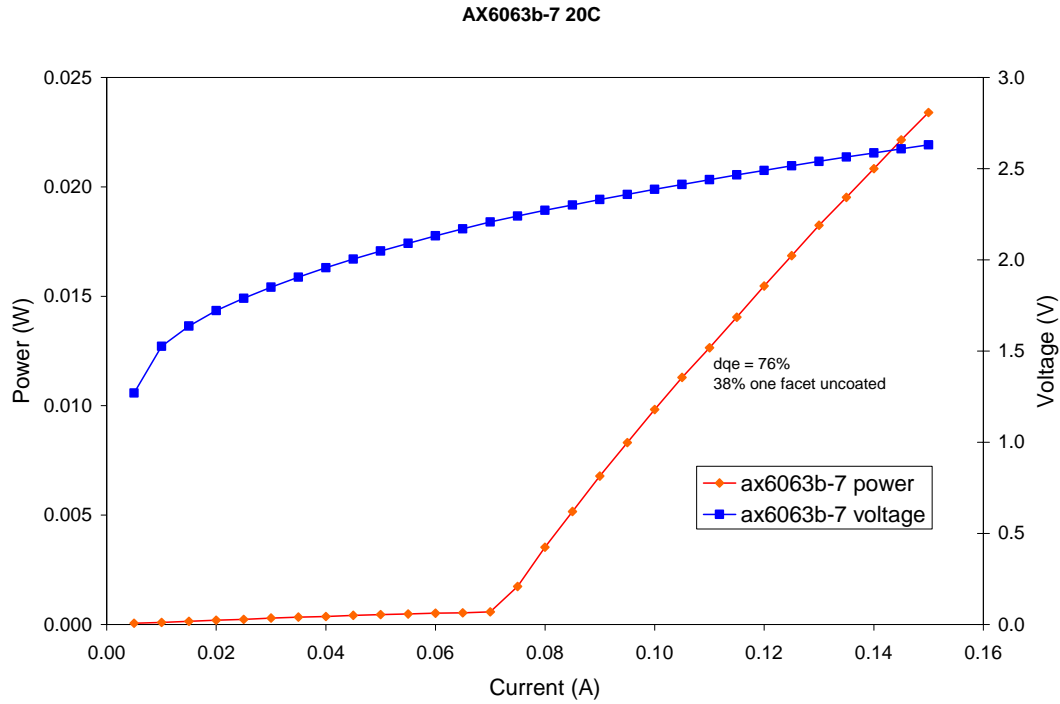


**Figure 50.** Ridge waveguide lasers with 2 active regions. These devices are uncoated with a cavity length of 0.5 mm. This laser has a high dqe of 76%.

Further 3  $\mu\text{m}$  ridge waveguide lasers from the previous best material (AX6063) were facet coated (HR 97%/AR 3%) and tested. For 0.5 mm cavity lengths the dqe measured at 20  $^{\circ}\text{C}$  was less for coated devices than uncoated, 52% as opposed to as high as 76% (38% from one uncoated facet). The P-I and I-V characteristics were measured over a range of temperatures from 0 to 50  $^{\circ}\text{C}$  are shown in Figure 51. The dqe improved with lower temperature to 66% at 0  $^{\circ}\text{C}$ . Near field measurements showed that current spreading was minimal. The conclusion is that there was still some leakage of current between the active regions. There may also have been optical loss related to the internal cladding and tunnel junction. It is possible that dqe of coated devices could be further improved by optimizing the cavity length and facet coating but the test of this was slated for the next growth iteration.

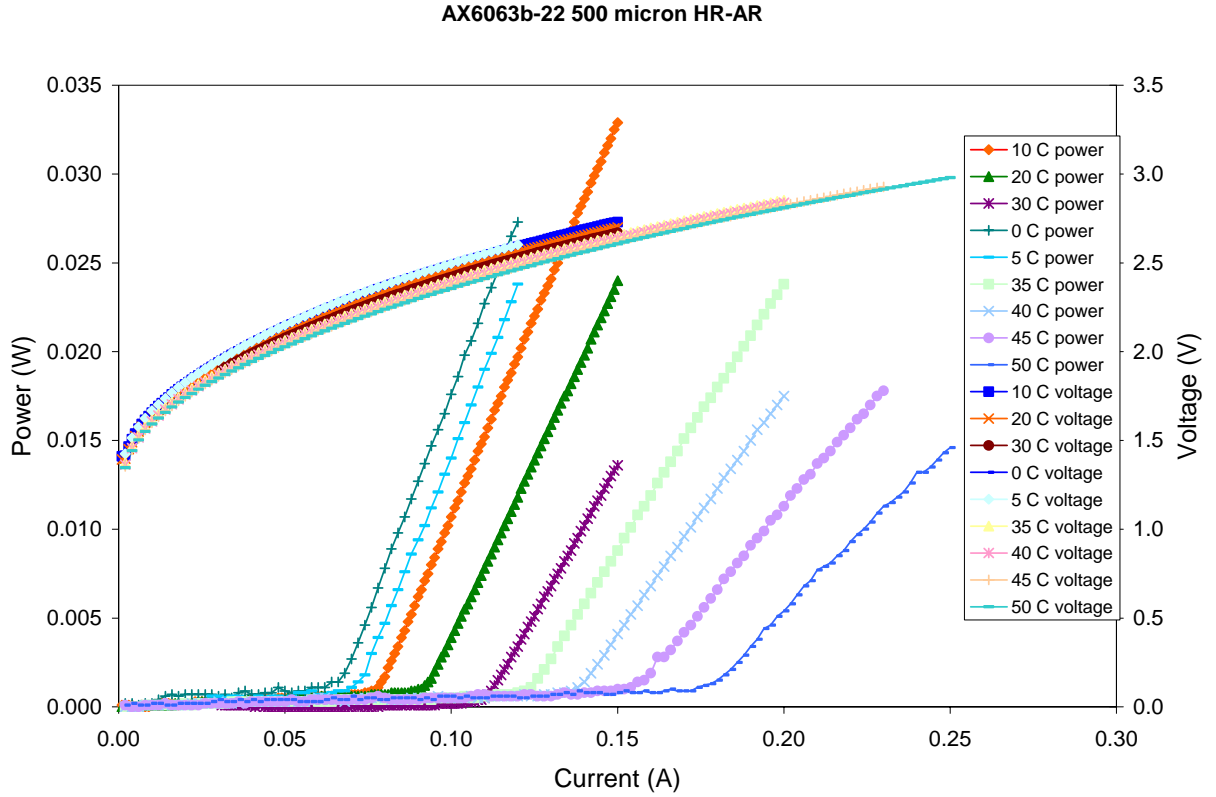


**Figure 51.** The P-I and I-V characteristics were measured over a range of temperatures from 0 to 50 °C of a 3  $\mu\text{m}$  ridge waveguide laser with HR 97%/AR 3% coatings.

## Iteration 4

### *Laser design and characterization*

#### **Optimization of bipolar cascade laser**

A final growth iteration of the cascade laser was completed. Four variations of the structure were grown as follows:

AX6190: Same as AX6063 (best performing 2 active region laser) but with 3 active regions instead of two.

AX6191: Same as AX6190 but with a 10 nm thick  $\text{In}_{0.80}\text{Ga}_{0.20}\text{P}$  high bandgap current blocking layer inserted after the upper confinement layer of each of the first two active regions. This is to eliminate leakage between the active regions.

AX6192: Same as AX6191 but with reduced thickness of the internal cladding layers.

AX6193: Same as AX6191 but with reduced doping in the internal cladding layers and slight reduction of the tunnel junction thickness.

These last two variations are to further reduce optical loss and current spreading but may have a trade off with increased current leakage between the active regions.

The four growths from the final iteration were processed into 3  $\mu\text{m}$  wide ridge waveguide lasers. Uncoated chips with 0.5 mm cavity length were tested. All of the devices had very high voltage. This was a problem since many devices reached the 5 V maximum of our system before lasing. This was the case with all devices from AX6191 and AX6193. Voltage should be higher of course for three active regions but not so high. AX6190 and AX6192 lased but only with dqs of 40% and 60% respectively. After some analysis it was discovered that the critical process step of annealing the wafers under nitrogen before processing had been omitted. This is necessary to activate the carbon doping in the p+ InGaAlAs layer of the tunnel junction. Without this step the resistance of the tunnel junction should be very high. This explains the high voltage. AX6192 was probably best because the high resistance of the tunnel junction was likely causing excessive current spreading which the thinner internal cladding was designed to reduce. Unfortunately, the wafers cannot be annealed after processing. The unprocessed parts of the wafers were annealed and processed.

The four growths from the final iteration were reprocessed into 3  $\mu\text{m}$  wide ridge waveguide lasers with the correct annealing step before processing. However, this did not change the results significantly. All of the devices still had high voltage at threshold indicating high resistance. This high resistance increases current spreading, heating and carrier leakage. The most likely explanation is some MOCVD (Metalorganic Chemical Vapor Deposition) growth problem with the tunnel junction layers leading to a poorer interface. The best results were for devices from AX6191. This was the three active region structure with a 10 nm thick  $\text{In}_{0.80}\text{Ga}_{0.20}\text{P}$  high bandgap current blocking layer inserted after the upper confinement layer of each of the first two active regions. Uncoated chips with 0.5 mm cavity length showed dqe of 78% (39% from one uncoated facet) with cooling to 0°C. HR/AR coated chips with 0.75 mm cavity length showed dqe of 57% at 10°C. Measuring the same devices pulsed gave dqe of 79% at 20°C indicating that heating due to the high resistance is a major issue.

### **Frequency performance of cascade laser**

A goal of the RFLICs program was to demonstrate the frequency response of a cascade laser. Figure 52 shows the frequency response of a laser AX6036b-23, a fundamental mode cascade laser with two active regions of three quantum wells each. This laser has a 3  $\mu\text{m}$  wide ridge and is 500  $\mu\text{m}$  long with HR/AR coating. The laser package shown in Figure 53 is not optimal for high frequency performance. Figure 54 shows that the packaging has a major roll-off starting at 4 GHz. The frequency dependence of the package was removed from the overall laser performance and is shown in Figure 55.

The ridge waveguide laser and packaging was not in the optimal configuration. The electrode has excess capacitance. Therefore, the roll-off at low frequencies ( $<5$  GHz) is not inherent to the cascade laser. Since the RFLICs funding for this work has been spent, any follow-on work to with this type of cascade laser can provide a better understanding of the true limitations of this device. Other more expensive design practices appropriate for higher frequency should be implemented.

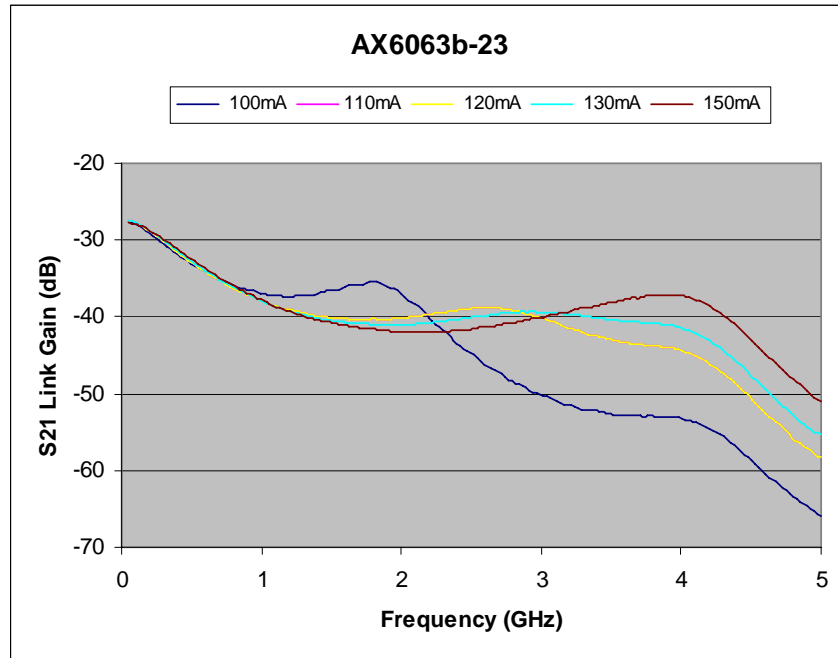


**Figure 52.** Frequency response of two active region cascade laser.

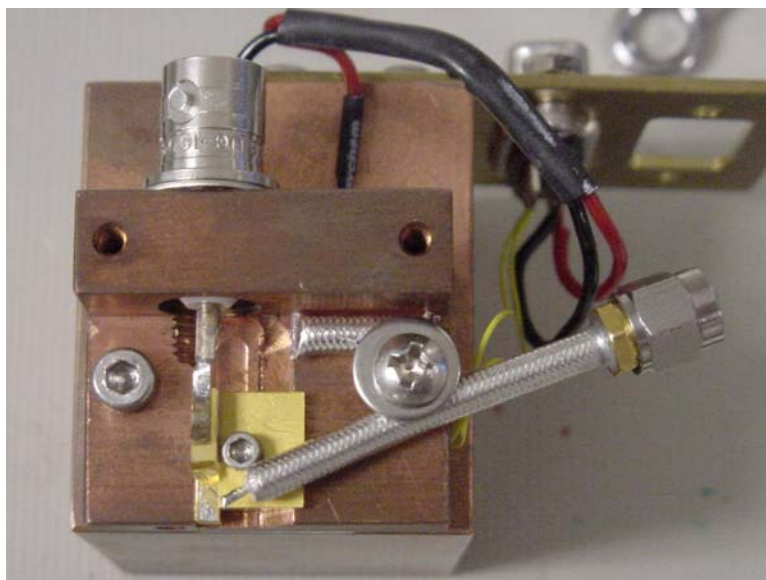


**Figure 53.** Laser in lab configuration package

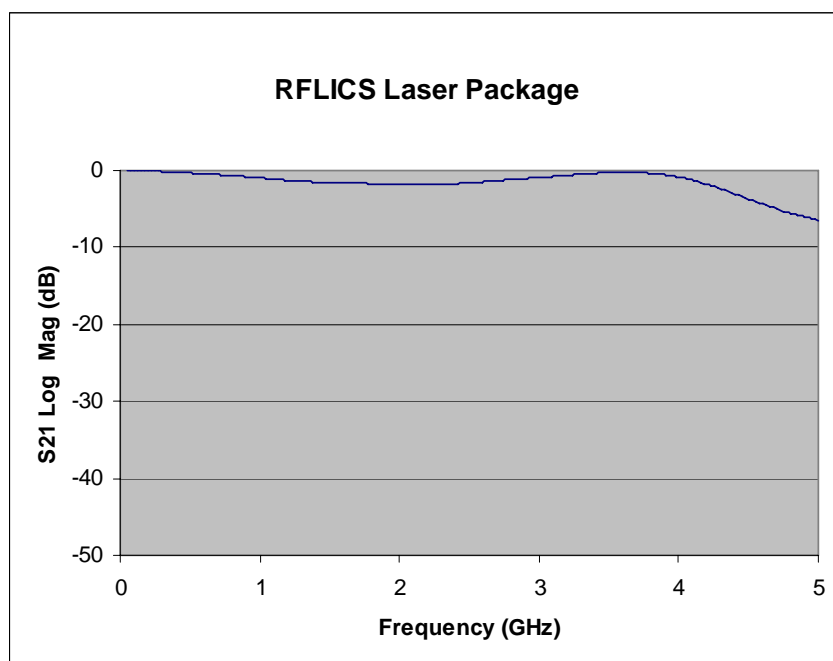


**Figure 54.** Frequency response of laser package.



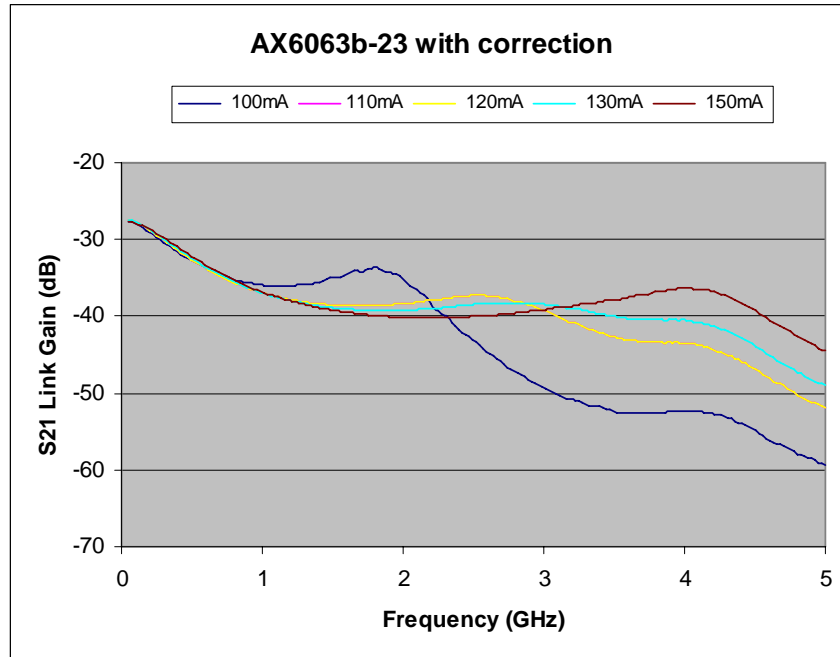


**Figure 55.** Frequency response of two active region cascade laser without the package response.

## 2.4 Conclusions

This program was motivated by the desire to develop high-performance RF photonic links using an innovative device approach called the *cascade laser*. The ideal cascade laser has a slope efficiency of  $>1$  W/A, is monolithically manufactured and easily coupled to a fiber. We investigated the bipolar cascade laser. As stated before, the first step in determining a better cascade laser was to review and understand cascade laser technology to date. We tried to overcome some of the limitations to obtaining high slope efficiency, which are listed below:

- Intracavity optical loss
- Fiber coupling efficiency
- Carrier leakage over heterobarrier
- Non-radiative recombination
- Temperature dependence of carrier confinement
- Materials issues

Collaborating with Sarnoff Corporation, Photonic Systems, Inc. (PSI) developed a Bipolar Cascade Laser that achieved a slope efficiency of 0.5 W/A by forcing the link's input RF signal to feed a series-connected succession of multiple laser junctions whose optical outputs are collected in parallel to illuminate the link's single photodetector. This laser utilized vertically stacked active regions separated by tunnel junctions in a single optical cavity. Since vertical stacking does not allow for the heatsink to scale as the number of cascade sections, the maximum number of cascade sections is limited to three. These lasers had limited slope efficiency due to the excess optical loss in the tunnel junction. Also, it was difficult to fit many laser layers within a thin single transverse mode waveguide.

### 3 External Modulation

#### 3.1 Introduction

The RFLICs program goal as stated in the BAA was, “In the case of a Mach-Zehnder type modulator, achieving a  $V\pi$  in the range of 0.1-0.5 Volts would result in zero RF insertion loss with the 1-10 mW of optical power available from conventional laser diode sources.” For the conditions of  $P_{in}=10$  mW,  $R_m=40\Omega$ , and  $\eta_d=0.9$  A/W, the maximum allowable optical insertion loss could be:

- 1.0 dB for  $V\pi=0.5$  V
- 3.2 dB for  $V\pi=0.3$  V
- 8.0 dB for  $V\pi=0.1$  V

To obtain such a high-speed modulator, the design begins with the selection of what physical effect will be used to achieve modulation and a selection of the material in which this effect will be produced. Many recent efforts have focused on exploiting either of two electroabsorptive effects (Franz-Keldysh or quantum-confined Stark effects) in semiconductors, because such devices are readily integrated with a CW semiconductor laser source. Many commercially available modulators use the linear electro-optic Pockels effect, either in a semiconductor, in a polymer material, or in  $\text{LiNbO}_3$ . This effect allows modulation of the phase of the light, and an interferometer converts the phase modulation to intensity modulation.

The most common type of interferometer used for phase to intensity conversion is a Mach-Zehnder (MZ). The slope efficiency of a MZ modulator is inversely proportional to  $V\pi$ , the voltage required to swing between constructive and destructive interference. With a  $V\pi$  on the order of 0.1 to 0.5 V and a conventional 10 mW semiconductor laser, a link gain of 0 dB can be achieved. The best performing MZ modulators are made with  $\text{LiNbO}_3$  due to the long device lengths that can be achieved maximizing the RF/optical interaction length, thus minimizing  $V\pi$ . These long device lengths are possible in  $\text{LiNbO}_3$  since the optical waveguides have very low attenuation ( $\sim 0.1$  dB/cm). Before the beginning of RFLICs, NRL<sup>13</sup> demonstrated the lowest  $V\pi$  for a  $\text{LiNbO}_3$  MZ modulator of less than 2 V for frequencies up to 1 GHz. Although other materials such as semiconductors and polymers can have a stronger Pockels effect than  $\text{LiNbO}_3$ , their optical insertion loss has prohibited them from having as low effective  $V\pi$  as  $\text{LiNbO}_3$ .

Under this program regarding external modulation, we took two approaches. The first approach involved working with Rick Osgood of Columbia University to identify new materials with excellent electro-optics properties to produce a modulator with a lower  $V\pi$  than that demonstrated thus far in a standard  $\text{LiNbO}_3$  MZ. This work involved investigations of thin lithium niobate and thin barium titanate. The second approach involved improving or developing modulation techniques. We initially began with the vertical Fabry-Perot (FP) modulator, a modulator geometry that was enabled by the ability to produce thin lithium niobate developed by our team member Professor Osgood. However, within a few months of the start of the contract, we realized that there was a fundamental sensitivity-bandwidth tradeoff for the vertical FP that precluded ever achieving simultaneously the RFLICs  $V\pi$  and bandwidth goals. Subsequently, PSI attempted to identify a new novel modulator. Several different modulator configurations

were analyzed via a PSI developed computer model. After a series of iterations and down selections, one modulator design – the broad-bandwidth resonant (BBR) design – was found to theoretically meet the RFLICs goals.

### 3.2 *Electro-optic Materials*

PSI and Columbia have investigated types of modulators that might be realized in various inorganic materials ( $\text{BaTiO}_3$  and  $\text{LiNbO}_3$ ) and identifying those that have the greatest potential for satisfying the RFLICs goals of  $V_{\pi,eq} < 0.3 \text{ V}$  and  $f_{3dB} > 50 \text{ GHz}$ . As the result of this investigation, we identified two modulator approaches that we considered to be our baseline approaches. These two approaches are: 1) a mode conversion modulator in  $\text{BaTiO}_3$ , and 2) a MZ modulator in  $\text{LiNbO}_3$ .

#### **Mode conversion modulator in thin high r-coefficient material**

Element  $r_{51}$  of the electro-optic tensor matrix of the inorganic material  $\text{BaTiO}_3$  is 820 pm/V, which is about a factor of 27 larger than the  $r_{33}$  of  $\text{LiNbO}_3$ . Unfortunately, because  $r_{51}$  is an off-diagonal element of the matrix, an applied voltage doesn't produce a simple optical phase change that can be converted to intensity modulation in an interferometer, but rather it induces coupling between the waveguide's orthogonal TE and TM modes. Thus the only type of modulator one can fabricate in  $\text{BaTiO}_3$  that exploits the magnitude of the  $r_{51}$  tensor element is a *mode-conversion* modulator (sometimes called a *polarization* modulator), which has to be followed by a passive polarization filter in order to convert the polarization modulation into an intensity modulation that can be directly detected.

Barium titanate had the best combination of parameters so Columbia began development of the processing techniques required to adapt the crystal ion slicing (CIS) to barium titanate and to demonstrate low-loss optical waveguides in this material. Columbia subsequently did adapt the CIS process to barium titanate. Further they were able to demonstrate low loss optical waveguides in this material by fabricating a complete modulator.

PSI, together with their consultant Anokiwave, developed the electrode design for barium titanate as well as potassium niobate, which was identified as a material with properties in between lithium niobate and barium titanate. Since this design is heavily dependent on the material properties, PSI developed a plan to measure the properties of these materials. Actual measurements were subsequently made on potassium niobate, however we did not carry through on measuring barium titanate because it was decided that this material had a fatal flaw: too low a Curie temperature for practical use.

#### ***Fabrication of channel waveguides in $\text{BaTiO}_3$***

Columbia investigated various methods for making optical waveguides in  $\text{BaTiO}_3$ , such as thin film growth, wet etching, mechanical stress, and ion implantation. Conventional processes, such as ion in-diffusion, are not available for this material. Columbia's approach was a combination of ion implantation and wet etching of the top surface.

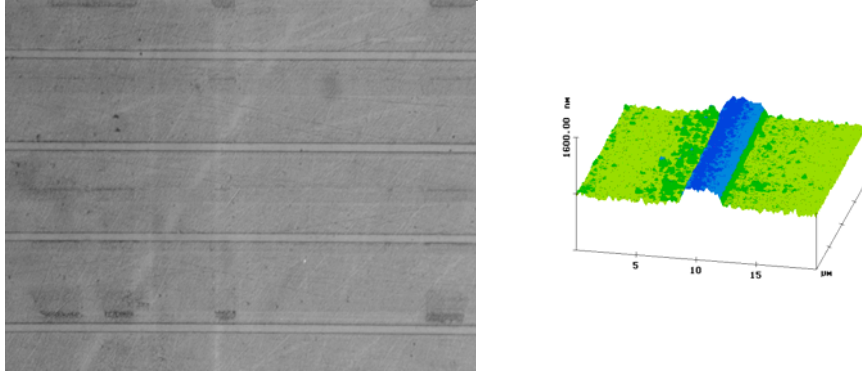


**Figure 56.** Waveguides formed on a surface by wet etching. The waveguide structure is shown at right, and a photograph of a top-view AFM image of the structure is shown at left.

For the ion implantation step, He ions were implanted at energies ranging from 0.6–1 MeV. Ion-implanted  $\text{BaTiO}_3$  samples were measured by prism coupling to obtain the effective index of the resulting waveguide. Then, the refractive index profile due to the implantation was numerically computed. Using these data, a 3-D channel waveguide was designed using a beam-propagation-method simulation package (BeamProp). Next, the channel waveguides were prepared by wet etching of the top surface in diluted HF. Thus the wet etching provided lateral confinement while the ion implantation formed the bottom boundary. These channel waveguides were tested and showed guiding of the optical input from a fiber. Minimization of optical loss due to leakage into higher-index bulk region was calculated. It was found that two implantation steps at two different energies are needed so as to form a thicker vertical boundary for guided modes. Figure 56 shows the waveguides Columbia formed on a  $\text{BaTiO}_3$  substrate in this manner.

Columbia successfully fabricated a test structure for the  $\text{BaTiO}_3$  polarization modulator in lithium niobate. The bidirectional beam propagation method (Bi-BPM) was shown to be useful for simulating our  $\text{BaTiO}_3$  polarization modulator. Binary superimposed gratings for use with multiple wavelength gratings were also tested by Bi-BPM and compared with theory.

### ***Formation of electrodes on $\text{BaTiO}_3$***

Because of the relatively small difference in TE and TM mode indexes in  $\text{BaTiO}_3$ , the modulator electrodes must form a periodic grating structure with a periodicity of  $\sim 50 \mu\text{m}$ . This pattern can be written easily by laser direct writing, which has the advantage of rapidly implementing changes in the grating design. One of the difficulties of the device fabrication process is accurate alignment of the electrode pattern relative to the waveguide. Optimal alignment is achieved by doubly exposing a pre-fabricated waveguide, covering the entire waveguide with a mask aligner, and using laser direct writing to implement the grating structure. Deposition of a Ti (or Cr) layer for adhesion promotion and a capping gold layer by sputtering, and the subsequent lift-off process, resulted in the electrode shown in Figure 57. Flexible patterning using laser direct writing also allows us to study a more complex electrode design for the electrodes, such as Binary Superimposed Grating (BSG) for multi-wavelength devices, and to optimize the

performance of a detailed design, including, for example, apodization for sideband suppression and segmented electrodes for faster modulation.

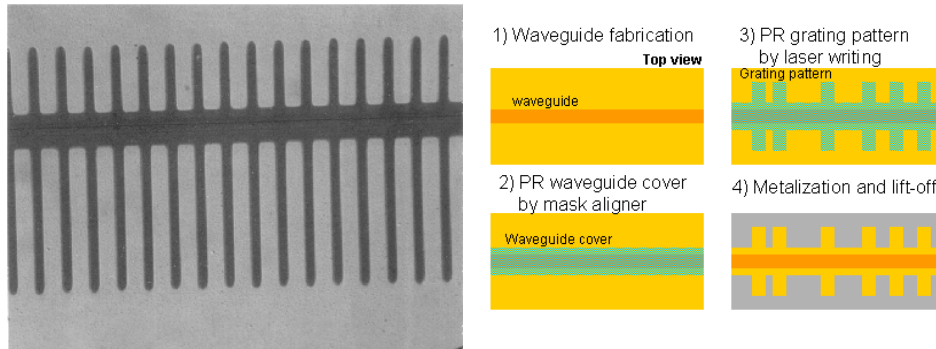


**Figure 57.** Grating electrodes on  $\text{LiNbO}_3$  for the fabrication process test. In photograph at left, a titanium in-diffused waveguide is aligned in a gap (horizontal region) between electrodes (lighter comb-shaped lighter regions). The schematic diagram shows how this four-step electrode alignment procedure was successfully used in the past to fabricate a chirped grating structure in  $\text{LiNbO}_3$ .

### ***Measurement of the microwave properties of $\text{BaTiO}_3$***

Temperature places severe constraints on  $\text{BaTiO}_3$  material. As the temperature decreases to 9C, it undergoes a non-reversible crystalline change that produces twinning. As a result, the sample must be kept at elevated temperature during shipping, storage, processing, and use. In addition, its Curie temperature is 120C, and its microwave and dielectric properties are therefore highly temperature dependent, even at room temperature.

Measurements were made of the dielectric properties of barium titanate at 3 GHz, in conjunction with Prof. Mark Reeves at George Washington University. The data for this experiment essentially was consistent with data published in the 1960's by Russian researchers.

### **Thin lithium niobate material process development for Mach-Zehnder modulator**

The breakthrough advantage the RFLICs program was attempting to apply was the thin film lithium niobate that Columbia developed. Using a technique they refer to as crystal ion slicing (CIS), for the first time Columbia produced single crystal lithium niobate that is more than an order of magnitude thinner than the thinnest conventional lithium niobate, as shown in Figure 58.

Clearly in a standard MZ modulator, the difference between the optical phases at the output of the two arms of the interferometer is what is being changed as the voltage across the electrodes is changed. Columbia has analyzed whether CIS technology might be exploited to improve MZ performance, and have projected that a MZ modulator fabricated in 3- $\mu\text{m}$  x-cut  $\text{LiNbO}_3$  with a ridge electrode structure having a cross-section shown in Figure 58 can have a  $V_\pi \times L$  product of

7.0 V cm. To our knowledge, the smallest  $V_\pi \times L$  product reported so far for a MZ modulator in thick ( $> 100 \mu\text{m}$ )  $\text{LiNbO}_3$  has been about 9.0 V cm. Moreover, the design shown in Figure 58 is projected to have a microwave index, characteristic impedance, and electrode attenuation [2.15, 45  $\Omega$ , and 0.3 dB/(cm GHz<sup>1/2</sup>), respectively] that is likely to yield a higher bandwidth per unit  $V_\pi$  than has been reported for MZs in thick  $\text{LiNbO}_3$ .

Columbia was able to obtain lift-off of films from both z- and x-cut  $\text{LiNbO}_3$ . Work on the x-cut methods achieved the best optical properties. Columbia also successfully deposited and patterned metal electrodes onto the samples prior to lift-off, using an encapsulation procedure. Columbia was able to improve upon the annealing conditions prior to and after lift-off; these improvements have allowed for larger film size and better film quality.



**Figure 58.** Comparison of the thinnest conventional lithium niobate and the new thin lithium niobate developed by Columbia.

### Materials investigation ended

From a material point of view we had three candidate modulator materials, as listed in Table 3. The barium titanate would permit demonstration of the low  $V_\pi$  goal. However we do not see way to design electrodes to meet the bandwidth goal. Further the low Curie temperature of barium titanate would significantly limit its application. The potassium niobate has a higher Curie temperature but not as high an electro-optic coefficient. Consequently we could demonstrate a modulator that meets the RFLICs bandwidth goal, but not the  $V_\pi$  goal. Since Columbia has not adapted the CIS process to this material, nor has it developed a low loss waveguide process, it would take an estimated 18 months to bring this material on line. These

tradeoffs were reviewed by the sponsor. The sponsor decided to discontinue the external modulation materials investigation for the remainder of the RFLICs program.

**Table 3:** Comparison of modulator materials.

	BaTiO <sub>3</sub>	LiNbO <sub>3</sub>
Principal Advantage	Lowest $V\pi L$ at reasonable BW (e.g. 10 GHz) or lowest $V\pi$ at low frequency (e.g. <1 GHz)	~30% lower $V\pi$ at wide bandwidth
Main Questions	RF electrode design	None

### 3.3 *External Modulation Techniques*

#### **Vertical Fabry-Perot modulator**

One way of converting phase modulated light to intensity modulated light is with a Fabry-Perot (FP) interferometer. In an FP modulator an applied voltage produces an electric field parallel to the direction of light propagation. This “vertical FP” configuration has an improved electrical-optical field overlap relative to MZ modulators. Additionally a very short vertical cavity will yield a large 3-dB bandwidth without the need for a traveling-wave electrode and the associated velocity matching challenges.

PSI investigated a unique vertical FP modulator design shown in Figure 59. PSI chose to re-investigate the FP modulator because there have been many advances in linearization, wavelength stabilization, and fabrication of high-reflectivity mirrors since the FP was first proposed for analog links<sup>14</sup>. Vertical FP modulators with bandwidths as high as 37 GHz<sup>15</sup> have been realized in semiconductors; however the optical attenuation has limited the effective  $V\pi$  to ~3 V. The key to implementing this approach is micron-thin LiNbO<sub>3</sub> or other electro-optic material. In a FP modulator an applied voltage produces an electric field parallel to the direction of light propagation.



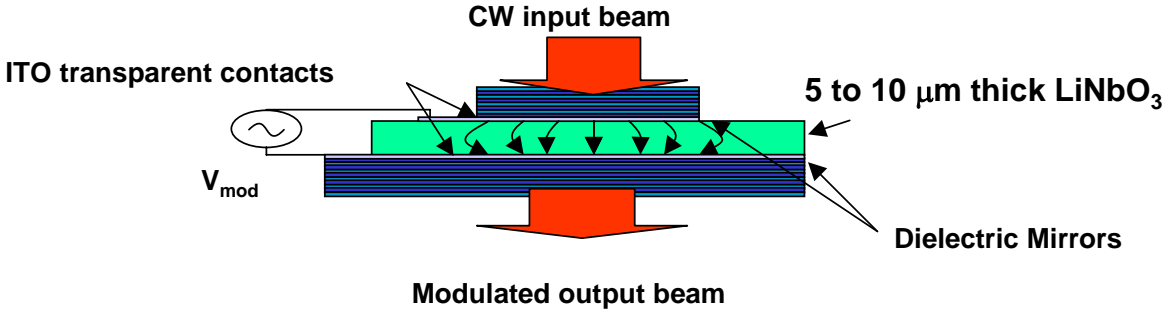


**Figure 59.** Cross section sketch of the vertical Fabry-Perot modulator.

### Gain/bandwidth tradeoff

Two of the key modulator performance parameters that the RFLICs program is attempting to improve are the  $V_\pi$  (or its equivalent) and the bandwidth. As is often the case, the techniques for optimization of these two parameters are not independent. Thus it is imperative to understand the design tradeoffs between these two parameters, which are independent of the fabrication or implementation tradeoffs that will subsequently apply.

Across the RFLICs program there are several teams working on various resonant-based advanced modulators, among them the vertical FP that the Photonic Systems team is working on. Thus we began by setting up the analytical framework to define the  $V_\pi$ /bandwidth design tradeoffs for the vertical FP. Once we completed this analysis we realized that these analytical tools were applicable to other types of modulators, prime among them the microcavity-resonator-based designs being pursued by several of the other RFLICs teams.

Recall that the vertical FP, shown in a cross-sectional sketch in **Figure 59**, is a new modulator configuration proposed by Photonic Systems and Columbia that takes advantage of the Crystal Ion Slicing (CIS) technology developed at Columbia for producing thin ( $\sim 10 \mu\text{m}$ ) lithium niobate material.

The transfer function of a FP modulator has been shown in more than one instance<sup>16,17</sup> to be:

**Equation 1** 
$$I \equiv \frac{I_{out}}{I_{in}} = \frac{(1 - \sqrt{R_1 R_2} e^{-2\alpha L})^2}{(1 - \sqrt{R_1 R_2} e^{-2\alpha L})^2 + 4\sqrt{R_1 R_2} e^{-2\alpha L} \sin^2\left(\frac{2\pi n L}{\lambda}\right)},$$

where  $I$  and  $\lambda$  are the optical intensity and wavelength, respectively,  $R_1$  and  $R_2$  are the input and output mirror reflectivities, respectively,  $\alpha$  is the optical attenuation per unit length in the FP cavity, and  $n$  and  $L$  are the index of refraction and length of the cavity, respectively. What we wish to illustrate can be seen more clearly if we simplify Equation 1 by defining  $R_1=R_2=R$  and assuming that attenuation in the cavity is negligible (i.e.,  $\alpha \sim 0$ ). Equation 1 can then be rewritten as follows:

**Equation 2** 
$$I \equiv \frac{I_{out}}{I_{in}} = \frac{(1 - R)^2}{(1 - R)^2 + 4R \sin^2\left(\phi_{bias} - \frac{\pi n^3 r \Gamma L}{\lambda g} v_m\right)}.$$

In Equation 2 we have also shown how the optical phase shift incurred in the FP cavity, which is the argument of the  $\sin^2$  function, is determined by a bias point and modulated by the signal voltage  $v_m$ . In Equation 2,  $r$  is magnitude of the cavity material's electro-optic tensor,  $\Gamma$  is the electrical-optical field overlap integral, and  $g$  is the gap distance between the electrodes traversed by the electric field.

At some bias points, the transfer function of a FP modulator can be much steeper than the transfer function of a MZ at its quadrature bias. This is because the optical phase shift required to shift a FP between its maximum and minimum output intensity is much less than the  $\pi$  phase shift required to switch a MZ from its maximum to its minimum. (How much less depends on the mirror reflectivities.) Therefore to compare a FP to a MZ we calculate  $V_{\pi,FP}$  which is the  $V_\pi$  that a MZ would have to exhibit to result in the same transfer function slope as the FP has at its maximum-slope bias point. Like a MZ, the FP modulator's transfer function has a maximum slope when  $I=0.5$ . Therefore  $V_{\pi,FP}$  is calculated as follows:

**Equation 3** 
$$V_{\pi,FP} \equiv \frac{\pi}{2} \frac{1}{\left| \frac{\partial I}{\partial v} \right|_{I=0.5, v=0}} = \frac{1-R}{\sqrt{R}} \frac{\lambda g}{2 n^3 r \Gamma L} = \frac{1-R}{\sqrt{R}} V_{\pi,MZ}.$$

The bandwidth of the FP modulator can be calculated by assuming it to be a linear first-order system like an RC circuit. For small-signal modulation in a cavity with large mirror reflectivities this is a good approximation. In such a system the electrical 3-dB bandwidth is the frequency at which the output power is  $1/\sqrt{2}$  of what it is at DC. (Using this factor of  $1/\sqrt{2}$  yields the *electrical* 3 dB bandwidth, whereas using a factor of  $1/2$  would give the *optical* 3 dB bandwidth.) Therefore, at the electrical 3 dB roll-off frequency  $f_{3dB_e}$ ,

**Equation 4** 
$$\frac{1}{(2\pi f_{3dBc})^2 + \frac{1}{\tau_f^2}} = \frac{1}{\sqrt{2} \frac{1}{\tau_f^2}},$$

where  $\tau_f$  is the 1/e optical field decay time in the cavity, which is

**Equation 5** 
$$\tau_f = -\frac{2nL}{c \ln(R)} \approx \frac{2nL}{c(1-R)}.$$

Therefore,

**Equation 6** 
$$f_{3dBc} \approx \frac{\sqrt{\sqrt{2}-1}}{4\pi} \frac{c}{nL} (1-R).$$

It is important to point out that very small  $V_\pi$  can be achieved using the vertical FP modulator in a narrow bandwidth around a high center frequency. For instance, a  $V_{\pi,FP}$  of 1 V (corresponding to a link gain of about 0 dB for a laser power of 10 mW) can be achieved in a 100 MHz bandwidth. This 100 MHz-wide band can be centered at any RF frequency we choose; the maximum center frequency would be limited only by the bandwidth of the photodetector and dispersion in the fiber.

Note that the ratio of  $f_{3dBc}/V_\pi$  is a good figure of merit for a modulator, and at these large values of R that give low  $V_\pi$  this ratio is relatively independent of R:

**Equation 7** 
$$\frac{f_{3dBc}}{V_{\pi,FP}} \approx \frac{\sqrt{\sqrt{2}-1}}{2\pi} \frac{n^3 r \Gamma c}{\lambda g}.$$

The equations above, Equation 1– Equation 7, apply to all FP modulators. Equation 7 implies that achieving a significantly larger  $f_{3dBc}/V_\pi$  ratio in a FP modulator will require a material with a much greater electro-optic tensor  $r$ .

A simple FP modulator of Figure 60 and a resonant interferometric modulator of Figure 61 that can be fabricated in lithium niobate have characteristics that are exactly equivalent to those of a FP modulator. In the FP modulator of a mirror (with reflectivity  $R_1$ ) determines the percentage of light that is coupled from the input port into the resonant cavity and from the cavity into input port 1, a second mirror (with reflectivity  $R_2$ ) determines the percentage of light that is coupled from the cavity into output port 2, and the round-trip optical phase shift incurred in the cavity is  $4\pi nL/\lambda$ . In the equivalent resonant interferometer structure a directional coupler (with coupling coefficient  $k_1$ ) determines the percentage of light that is coupled from the input port into the resonant cavity and from the cavity into output port 1, a second coupler (with coupling

coefficient  $k_2$ ) determines the percentage of light coupled from the cavity into output port 2, and the round-trip optical phase shift incurred in the cavity is  $2\pi nC/\lambda$ , where  $C$  is the round-trip length of the cavity [we chose  $C$  for Circumference]. I. Gheorma and R. Osgood of Columbia University<sup>18</sup> showed that Equations (1)-(7) given for a FP modulator apply for the case of the resonant modulator as well if we make the following substitutions:

**Equation 8**  $R = \sqrt{R_1 R_2} \Rightarrow 1 - |k_1 k_2|$   
and

**Equation 9**  $L \Rightarrow \frac{C}{2}.$

Therefore, for the resonant interferometric modulator shown in the following equations apply:

**Equation 10** 
$$V_{\pi,eq} \equiv \frac{\pi}{2} \frac{1}{\left| \frac{\partial I}{\partial v} \right|_{I=0.5, v=0}} = \frac{|k|^2}{\sqrt{1-|k|^2}} \frac{\lambda g}{n^3 r \Gamma C} = \frac{|k|^2}{\sqrt{1-|k|^2}} \frac{2}{C} V_{\pi,MZ},$$

**Equation 11** 
$$f_{3dBc} \approx \frac{\sqrt{\sqrt{2}-1}}{2\pi} \frac{c}{nC} |k|^2,$$

and

**Equation 12** 
$$\frac{f_{3dBc}}{V_{\pi,eq}} \approx \frac{\sqrt{\sqrt{2}-1}}{2\pi} \frac{n^3 r \Gamma c}{\lambda g},$$

where for simplicity we have assumed  $k=k_1=k_2$  and  $|k|^2 \ll 1$ . Note that for  $|k|^2 \ll 1$  the  $f_{3dBc}/V_{\pi}$  ratio is independent of  $C$  and  $k$ , just as the FP modulator's  $f_{3dBc}/V_{\pi}$  ratio was shown to be independent of  $L$  and  $R$ , and is therefore limited to a value on the order of 0.1 GHz/V (assuming fabrication in LiNbO<sub>3</sub> with  $g \sim 15 \mu\text{m}$ ,  $n \sim 2.2$ ,  $r \sim 30 \text{ pm/V}$ ,  $\Gamma \sim 0.5$ , and operation at  $\lambda \sim 1550 \text{ nm}$ ), which is the same value we calculated for the vertical FP above.

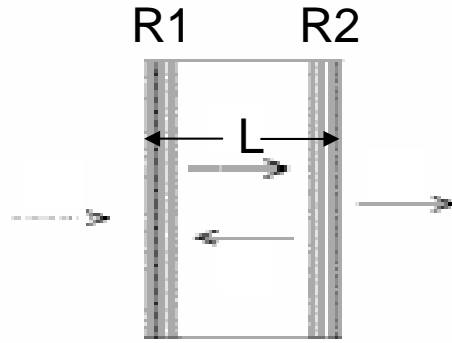


**Figure 60.** Representation of a Fabry-Perot Cavity of length  $L$  with reflectivities  $R1$  and  $R2$

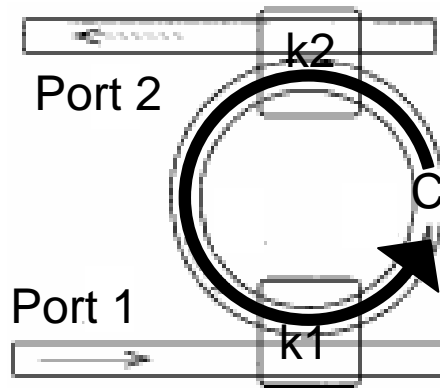


**Figure 61.** Representation of a ring resonator of circumference  $C$  and reflectivities  $k1$  and  $k2$

The table below gives representative values for this figure of merit for the conventional MZ as well as the proposed Fabry Perot. We see that a Fabry Perot has about  $\frac{1}{4}$  the performance of a MZ whereas a disk-resonator-based modulator is slightly better than a MZ.

Modulator Type	Gap Width ( $\mu\text{m}$ )	$f_{3\text{ dB}}/V_{\pi}$ (GHz/V)
Mach Zehnder	15	0.5
Fabry Perot	15	0.13
Resonant Disk	3	0.66

The conclusion at this point is that none of the resonant-based modulator designs will meet the RFLICs program goals. Thus we suspended work on the vertical FP modulator. We instead focused our efforts under this task on attempting to find a modulator configuration that had the required sensitivity and bandwidth.

### Broad-bandwidth Resonant (BBR) Modulator

A unique device architecture, shown in

**Figure 62** and known as the broad-bandwidth resonant (BBR) modulator, has been proposed that combines resonant and non-resonant interferometric modulation techniques. The transfer function of this modulator is shown in

**Figure 63** and compared to that of an MZ. Using a system transfer matrix approach, it has been calculated that this device can provide 20x greater sensitivity (transmission vs. applied voltage) than a completely non-resonant interferometric modulator (such as an MZ). For such performance, it is necessary that the resonance condition be satisfied for the chosen input light frequency, and that the loss within the ring resonator and the coupling coefficient satisfied by the “critical coupling” relation.

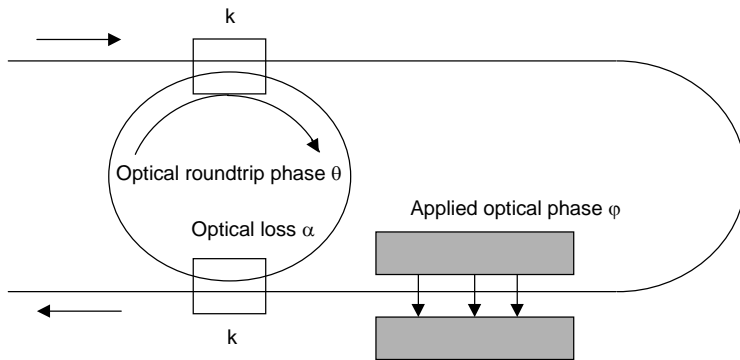


**Figure 62.** Novel modulator that combines a non-resonant phase modulator with a resonant loop.

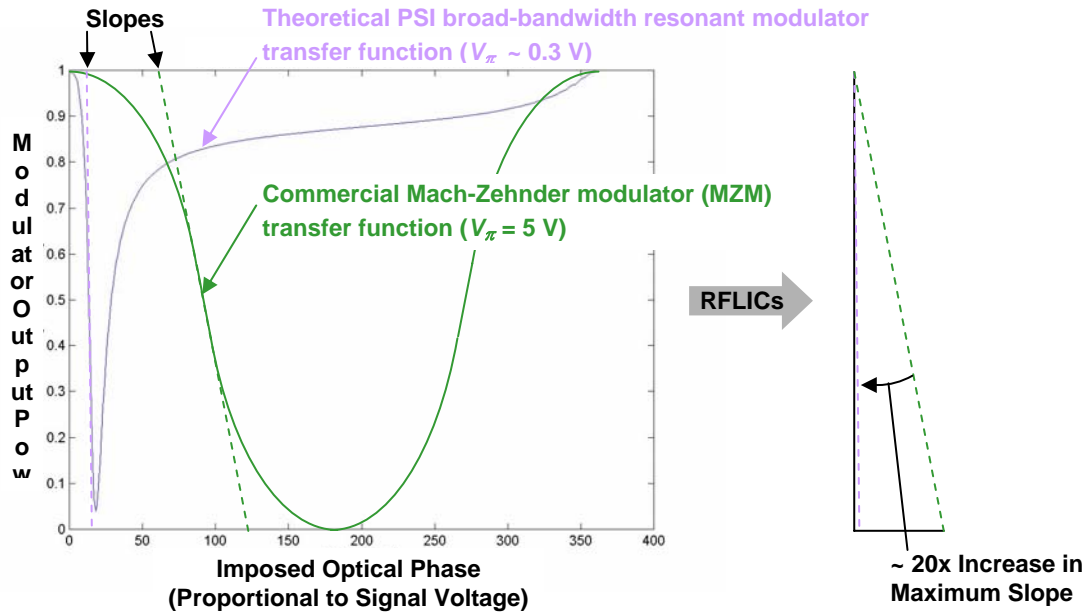


**Figure 63.** Transfer functions of a Mach-Zehnder and broad bandwidth resonant modulators.

After reviewing all our options, PSI followed the following progression of BBRs to best demonstrate the improvement of gain in an analog link with the BBR modulator as compared to a standard MZ.

1. BBR All fiber breadboard (first experimental results)
2. BBR hybrid —  $\mu$ -ring, and LiNbO<sub>3</sub> Phase Modulator (second experimental results)
3. BBR hybrid —  $\mu$ -ring, EDWA and LiNbO<sub>3</sub> Phase Modulator (near-term risk reduction)
4. BBR in LiNbO<sub>3</sub> (near-term risk reduction)
5. BBR monolithic or integrated hybrid (long term solution, higher-risk, high-payoff implementation)

### ***Theoretical analysis of BBR***

We investigated the transfer function of the broadband resonator (BBR) as a function of optical frequency as shown in Figure 64 and Figure 65. The transfer function makes a significant change over just 5 GHz. Even if one assumes very small signal levels so that one is only sensitive to the slope right at the bias point, the factor-of-three slope change at bias points around  $\phi_B = 140^\circ$  gives a 10dB drop in power response (gain and noise figure) by 20 GHz even if the modulator electrode response is flat.

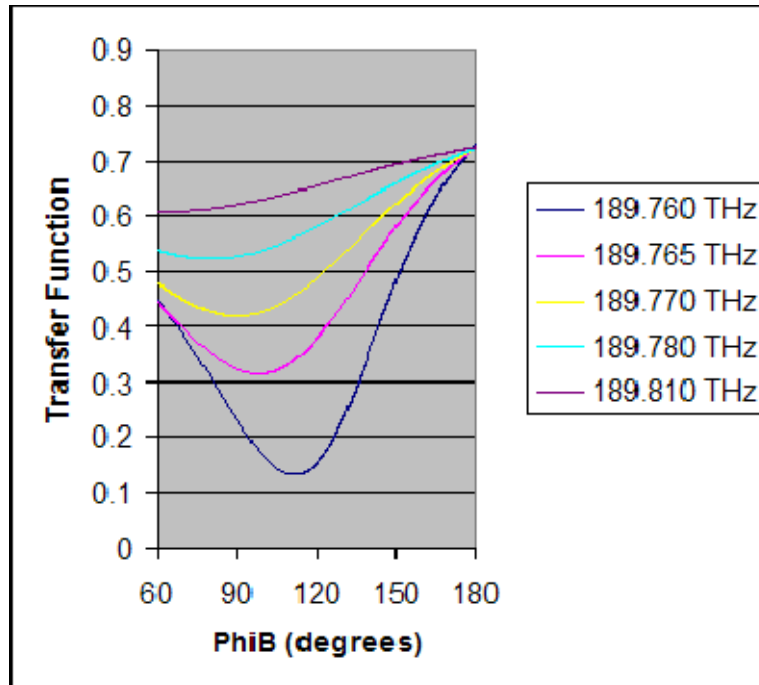


**Figure 64.** Transfer function of BBR as a function of optical frequency.

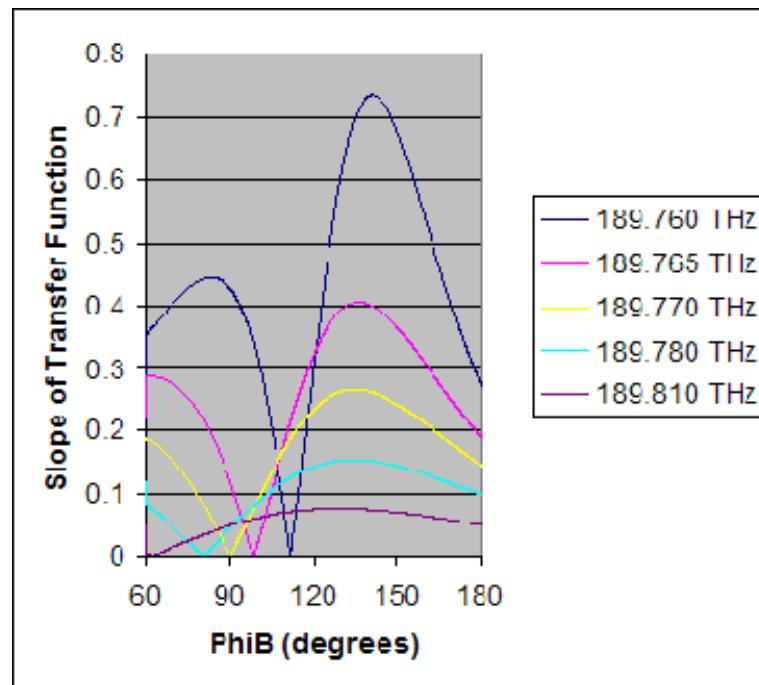


**Figure 65.** Slope of transfer function of BBR as a function of optical frequency.



PSI performed a time domain analysis of the transfer function of resonant interferometric modulators, and calculated the Fourier transform of the time-domain response to determine their RF frequency responses. There are some fundamental similarities between the ring resonator-based modulator and a Fabry-Perot modulator. One similarity is that for identical round-trip resonator (or cavity) travel time  $\tau$ , the ring resonator and the Fabry-Perot have the same resonance spectrum, as shown in Figure 66. In other words, the length of the cavity,  $L$ , affects the free spectral range (FSR) of the novel ring resonator in the same manner as it does for that of the Fabry-Perot.

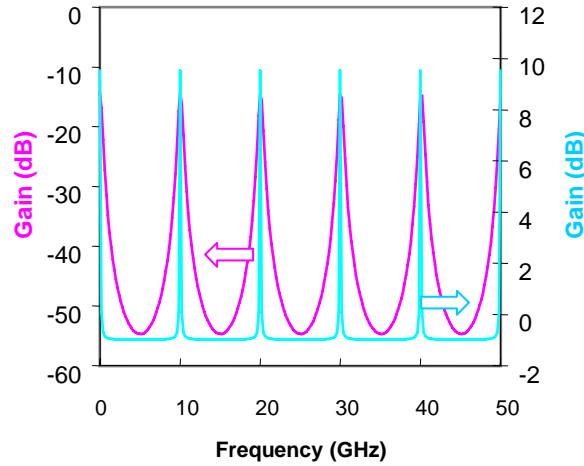


**Figure 66.** Results of MATLAB time-domain analysis of Gain for two links with different resonant modulator types having the same resonator roundtrip time  $\tau = 100$  psec. Left axis: link Gain for Fabry-Perot modulator with mirror reflectivity  $R=0.9$  (magenta curve); Right axis: link gain for novel ring resonator-based modulator with  $k=0.5$ .

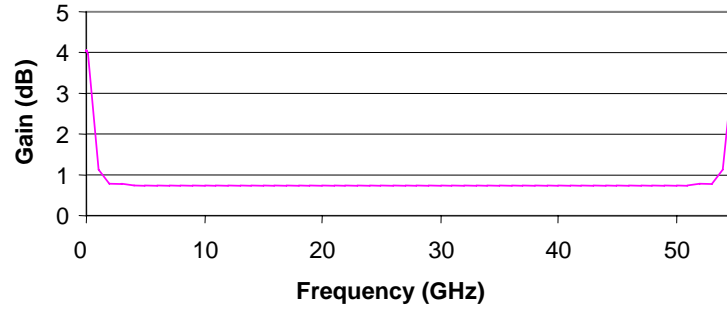
There are important ways that the novel ring resonator modulator differs fundamentally from a Fabry-Perot modulator. For given values of  $k$  (the coupling factor to and from the ring resonator) and  $\alpha$  (the insertion loss in the resonant ring), there are specific values of  $\theta$  (the round-trip phase incurred in the ring) and  $\phi$  (the applied optical phase shift in the outer arm) that result in optimal gain. This is one more degree of freedom than a Fabry-Perot offers; in the Fabry-Perot there is simply an optimum value of  $\phi$  for given values of  $R$ , but the gain is always optimum for  $\alpha = 1$  (no attenuation). We believe this fundamental difference arises because, whereas in a Fabry-Perot the phase modulation is imposed inside the resonant cavity, in the modulator shown in

Figure 62 the phase modulator arm is external to the resonator.

We have determined a means for leveraging this extra degree of freedom afforded by the novel ring resonator-based modulator. We have found that for a given value of  $\tau$  (or equivalently, the electrode length  $L$ ), which alone determines the free spectral range, there are several  $k-\theta-\alpha$  combinations of that yields a link gain of  $\sim 0$  dB (which corresponds to  $V_{\pi,eq} \sim 0.3$  V) at some

bias point  $\phi$ . For a given  $k$  value, the predominant effect of varying  $\alpha$  and  $\theta$  is to alter the peak-to-trough ratio in the frequency response plot. For example Figure 12 shows that for a reasonable set of  $k$  and  $L$  values, varying  $\alpha$  and  $\theta$  only slightly affects the link gain (taken as the value in the troughs) while it strongly affects the peak-to-trough ratio. For one set of  $\alpha$  and  $\theta$  values, the response varies by less than 3 dB across the desired 50 GHz band. Therefore, even though the shape of the frequency response is unusual, this design in fact displays a 3-dB bandwidth of greater than 50 GHz.

Because the  $V_{\pi,eq}$  is affected by both  $k$  and  $L$ , but the FSR is not affected by  $k$ , there are necessarily  $k$ - $L$  combinations that yield  $FSR > 50$  GHz with  $V_{\pi,eq} \sim 0.3$  V. The frequency response of one modulator with a set of parameters that yields  $FSR \sim 55$  GHz and  $V_{\pi,eq} \sim 0.3$  V is plotted in Figure 67. Neglecting electrode loss for the time being, this modulator has a flat response from about 1 GHz to about 54 GHz. This may turn out to be a more attractive solution than the one with the “peaky” frequency response shown by the blue curve in Figure 66.



**Figure 67.** Results of MATLAB analysis of the resonant modulator-based link with  $k = 0.4$ ,  $L \sim 2.5$  mm,  $\theta = 1.9723 \pi$ , and  $\alpha = 0.95$  biased at  $\phi = 20.3^\circ$ . The link gain is flat at  $\sim 1$  dB (corresponding to  $V_{\pi,eq} \sim 0.3$  V) over a bandwidth of approximately 1–54 GHz.

### ***BBR - all fiber breadboard***

A schematic of the all fiber BBR breadboard is shown in Figure 68. Here the inner ring resonator of figure L was comprised of 1-meter of fiber. Having an interferometer with very long arms comprised of fiber made this system very unstable. The quickly collected data of Figure 69 shows the gain of the all fiber BBR. The model successfully predicts the average value of link gain between inner loop resonances, locations of the inner and outer loop resonances and finer features of frequency response.

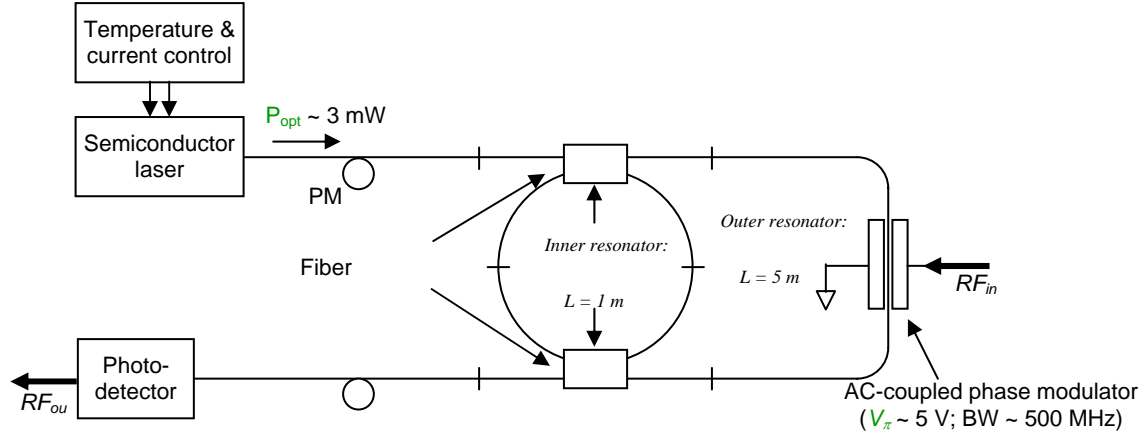


**Figure 68.** All fiber BBR breadboard.

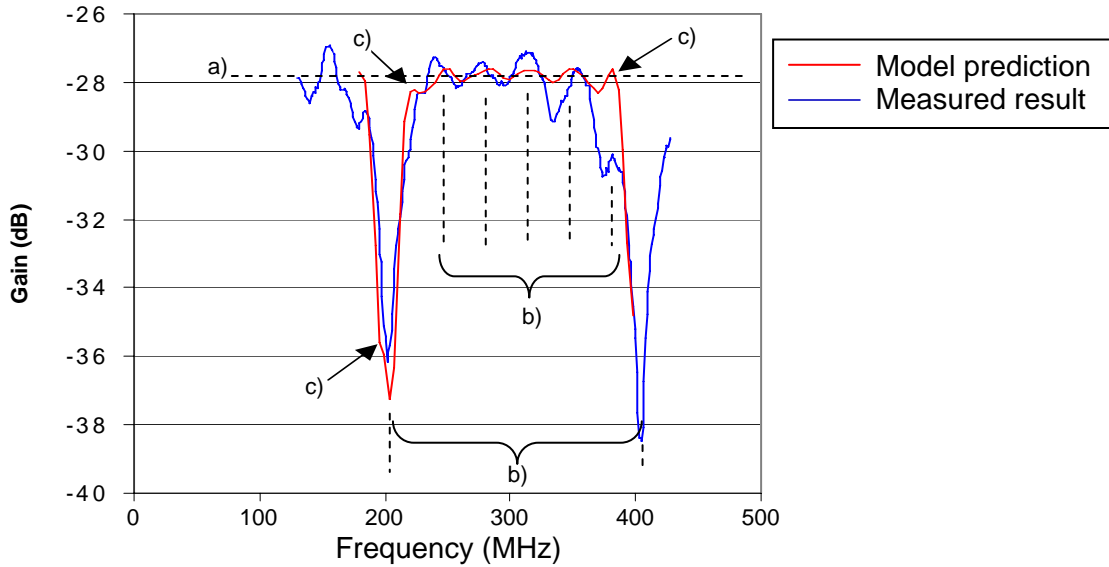


**Figure 69.** Modeled and measured gain of the all fiber BBR breadboard.

There is  $V\pi$  improvement of BBR as compared to Mach-Zehnder. Consider the following question: Is the  $V\pi$  improved by more than three times in this modulator design, relative to the single-pass phase modulator? If it is, then there is still an advantage at high frequency, even with the 3x slope reduction. This looks like the bandwidth versus  $V\pi$  tradeoff, which is expected but maybe is not fatal if the  $V\pi$  goes down faster than the bandwidth. To demonstrate the  $V\pi$  improvement, a phase modulator was tested in both a Mach-Zehnder (MZ) configuration and a BBR configuration. Figure 70 shows an experimental diagram of the BBR. The “x” marks

where the fibers were disconnected to obtain a MZ. Figure 71 contains the data to show that over a given bandwidth, the  $V_\pi$  did improve more than three times for the BBR as compared to the MZ. Due to availability of equipment with the appropriate loss and coupling, we chose to complete this demonstration with fiber couplers with long fiber pigtails and low insertion loss. The resonances seen in Figure 71 are due to the cavities created from the long lengths of fiber of the couplers and phase modulator.

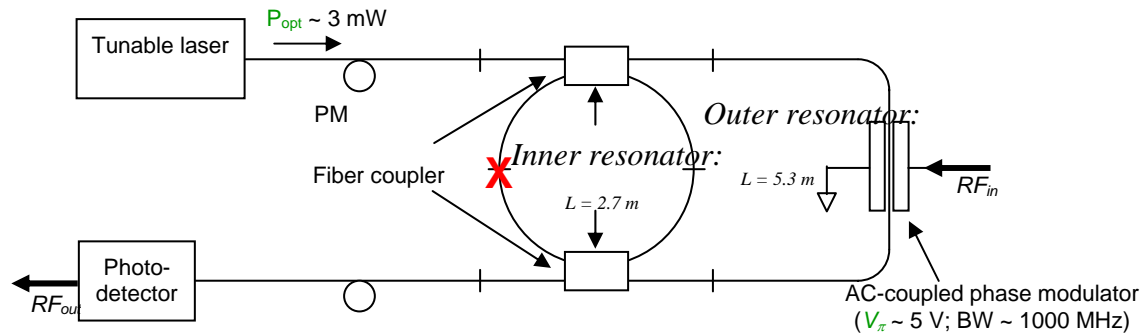


**Figure 70.** Experimental set up of broadband resonant (BBR) modulator. Disconnecting the fibers at the location marked “x” arranges the set up into a Mach-Zehnder configuration.

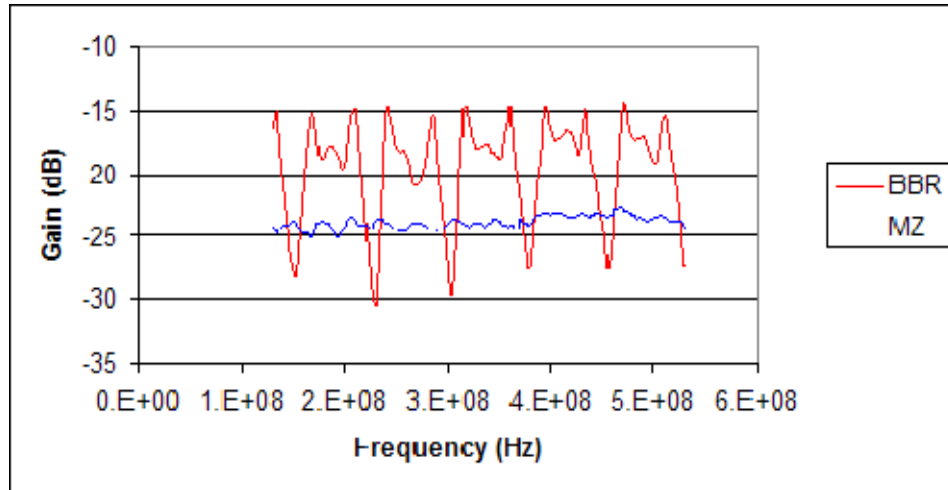


**Figure 71.** The experimental performance comparison of a phase modulator in the BBR vs. a MZ configuration.

### ***BBR hybrid –glass $\mu$ -ring and LiNbO<sub>3</sub> phase modulator***

The hybrid BBR consists of a separate m-ring and LiNbO<sub>3</sub> phase modulator coupled via fiber in a standard configuration as shown in Figure 72. It is non-ideal due to the outer arm length of 6-7 m from the fiber for coupling between devices and has an optional EDWA used to overcome device losses. The first experimental setup without an erbium doped waveguide amplifier (EDWA) of the hybrid BBR is shown in Figure 73. The ring coupling coefficients were not ideal to demonstrate the resonant effect. Therefore, the gain was <-30 dB as shown in Figure 74.

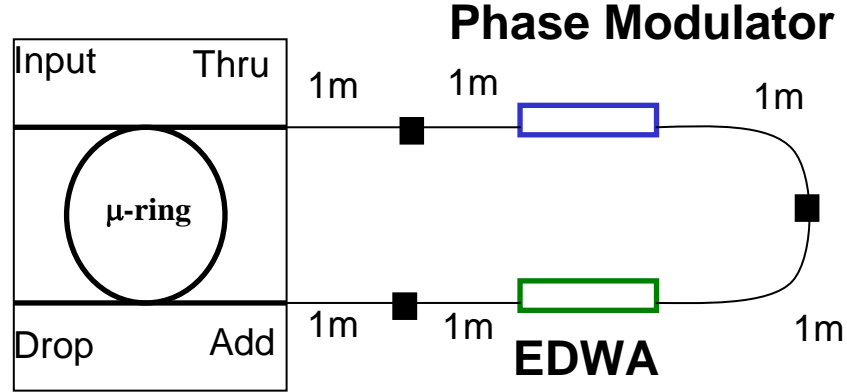


**Figure 72.** Diagram of the hybrid  $\mu$ -ring/LiNbO<sub>3</sub> phase modulator BBR with optional erbium doped waveguide amplifier (EDWA).

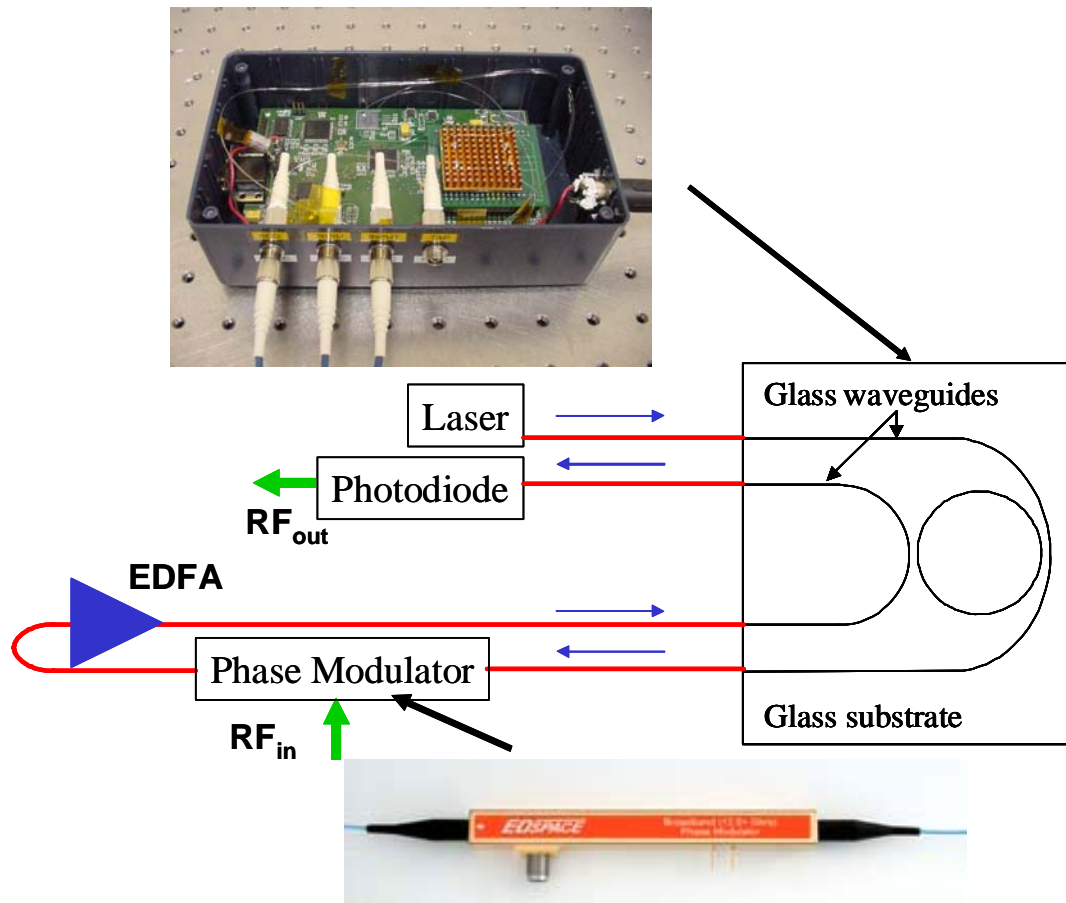


**Figure 73.** Experimental setup of the first hybrid BBR.

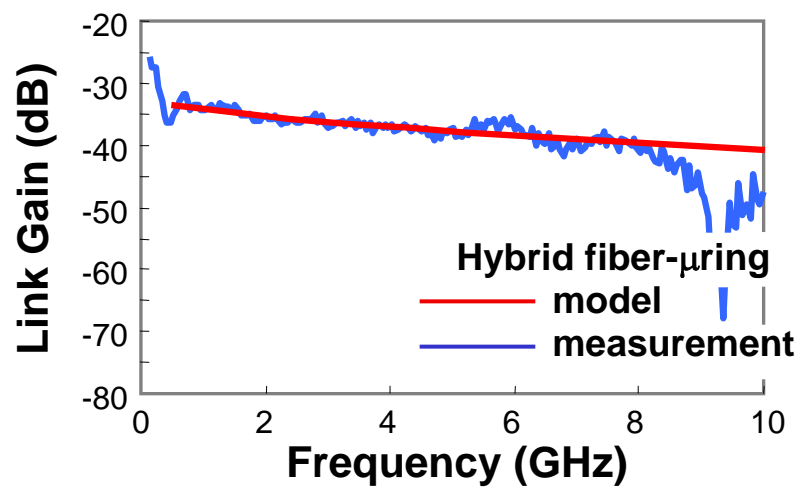


**Figure 74.** Measured and modeled gain of the first hybrid BBR without an EDWA.

In order to make progress towards the goal of PSI requisitioned another  $\mu$ -ring with appropriate coupling coefficients to achieve resonance in the BBR. To extend the frequency response of the modulator, we purchased a new phase modulator with a 3 dB bandwidth of 15 GHz. Figure 75 is a photograph of the experiment for the hybrid fiber/ $\mu$ -ring. The EDWA of this demonstration was only used to overcome the excess insertion loss of the  $\mu$ -ring and phase modulator. BBR was placed in the pink insulating box to minimize the path lengths changes related to temperature variations. The data from the gain measurements as a function of frequency is shown in Figure 76. The equivalent  $V\pi$  without the EDWA was 3.4 V, while the  $V\pi$  improved to 1.8 V with the EDWA.

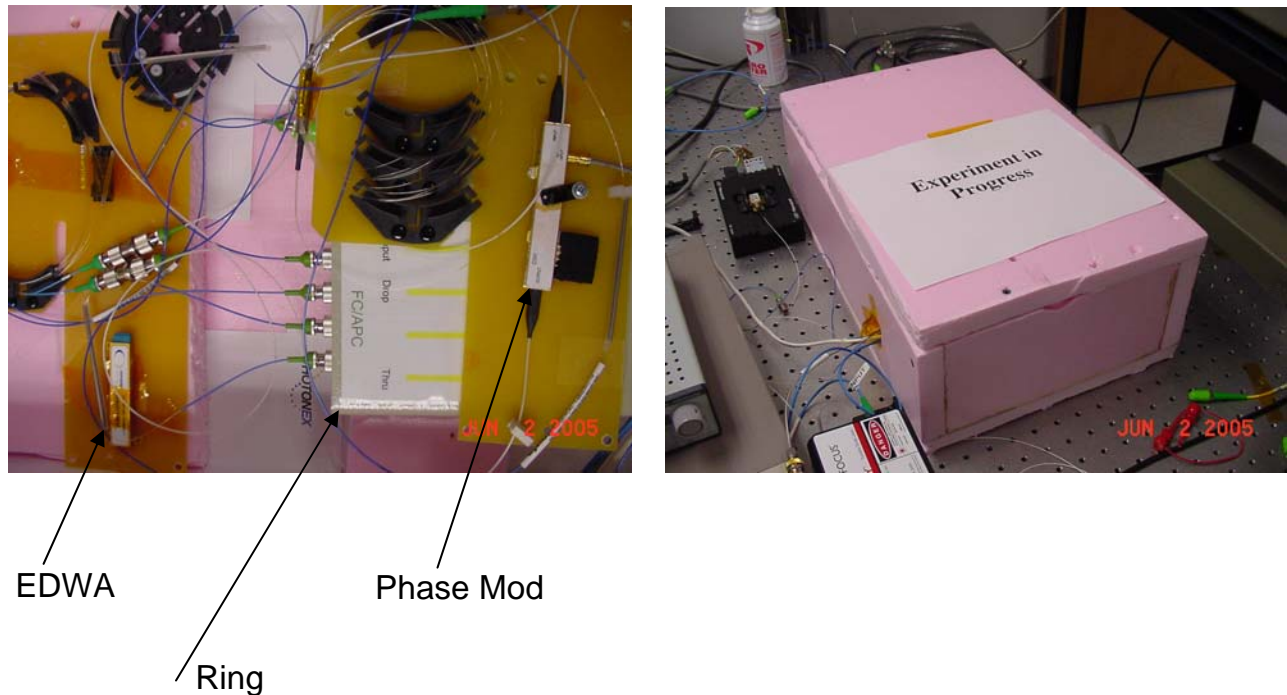


**Figure 75.** Set up of second hybrid BBR.

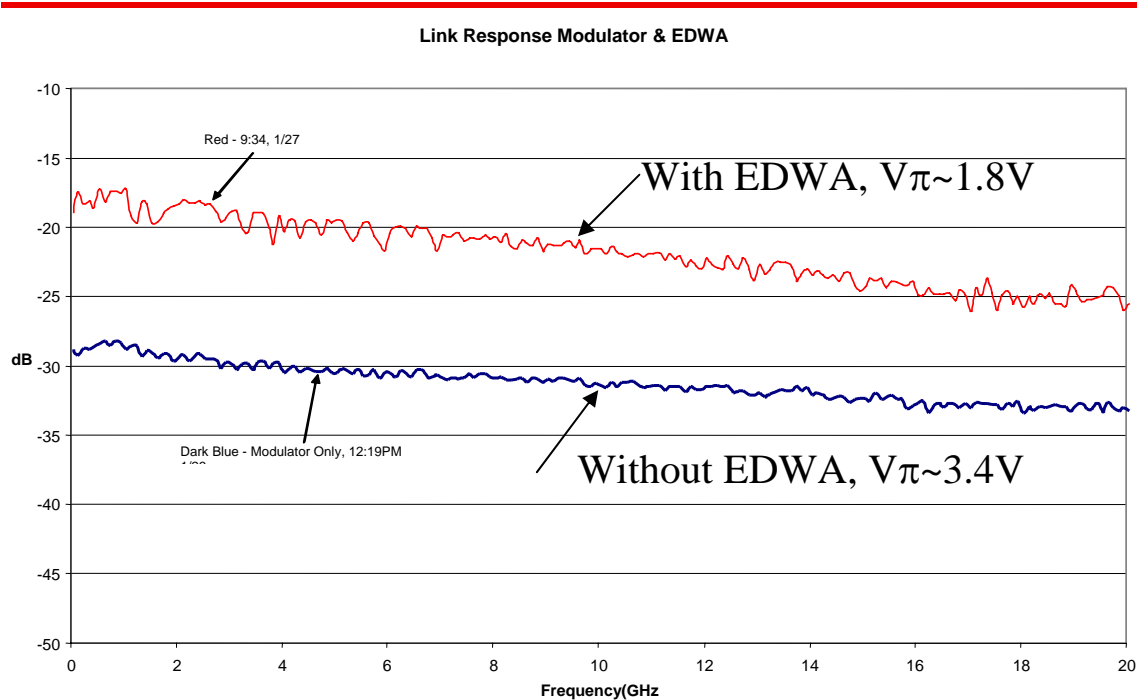
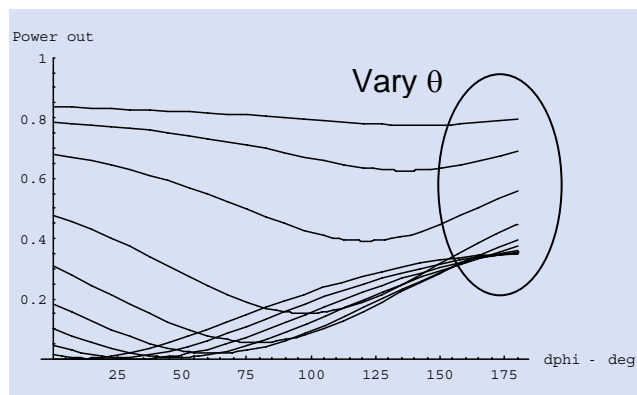


**Figure 76.** Link data with/without amplifier.

Figure 77 and Figure 78 show the modeled transfer functions and RF link gain for two cases of loss in the phase modulator arm of the BBR. The gain of a link is proportional to the slope of the transfer function. As the loss in the phase modulator arm decreases to match the loss in the ring,  $\alpha=1$ , the slope of the transfer function increases. Therefore, the case where  $\alpha=1$  is more desirable since it has a steeper slope. With  $\alpha=1$  and coupling  $t_2=0.95$ , gain equal to zero should be achievable for our BBR.



## Power out

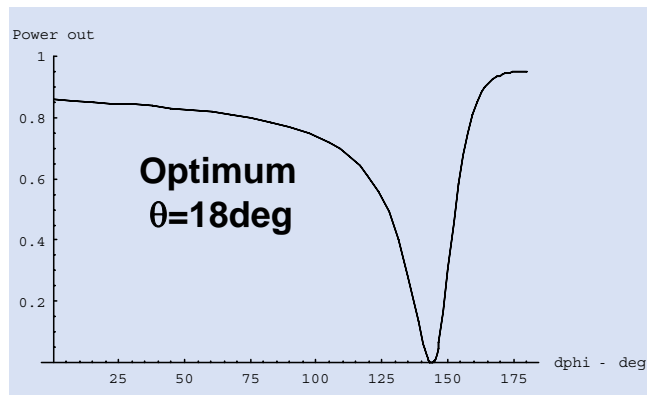


$\Delta\phi$ -deg

no amplifier,  $t_2=0.95$ ,  $\alpha=0.34$

(a)

## Power out



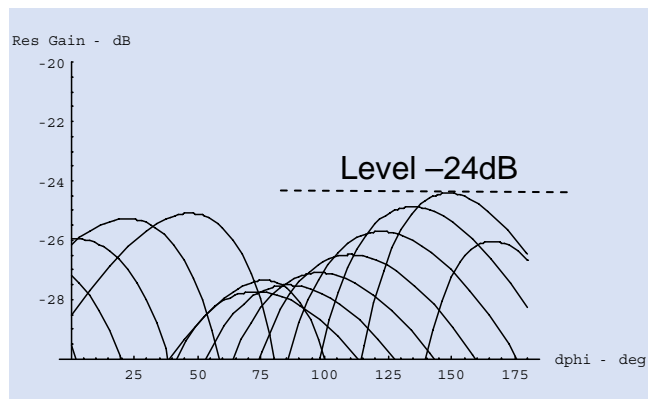
$\Delta\phi$ -deg

amplifier,  $t_2=0.95$ ,  $\alpha=1$

(b)

**Figure 77.** Transfer function of BBR for (a) higher insertion loss of phase modulator arm (b) zero insertion loss of phase modulator arm.

## RF link gain-dB

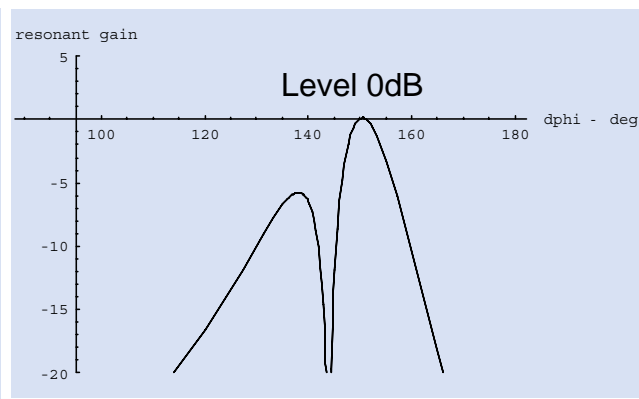


$\Delta\phi$ -deg

no amplifier,  $t_2=0.95$ ,  
 $\alpha=0.34$

(b)

## RF link gain-dB



$\Delta\phi$ -deg

amplifier,  $t_2=0.95$ ,  
 $\alpha=1$

(b)

**Figure 78.** RF link gain of BBR for (a) higher insertion loss of phase modulator arm (b) zero insertion loss of phase modulator arm.

The phase was constantly moving due to thermal effects on fiber and in EDWA, even in insulated chamber. The combination of intensity noise and phase bias drift made it extremely hard to lock bias with bias controller, and thus measure link performance. We were able to measure the transfer function of the modulator as shown in Figure 79. From this transfer function, we measured a  $V\pi \sim 1.8V$ . To minimize the phase drift, the EDWA, ring and phase shifter should be integrated. This would decrease MZ unequal path length, remove long fiber lengths, and allow bias stabilization.

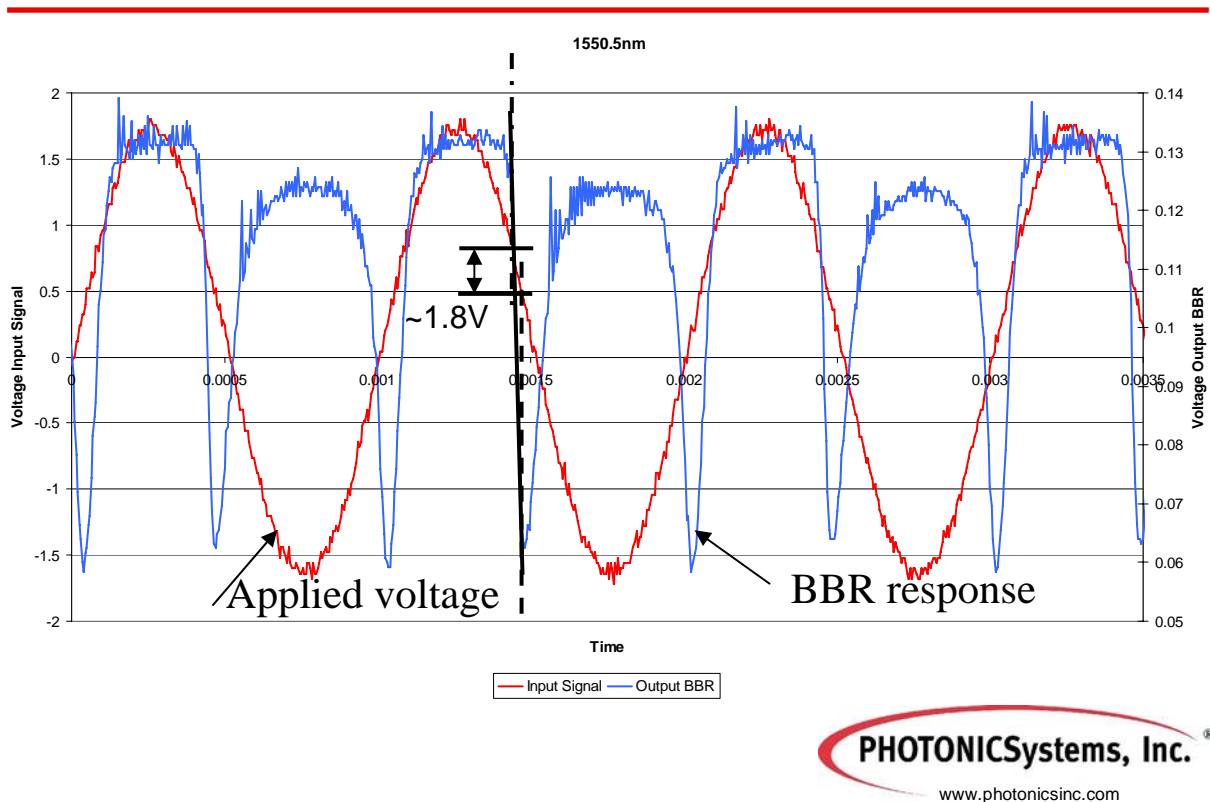


**Figure 79.** Measured transfer function of BBR hybrid with EDWA.

Excess noise made it difficult to make measurements on the hybrid BBR. The noise sources in the BBR include the:

- Amplifier in loop which allows bi-directional lasing in ring, with gain competition between laser and amplifier as shown in Figure 80
- Ring laser which feeds back into source laser, thus requiring high isolation
- Build-up of phase noise in resonant ring and conversion to intensity noise
- Phase and intensity noise amplified in amplifier

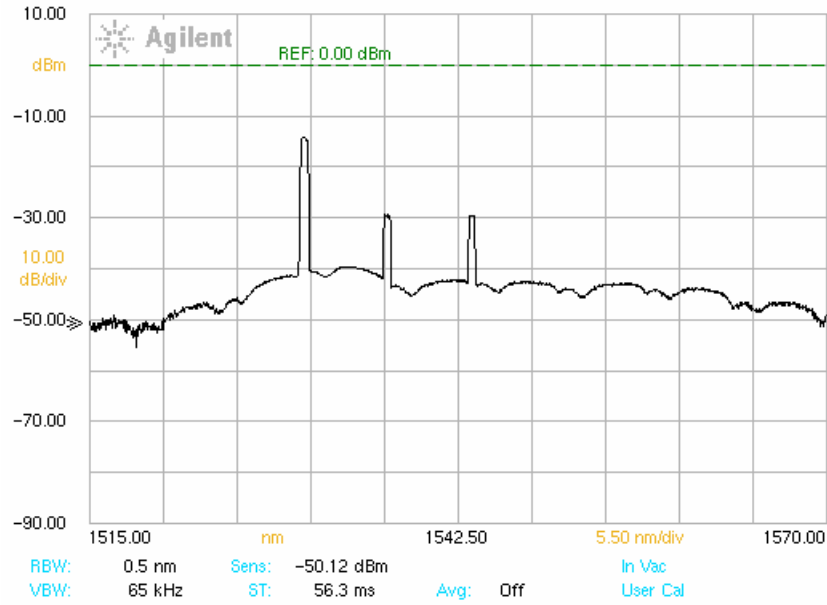


**Figure 80.** Lasing of the EDWA in the BBR configuration with no optical input to the BBR.

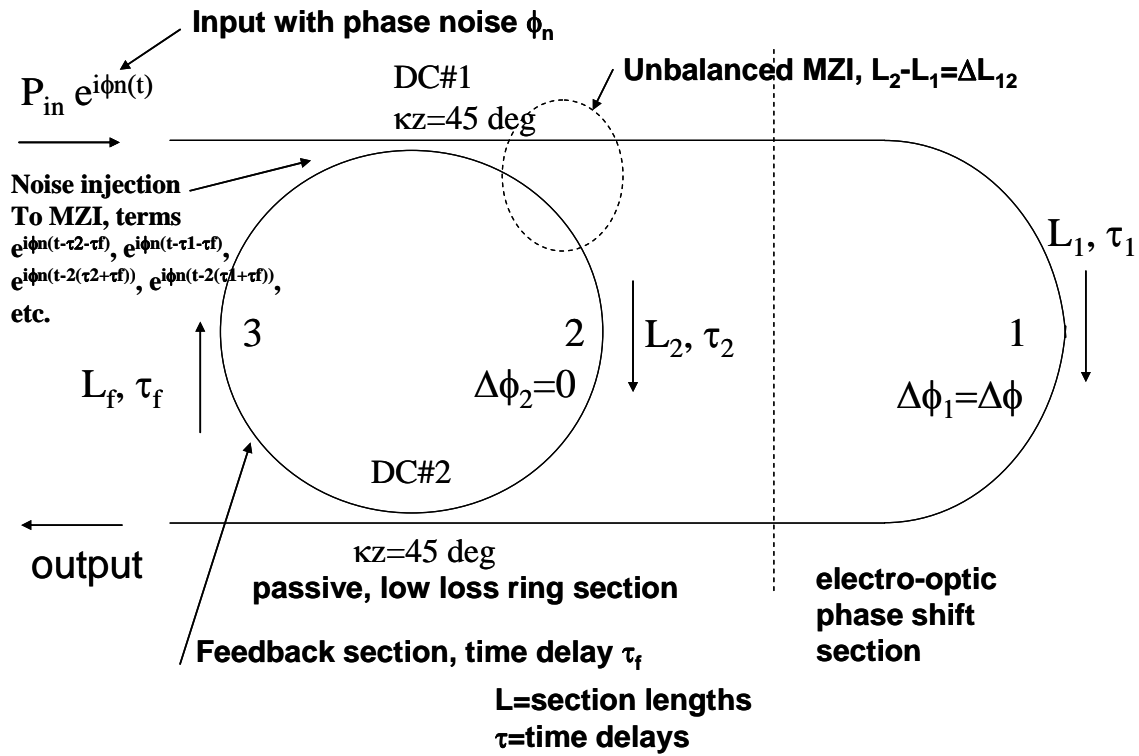


**Figure 81.** Detail of BBR identifying lengths, time delays and noise sources.

Intensity noise results from the conversion of laser phase noise in the BBR. Phase noise power builds up in resonant ring similar to power, but depends on time delays of paths,  $L_1$ ,  $L_2$  and  $L_f$ . These paths are represented in Figure 81. Shorter paths mean greater probability of noise components adding in phase, i.e. building up. Conversion of phase to intensity noise can occur at either directional coupler, if inputs are dephased. This noise conversion was observed in resonant rings in mid 80's.

We observed that the noise was much worse in JDS laser (<1MHz) than in the New Focus laser(<300kHz), due to wider linewidth as with measurements shown in Figure 82. Phase noise in unbalanced MZI is converted to intensity noise due to dephasing between arms. Phase fluctuation caused by frequency fluctuation  $\Delta\omega$  is represented as:

$$d(\Delta\phi) \sim (n\Delta L_{12}\Delta\omega) / c$$

Intensity fluctuation is represented as:

$$dI \sim \frac{I_{in}}{2} \sin(\Delta\phi) d(\Delta\phi)$$

This fluctuation causes intensity noise to increase with laser linewidth  $\Delta\omega$  and  $\Delta L_{12}$ .

The New Focus external cavity DFB laser has a narrower linewidth (<35 kHz) and less phase noise than the JDSU DFB chip with a linewidth of 3.5 MHz. Linewidth is the measure of phase noise present on the laser's output. The linewidths were measured in July 2005 with our Agilent 11980A and 70880A Automatic Linewidth Measurement System. The Agilent 11980A uses the self-homodyne technique to translate the spectral line from the terahertz region to 0 Hz. The noise measurements show that we desire a laser with a narrow linewidth.

## Noise Power vs. Frequency JDS(<1MHz) & New Focus(<300kHz) Lasers

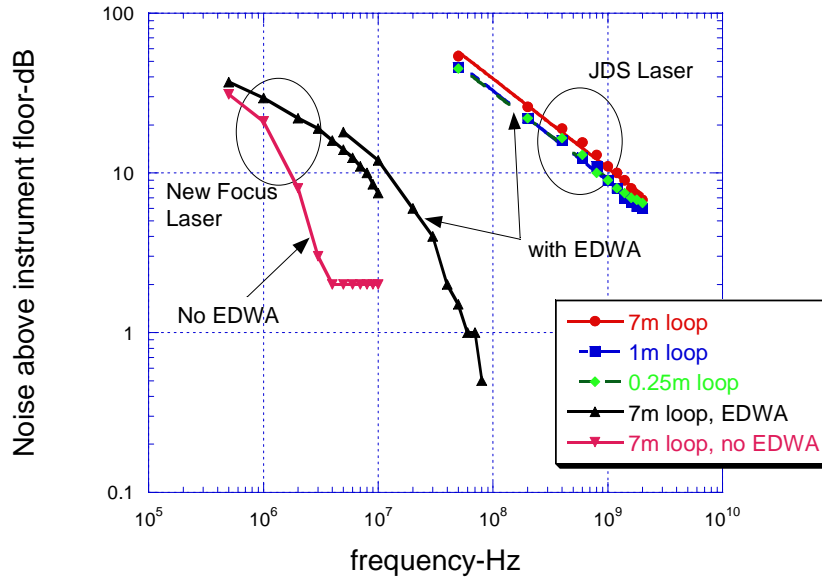


**Figure 82.** Noise power for two different linewidths and different unbalanced MZ lengths.

Figure 83 is a diagram of the BBR showing the micro-resonators and phase modulator sections. Figure 84 consists of modeled curves that demonstrate the design trades of the critical design parameters of the BBR; for example  $\alpha$ , ring loss,  $t_2$ ;  $t_1$  referenced in Figure 83. The improvement is modeled to show the enhancement in gain when the phase modulator is in a Mach-Zehnder as compared to being in a BBR configuration. The gain improves as the ratio of the optical transmission in the phase modulator to the optical transmission in the micro-resonator approaches 1 and as the optical throughput in each section approaches 1. Figure 85 is a variation of Figure 84 showing the improvement, decrease in  $V\pi$ , as a function of the optical loss in the phase modulator. A second resonator was purchased with the more ideal coupling coefficients as compare to the first. The “ $\perp$ ” marks the experimental data point related to the BBR with the second  $\mu$ -ring. This experimental result with the second ring was a  $V\pi$  improvement by a reduction factor of 0.14( $0.35V/2.5V \sim 0.14$ ).

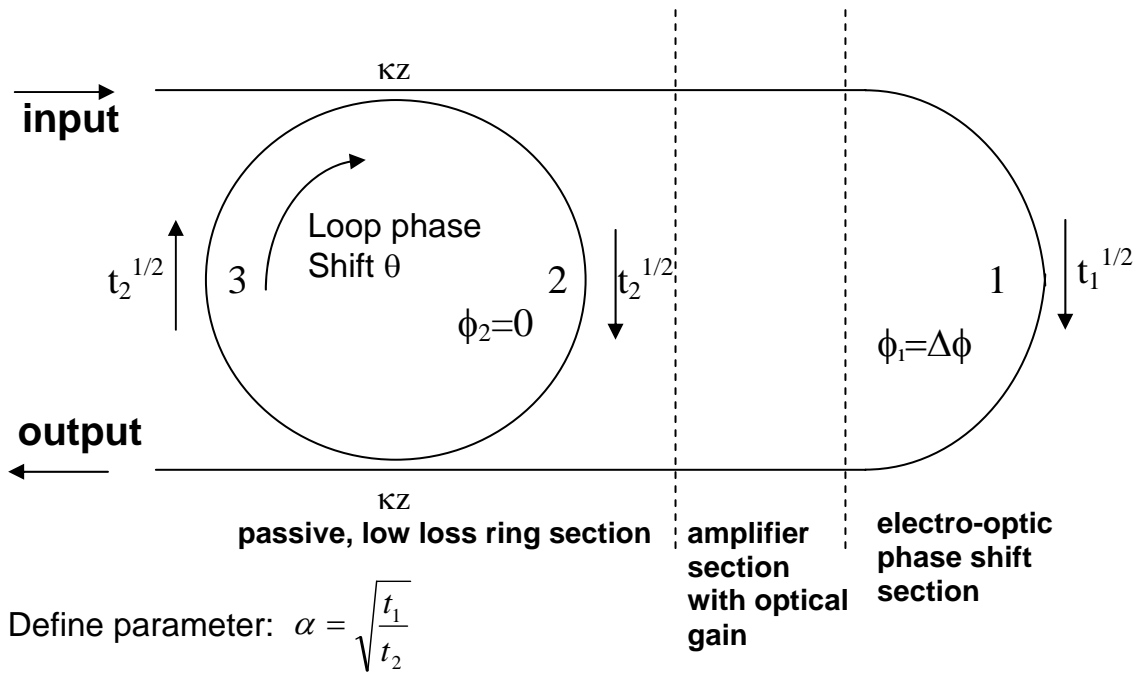


**Figure 83.** BBR modulator design.

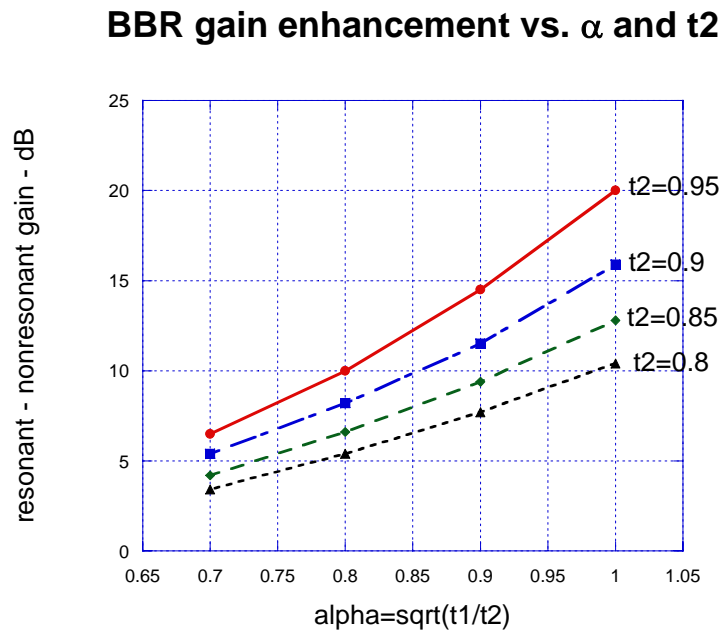


**Figure 84.** Available gain enhancement over regular MZI vs.  $\alpha$  and  $t_2$ . Assumes current LO ring design,  $kz=45\text{deg}$ .

### $V\pi$ Reduction Factor and estimated result with 2nd LO ring

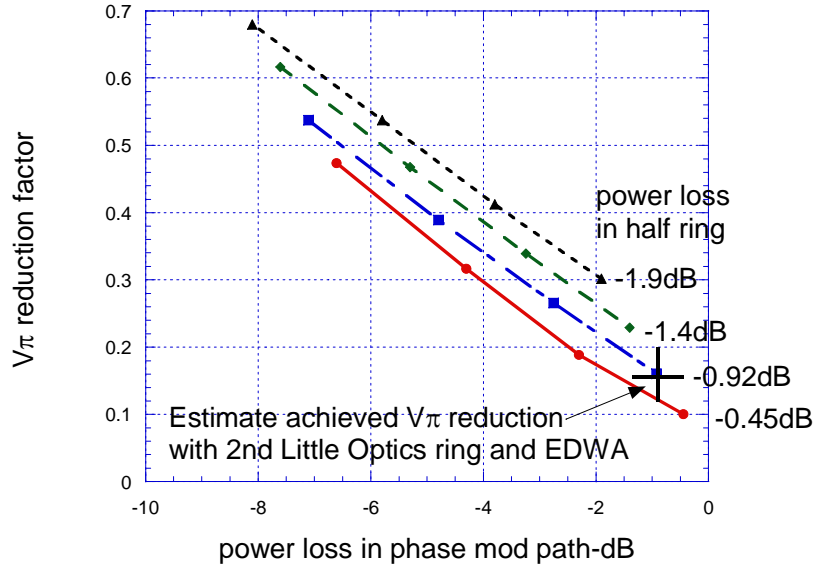


**Figure 85.**  $V\pi$  reduction factor with BBR vs. optical power losses.

We have demonstrated that models for BBR agree with experiment and low  $V\pi < 1.8V$  is achievable. Due to the unbalanced MZ, we observed phase to intensity noise conversion, from interference of periodically delayed signals. This noise can be reduced by reducing the laser linewidth. We also observed amplification was necessary to achieve good results due to losses in discrete component set-up, but that ring lasing modes add to noise. The ultimate design should not use an amplifier; therefore, very low loss material system is needed. Also, the combination of fiber loop and intensity noise does not allow bias stabilization. The device needs integration to achieve bias stability and demonstration of link performance.

### *BBR in LiNbO<sub>3</sub>*

At the same time the hybrid BBR was investigated, PSI pursued a BBR modulator in a standard configuration on a single lithium niobate wafer as shown in Figure 86. This system was not ideal, but was planned to provide more insight to the BBR before committing to the pursuit of the more expensive fully integrated BBR. Path lengths are large due to very large bend radius for lithium niobate. For low loss,  $R=25mm$  so the ring loop length is about 150mm and the outer

loop length is >80mm. The longer ring loop provides a modulator with repeated resonances every 800 MHz. Due to the low loss electrodes, the modulator should work well past 20 GHz.

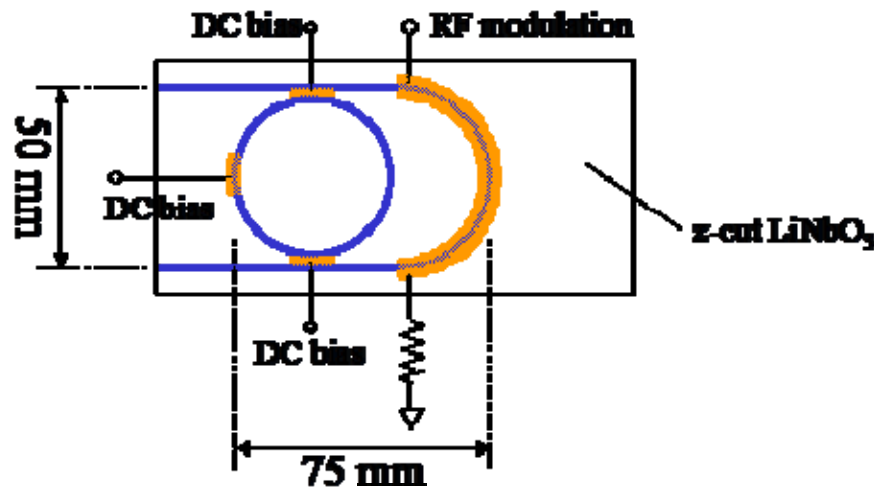


**Figure 86.** BBR in LiNbO<sub>3</sub>.

PSI contacted NRL concerning the fabrication of the BBR in the integrated ring in LiNbO<sub>3</sub> configuration. This was a new design for NRL and required new masks for both the electrodes and waveguides. NRL expressed enthusiasm in working with PSI and committed resources to the fabrication once they receive the appropriate funding. NRL was responsible for the following tasks:

- Generation of a detailed fabrication design
- Design and layout of photomask
- Procurement of photomasks
- Fabrication of prototype BBR modulators in LiNbO<sub>3</sub>
- Initial testing of prototype BBR

PSI viewed working with NRL as the opportunity with the least risk. PSI was eager to work with NRL and was impressed with the demonstrated NRL fabrication capabilities of 12 V\*cm V $\pi$  length product, 0.11 dB/cm loss in a straight waveguide and 0.3 dB loss for fiber coupling. The risk was further minimized in this design with the implementation of DC bias controls at the ring/straight waveguide coupler and in the ring waveguide to control the coupling into the ring and phase in the ring respectively.

The first version of the LiNbO<sub>3</sub> waveguide mask layout is shown in Figure 87 and Figure 88. These masks included:



- Diagnostics (straight channels and directional couplers, with and without electrodes) to section of mask with resonant ring only to independently get coupling, straight channel loss, and input output coupling loss to help with deconvolving ring loss measurement.
- Channels to convert non-resonant MZI to a 4-port device.

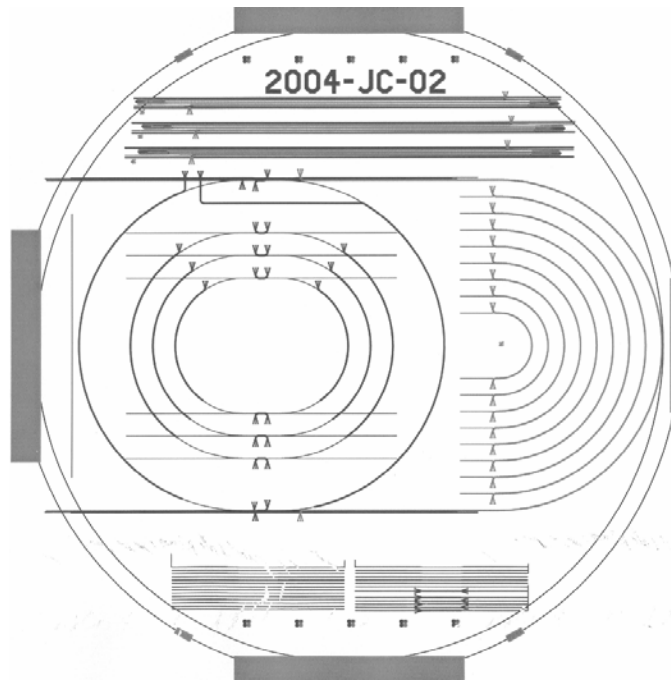


**Figure 87.** Mask layout of preliminary BBR.

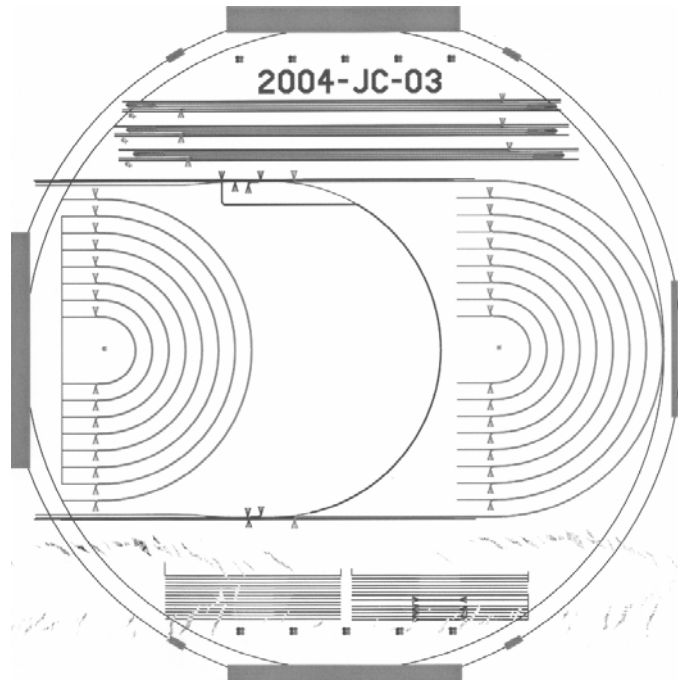


**Figure 88.** Mask layout of preliminary MZ with electrode length the same as the BBR.

Although there is an enhancement to the gain using a BBR in a link as compared to a Mach-Zehnder (MZ) of the same electrode length, both will suffer a roll off due to the electrode losses. Figure 90 shows the electrode loss as a function of frequency while Figure 75 relates how this loss will affect  $V\pi$  as a function of frequency.

The final design included a ridge waveguide and 47 Ohm RF electrode impedance. The expected thickness of the RF electrode was  $\sim 50\mu\text{m}$ . The RF electrode had the DC bias fed through a bias tee at the input and terminated with a bias tee so the user can control the resistive termination. Also planned was a low frequency thin plated electrodes for kappa trim and loop phase trim.

The final device was expected to be delivered in April 2005. During the period where NRL was attempting to fabricate the BBR, they were also changing from a 3" wafer fab facility to a 4" wafer fab facility. NRL experienced many setbacks with upgrading their equipment and never successfully fabricated a BBR. Since we had gained understanding of the BBR with the hybrid- $\mu$ -ring, and LiNbO<sub>3</sub> phase modulator, at a review in August 2005, it was decided to move on to the integrated hybrid BBR instead of continuing to fund the NRL effort.

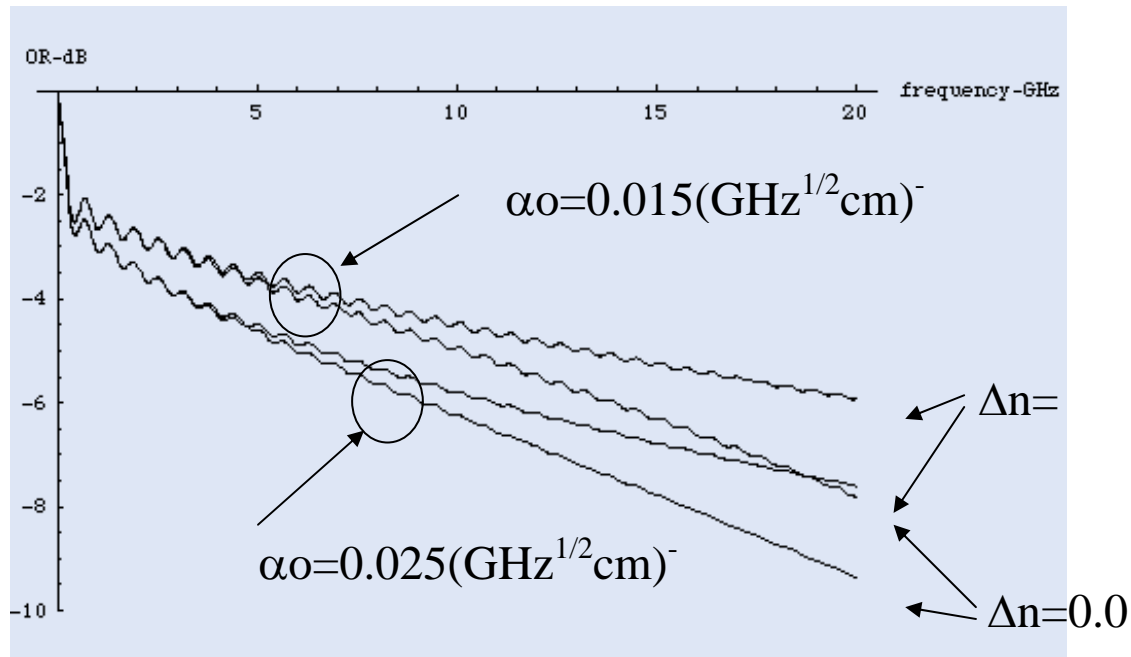


**Figure 89.** BBR frequency dependence (does not include effect of resonance) with  $V\pi L = 12$  Vcm,  $L = 11$  cm,  $a_1 = 0.0015(\text{GHz}\cdot\text{cm})^{-1}$ ,  $R = 35$  Ohms.

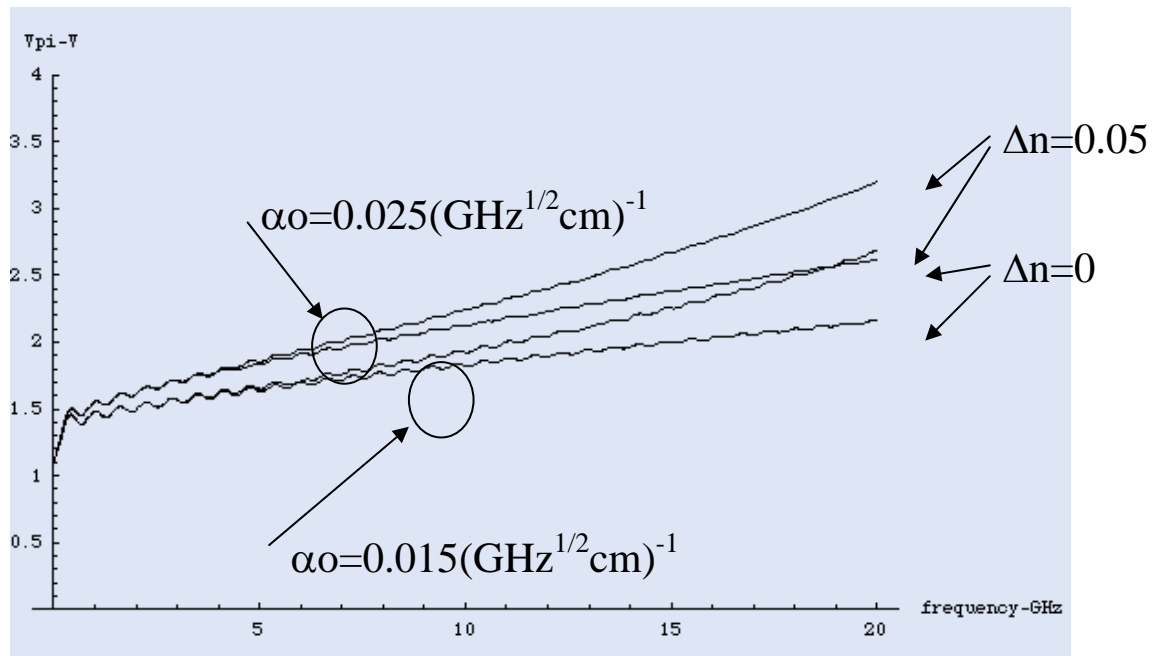


**Figure 90.**  $V_\pi$  vs. frequency (does not include effect of resonance  $\sim 0.6$  GHz).

### ***BBR – integrated hybrid***

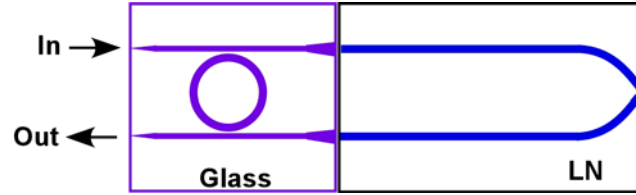


**Figure 91.** Integrated hybrid BBR

Gaining confidence in our understanding of a BBR based on our previous experiences, next PSI pursued an integrated hybrid BBR as shown in Figure 91. PSI developed a hybrid BBR with components that were butt coupled and packaged together. The integrated hybrid BBR consists of a ring resonator with coupling to input/output waveguides formed in glass, and an outer loop with electrodes formed in lithium niobate. The glass waveguides are tapered so the mode size matches fiber and lithium niobate modes as appropriate. The electrodes are placed on the outer loop on the lithium niobate. The electrodes can follow a curve or make a quick U-turn, so the interaction length can be nearly the full length of the outer loop.

In order to achieve a low  $V\pi$ , low optical insertion loss is required to allow for the resonance effect to take place. Major losses could occur between the glass and lithium niobate interface and the reflection/turnaround at the end of the lithium niobate. To make a low-loss ring with a bend radius of 0.2 mm, a high effective index compared to the substrate is required. This can be done with a material index difference of 0.05 and a waveguide width of 1.9  $\mu\text{m}$ , which are possible with glass. The critical coupling is to the lithium niobate because it is in the resonant outer loop. Lithium niobate has a mode size of about  $4 \times 8 \mu\text{m}$ . By using an adiabatic taper up to about 9  $\mu\text{m}$  width, the glass waveguide mode would become  $2.7 \times 8 \mu\text{m}$  which has a mode mismatch loss of only 0.3 dB. Thus the coupling loss would be about 1.0 dB (0.5dB for each the coupling for the outer loop). These numbers are not the result of an accurate model of glass waveguides, but they indicate that tapers to lithium niobate and fiber mode sizes are compatible with the same material index difference that is required for very tight bends. The lithium niobate vendor has proprietary techniques to minimize the optical loss of the turnaround.

The most important parameter to control when designing the BBR is optical insertion loss as previously stated. If the insertion loss is too high, the resonant effects are dampened. Emphasis was placed on minimizing the insertion loss. Figure 92 is a schematic of the components that contribute to the insertion loss. The phase modulator requires TM polarization of the light. The ring resonators have lower loss for TE but require lossy mode rotators to change the light to TM before the phase modulator if TE is used. Mode transformers are also in the ring resonator chip. These transformers have a shaped waveguide to minimize the mode mismatch between the

resonator chip and fiber. Table 4 summarizes the insertion loss of the BBR for two options of polarization in the ring resonator for the standard transformers. The transformers could also be designed to minimize the loss between the phase modulator and resonator chip. Minimizing this loss is more important than minimizing the fiber coupling loss.

Table 5 summarizes the insertion loss of the BBR for two options of polarization and the transformers designed to mode match to the phase modulator. Based on this analysis, the most promising option to minimize insertion loss was to use a specialized mode transformer without any mode rotators and accept the larger insertion loss of TM propagation in the ring resonator.

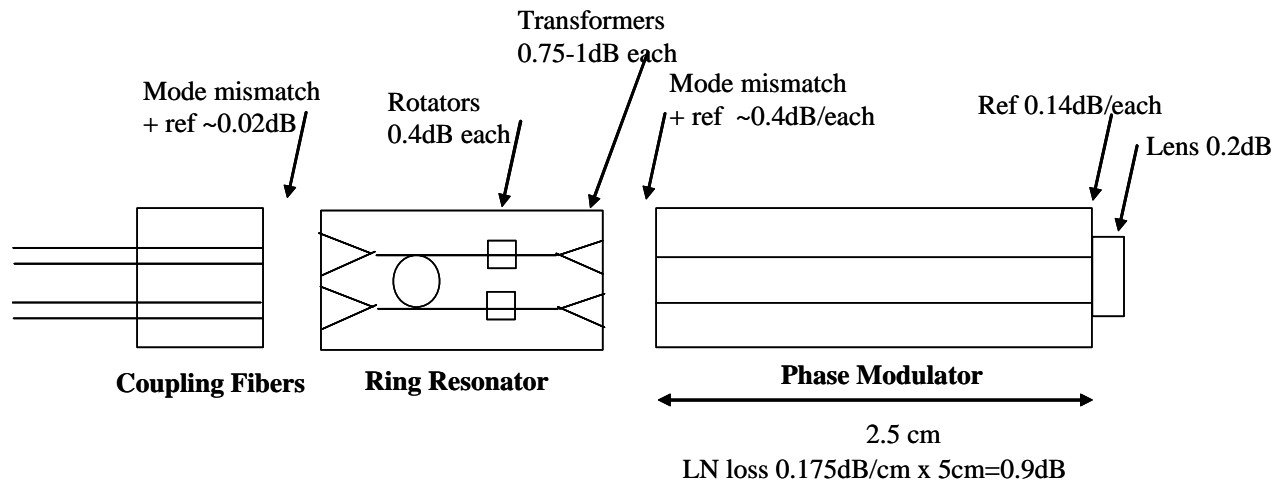


**Figure 92.** Loss budget- standard transformer,  $w_x=w_y=4.9\mu\text{m}$

**Table 4.** Loss budget for entire modulator- standard transformer,  $w_x=w_y=4.9\mu\text{m}$ .

	<u>TE-&gt;TM</u>	<u>TM</u>
2 rotators	0.8	0
2 transformers	1.5-2	1.5-2
2 Alignment loss	0-0.5	0-0.5
2 mode mismatch+ref.	0.8	0.8
Prop. Loss	0.9	0.9
Lens	0.2	0.2
2 Ref at lens	0.3	0.3
Total	4.5-5.5dB	3.7-4.7dB

**Table 5.** Loss budget for entire modulator- new transformer ,  $w_x=4.9\mu\text{m}$ ,  $w_y=3\mu\text{m}$ .

	<u>TE-&gt;TM</u>	<u>TM</u>
2 rotators	0.8	0
2 transformers	1.5-2	1.5-2
2 Alignment loss	0-0.5	0-0.5
2 mode mismatch+ref.	0.3	0.3
Prop. Loss	0.9	0.9
Lens	0.2	0.2
2 Ref at lens	0.3	0.3
Total	4-5dB	3.2-4.2dB

Figure 93 shows the gain enhancement of the BBR with the planned ring resonator of no mode rotators and redesigned mode transformers to reduce ring resonator chip/lithium niobate mode mismatch loss. Given the expected optical insertion loss, the reduction  $V\pi$  factor is  $10^{(-\text{gain}/20)}$ , or  $0.28=1/3.5$ , for 11dB gain enhancement. We planned to start with three different phase modulators with  $V\pi$ 's of 2.8V, 2.1V, and 1.7V, for 25, 30, and 35mm chip lengths respectively. Based on the gain enhancement, we calculated the  $V\pi$ 's of the integrated BBR to be 0.8, 0.6, and 0.5V. We supported the building of two integrated BBRs. Based on the performance of the three phase modulators, we down selected to two modulators for integration.

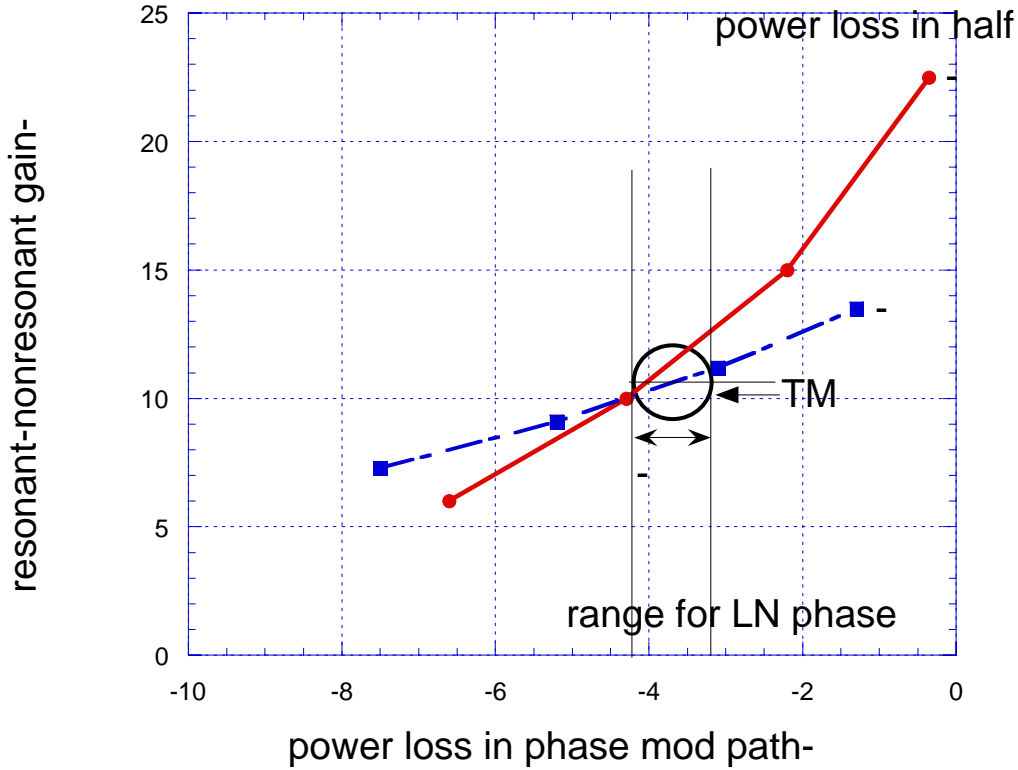


**Figure 93.** TM performance with new mode transformer to eliminate rotators, redesign mode transformers to reduce hydex/LN mode mismatch loss, TM operation only

As previously stated, the integration of the BBR included design and procurement of the phase modulator and  $\mu$ -ring resonator along with the integration of the two parts. The phase modulator was designed by PSI staff member, Bill Burns, an expert in  $\text{LiNbO}_3$  devices. To understand the tradeoff between lower  $V\pi$  of the phase modulator and higher insertion of the lithium niobate chip as length increases on the BBR, three chip lengths were fabricated of 25, 30, and 25 mm. A  $V\pi(\text{DC})$  of  $\sim 2.3\text{V}$  was expected in longest device (5.3mm electrode length).

Figure 95 shows a schematic of the ring resonator architecture. The chip consists of a single ring with a target Free Spectral Range (FSR) of 800 GHz, and a target ring-to-bus coupling strength of 50%. The circuit had input and output ports on both sides of the chip. Mode transformers at each port facilitated coupling to single mode fibers or to the modes of  $\text{LiNbO}_3$  waveguides. The

mode transformers were designed to give a spot size that had a radius of  $4.9\text{ }\mu\text{m}$  in the horizontal plane of the chip, and a radius of  $3.0\text{ }\mu\text{m}$  in the vertical direction, normal to the plane of the chip (mode radius defined as the  $1/e$  field point). A total of 5 ring designs were considered, which comprised the permutations of 5 coupling value splits of 40%, 45%, 50%, 55% and 60%. Ideally the target coupling value is 50%. The rings utilized new vertical coupling approach with a very low loss,  $t_2 \sim 0.97$  (.13dB). The mode transformers were designed to better match  $\text{LiNbO}_3$  mode asymmetry and for TM operation.

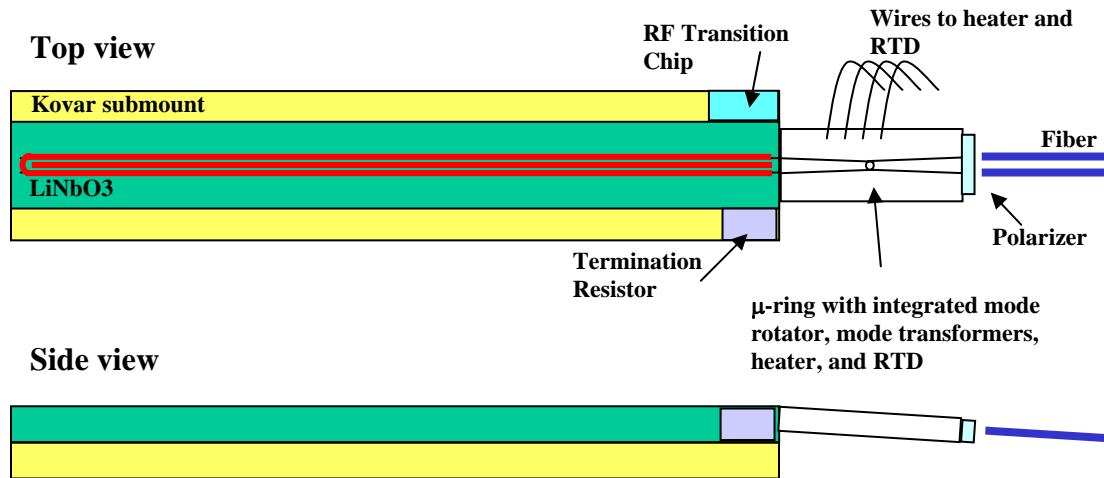


**Figure 94.** Schematic of a  $\text{LiNbO}_3$  chip co-packaged with a microring resonator chip.



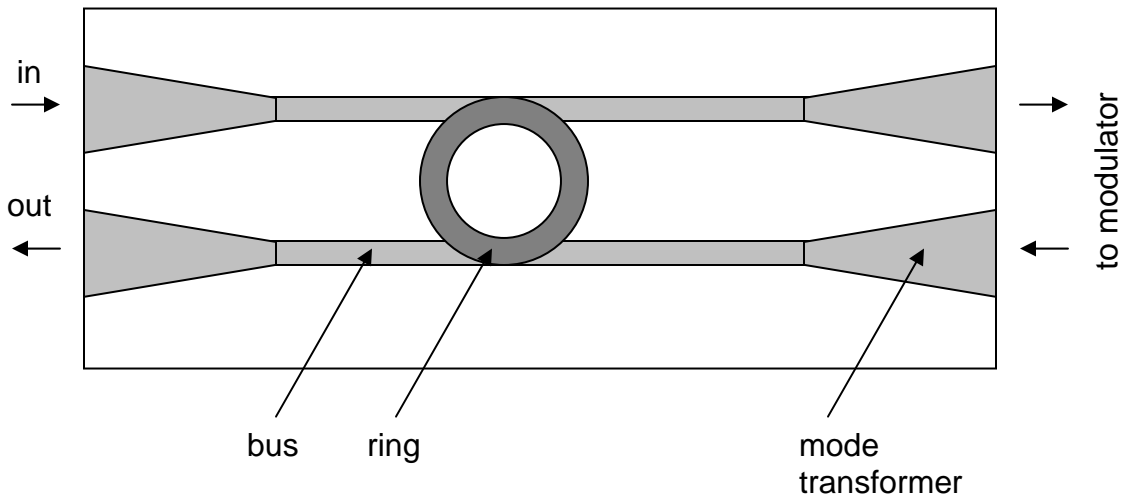


**Figure 95.** Schematic of a ring resonator chip having a single ring and dual sided input/output ports.

The co-packaging of a  $\text{LiNbO}_3$  modulator chip with a  $\mu$ -ring resonator chip is depicted in Figure 94. The modulator chip was mounted to a Kovar submount and had RF transmission and termination chips, and including turning mirror and possible polarizer. The chip was pigtailed to a pair of PM fibers, and then attached to the modulator chip. A vertical dice angle was used at the modulator-ring interface to suppress facet reflections. The submounted assembly was placed in a Kovar box (not shown in Figure 94) machined to accept RF K-connectors and other wire feed-throughs. A project box similar to Figure 75 housed an electronics board to control the ring thermal stability, while the Kovar modulator box, as shown in Figure 96, sat outside of the project box.

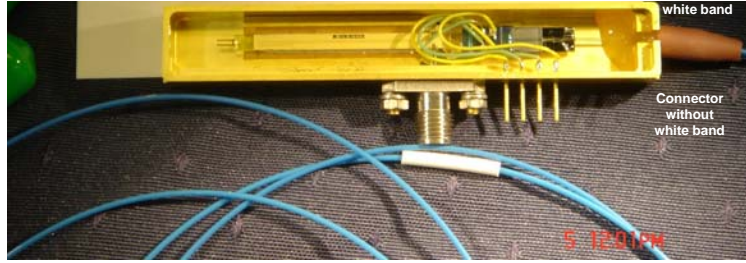


**Figure 96.** Broad bandwidth resonant modulator in an integrated package.

Both the first and second hybrid integrated BBR had a higher than expected  $V\pi$ . It was realized that the optical insertion loss in the phase modulator arm was greater than expected as summarized in Table 6 and Table 7. In Figure 97, the transfer function as a function of loss and phase is modeled for a MZ and the first and second BBRs assuming the same phase modulator  $V\pi$ . Just as expected, the 2<sup>nd</sup> BBR has the highest slope with its lowest insertion loss which results in an effective  $V\pi$  reduction of 15% as compared to the MZ. Using Equation 13 to model the gain in a modulator as related the transfer function, Figure 98 demonstrates the impact to gain of the higher insertion loss of the first BBR compared to the second BBR. The impact of the insertion loss on gain was verified as shown in Figure 99. Notice how the ripple decreases and losses decrease which is due to the effect of the resonance.

**Table 6.** Optical insertion loss tabulation in phase modulator only.

Fiber/LN/lens (double pass)

35mm chip, 4.1dB insertion loss measured

Fiber/LN mode mismatch loss (x2)	0.8dB
Fiber/LN reflection loss (x2)	0.3dB
Prop. Loss, 0.2dB/cm, 7cm	1.4dB
Reflection at lens (x2)	0.3dB
Reverse image mode mismatch loss	0.4dB
Lens defect loss – total	0.2dB
Fiber/lens alignment loss – total	<u>0.3dB</u>
Sum of contributions	3.7dB
Unaccounted for loss	<u>0.4dB</u>
Total insertion loss	4.1dB

**Table 7.** Optical insertion of phase modulator arm of BBR including coupling to ring.

Loss in phase modulator arm ( $t_1$ )

Ring/LN mode mismatch + ref (x2)	0.3dB
Prop. Loss, 0.2dB/cm, 7cm	1.4dB
Reflection at lens (x2)	0.3dB
Reverse image mode mismatch loss	0.4dB
Lens defect loss – total	0.2dB
Ring/LN/lens alignment loss-total	0.3dB
2 transformers	1.8dB
Unaccounted for loss	<u>0.4dB</u>
Total estimate for $t_1$	5.1dB

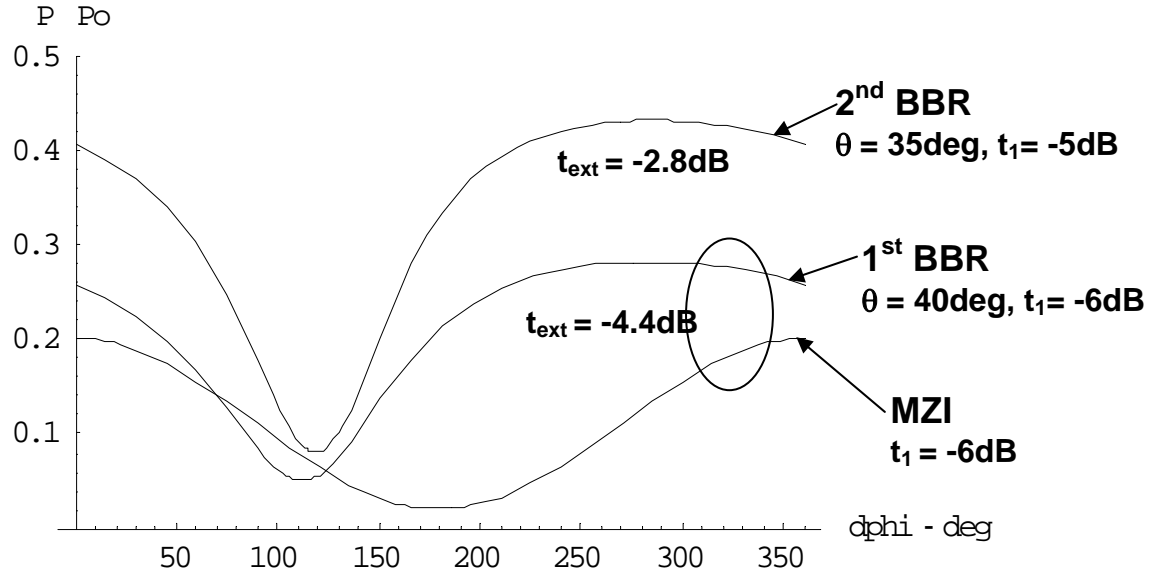


**Figure 97.** Modeled transfer functions MZ, 1st & 2nd BBR assuming the same phase modulator  $V\pi$ .

**Equation 13** 
$$Gain = 10 \log_{10} \left[ r P_{in} 10^{(dB/10)} \left| \frac{d\eta}{dV} \right|_{bias} \left( \frac{50 r_d}{r_d + 50} \right) \right]^2$$

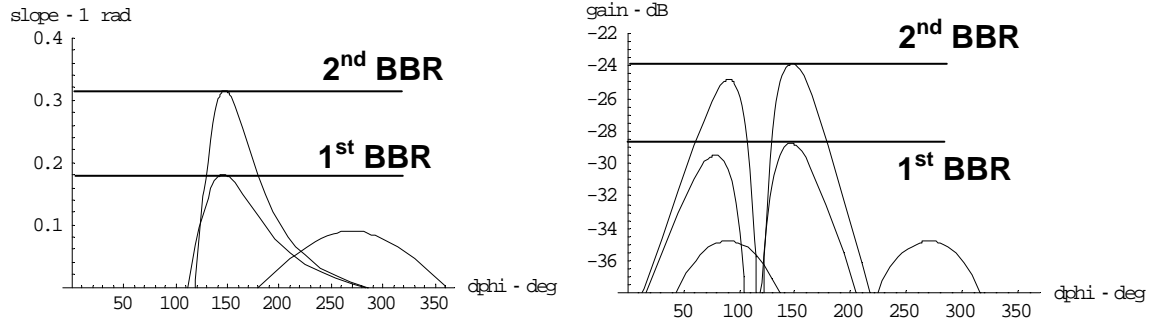


**Figure 98.** Modeled slope (left) and link gain (right) at 1.7GHz assuming  $P = 11.5\text{mW}$ ,  $RPD = 0.68\text{A/W}$ , and  $V\pi$  (large signal) = 3.1V .

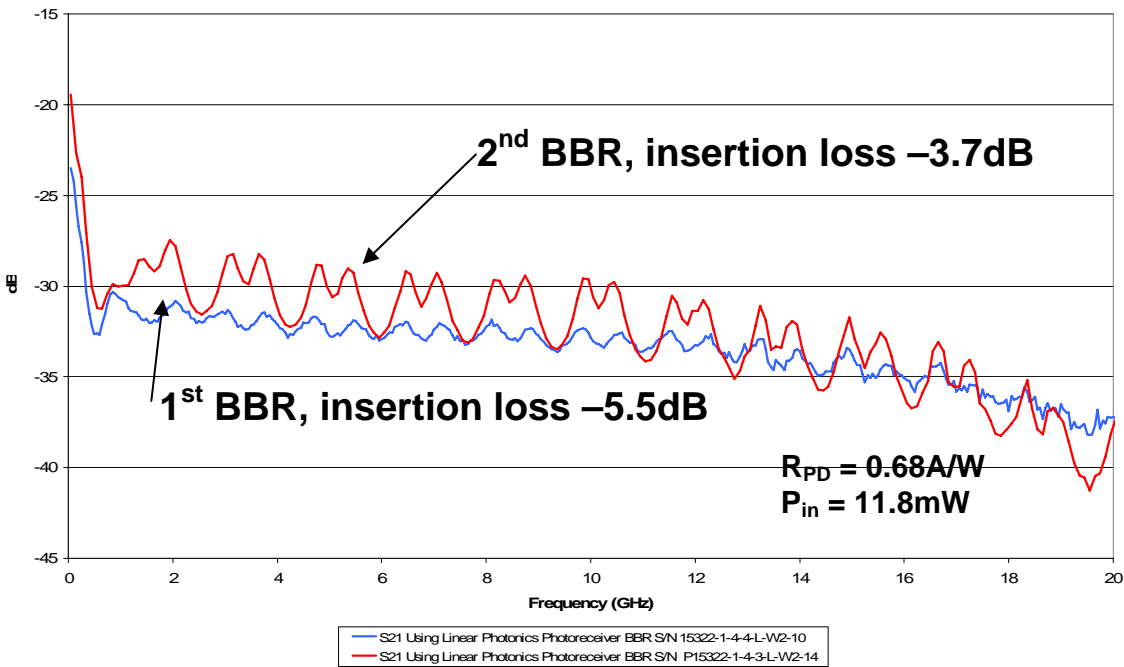


**Figure 99.** Small signal modulation link gain of 1st and 2<sup>nd</sup> BBR.

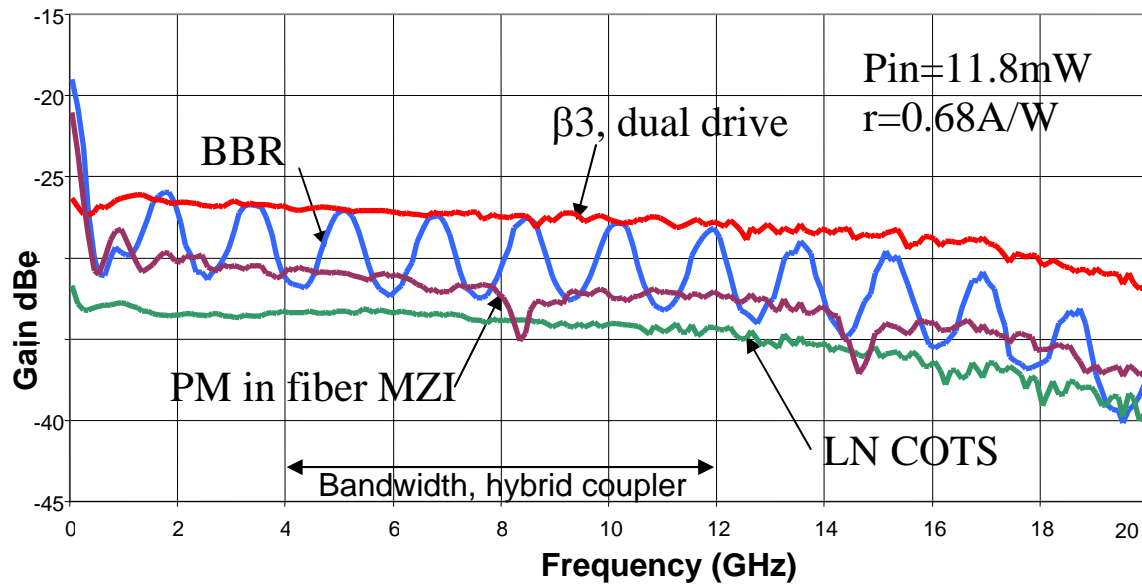


**Figure 100.** Relative measurement of link loss.

**Table 8.** Link gain and  $V\pi$  of BBR and MZI type devices.

	$V\pi_{\text{eff}}$ (V)	Insertion Loss (dB)	Gain/Model (dB)	Gain/Expt. (dB)
2nd BBR	2.7(1.7GHz)	3.7	-24	-26
ULTRA-beta3 dual drive	~0.9(1GHz)	7.6	-24.4	-26.3
LiNbO3 COTS MZ	5.2(1GHz)	4.5	-33.4	-32.8
Phase modulator - Fiber MZI	3.1(1.7GHz)	3.8	-27.4	-29.6

We also measured the gain of other external modulators using the same laser input power and same detector efficiency with the results shown in Figure 100 and summarized at specific frequencies in Table 8. Although the ULTRA-beta 3 modulator had the lowest  $V\pi$ , the optical insertion loss prevented it from having the highest gain. The 2<sup>nd</sup> BBR had the best gain performance of the available modulators.

### ***BBR modulation linearity***

An analysis was completed on a linearity comparison of the broad bandwidth resonant modulator (BBR) and the Mach Zehnder modulator (MZ). Often systems specify linearity with an intermodulation-free dynamic range (IMFDR) requirement. However, the IMFDR depends on the noise, bandwidth and distortion of the system. For our investigation, we calculated the third-order intercept point (IP3) for both the BBR and MZ, which is only a function of the distortion. The third-order intercept point is defined as the point where the linear extrapolation of the fundamental output curve as a function of the power in intersects with the third-order output curve.

A diagram of the BBR is shown in Figure 101. The BBR is a variant of the classical MZ design that combines features of a MZ and a ring resonator. We will show that, for this configuration, a very small (compared to  $\pi$ ) change in the interferometer phase,  $\Delta\phi$ , can switch the output state from on to off. Likewise the voltage required for on-off operation is very small compared to the traditional  $V\pi$  required for a conventional MZ.

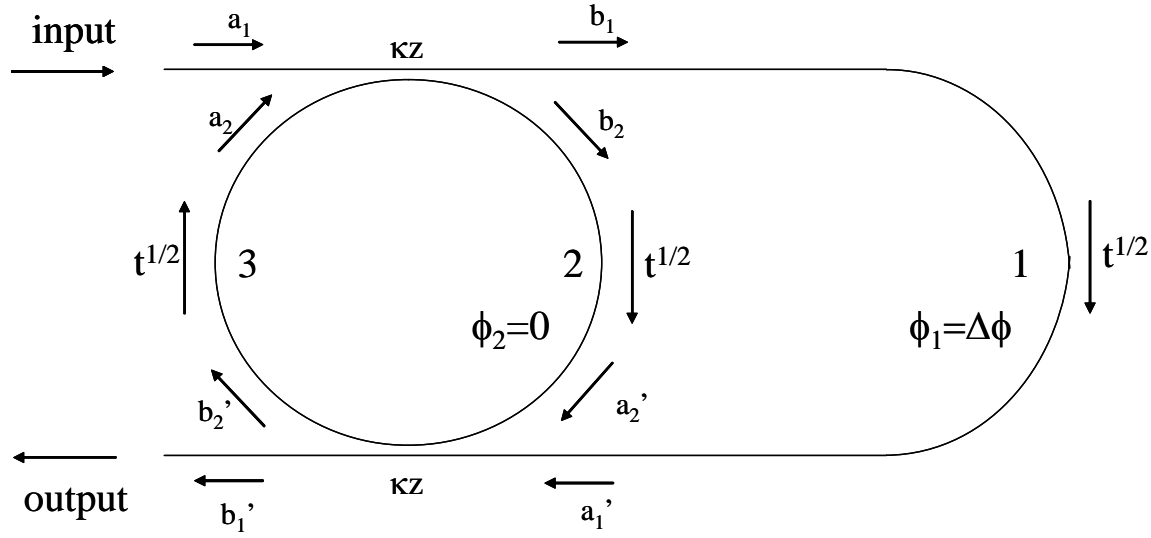


**Figure 101.** Broad bandwidth resonant modulator (BBR).

The transfer function of a modulator is described by the power out of the modulator as a function of the voltage applied. For modulators based on interference such as the MZ and BBR, the transfer function repeats every  $2\pi$  radians, therefore Figure 102- Figure 105 will be shown as a function of phase,  $\Delta\phi$  instead of applied voltage. The transfer functions for the MZ and BBR are shown in Figure 102 for modulators with the same phase modulator section. The amount of voltage required for a MZ to turn from on to off or maximum to minimum optical transmission is referred to as  $V\pi$ . Note the steeper slope of the BBR transfer function as compared to the MZ, or the  $\Delta\phi < \pi$  required to turn the BBR on-off.

To compare the performance of the BBR to the MZ, a  $V\pi_{\text{equivalent}}$  was defined based on a modulator transfer function. The transfer function (TF) of a MZ is:

**Equation 14** 
$$TF_{MZ} = \frac{1}{2} \left( 1 + \cos \left( \frac{\pi V}{V_\pi} \right) \right)$$

The maximum slope occurs when  $V = V\pi$ . The  $V\pi$  of the MZ is related to the slope of the transfer function as:

**Equation 15** 
$$\text{Slope} TF_{MZ} = -\frac{\pi}{2V_\pi}$$

To compare the on-off of the BBR to MZ, we have defined a  $V\pi_{\text{equivalent}}$  as:

**Equation 16** 
$$V_{\pi equiv} = Abs \left[ \frac{\frac{\pi}{2}}{MaxSlopeTF_{BBR}} \right]$$

The  $V_{\pi equiv}$  as a function of radians of the transfer function is shown in Figure 103 across the bias range of greatest interest. The  $V_{\pi equiv}$  is normalized to the MZ  $V_{\pi}$ . There are two regions where  $V_{\pi equiv}$  is  $<1$ , that is the  $V_{\pi}$  of the BBR is enhanced when compared the MZ. This reduction in  $V_{\pi}$  is the reason the BBR is being pursued by PSI in the DARPA RFLICs program.

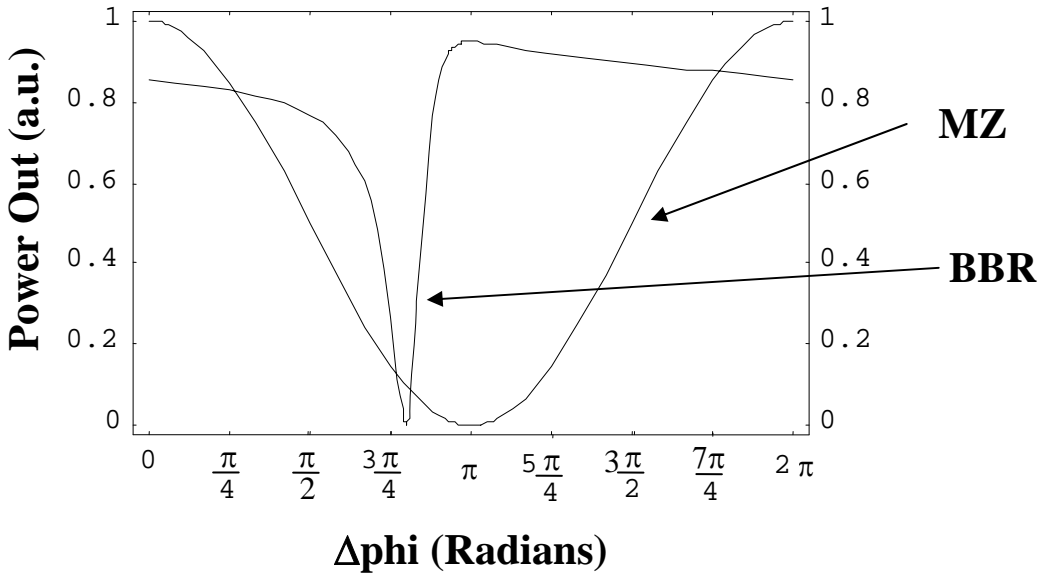


**Figure 102.** The transfer functions of the Mach-Zehnder modulator (MZ) and the Broad Bandwidth Resonant Modulator (BBR).



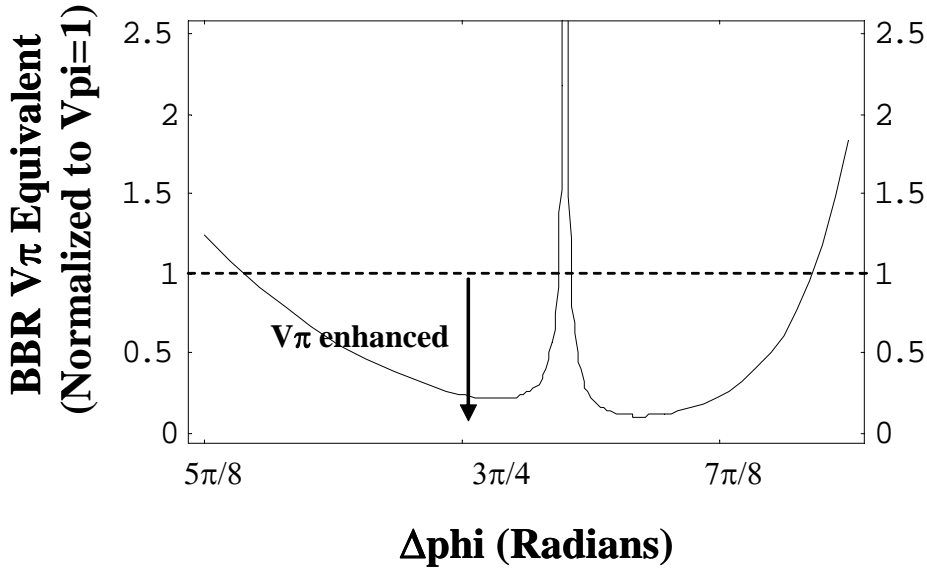


**Figure 103.** Equivalent  $V\pi$  of the BBR, normalized to that of an MZ modulator.

The IP3 of an external modulation link can be described as:

$$\text{Equation 17} \quad IP3_{IN} = \frac{2}{3R_m} \left| \frac{g_1}{g_3} \right|$$

where  $R_m$  is the resistance of the modulator electrodes and  $g_n$  is the  $n$ th term of the series expansion of the current at the detector as a function of applied voltage where

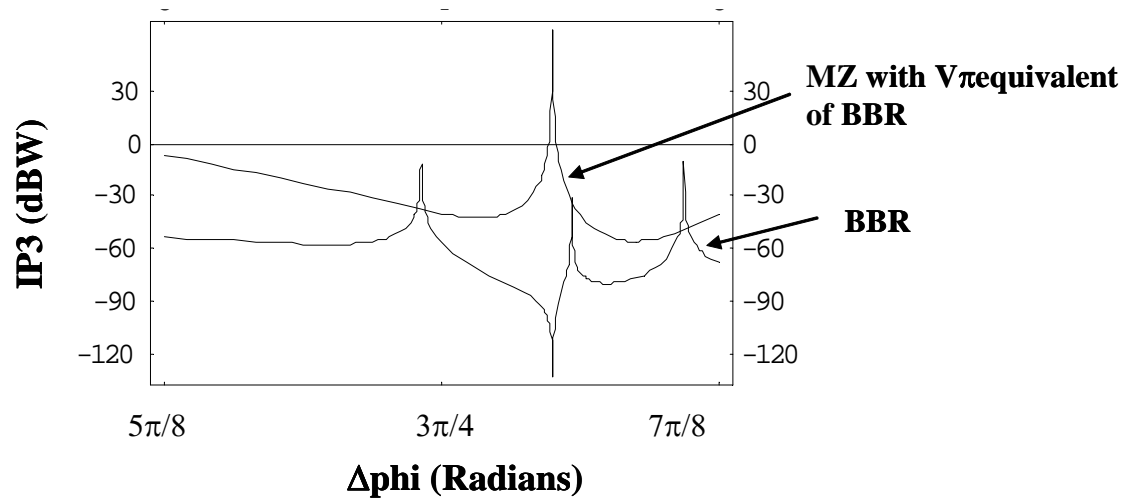
$$\text{Equation 18} \quad g_n = \frac{1}{n!} \left( \frac{d^n i}{dV^n} \right)$$

For a MZ modulator,  $IP3_{IN}$  simplifies to

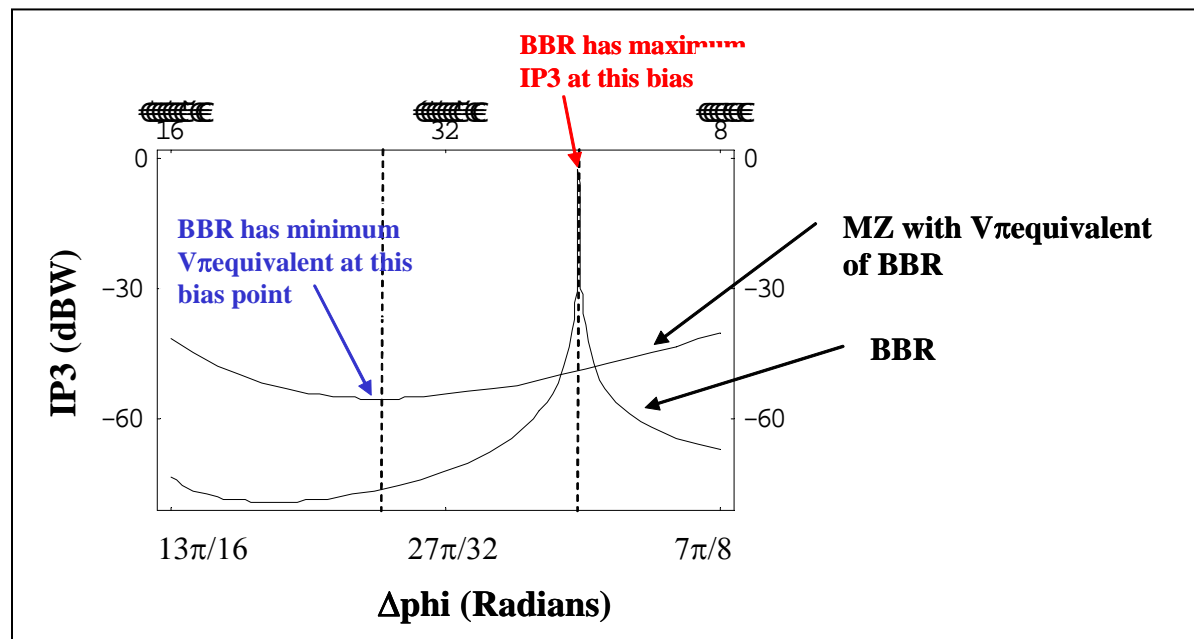
$$\text{Equation 19} \quad IP3_{IN\_MZ} = \frac{4V_\pi^2}{\pi^2 R_m}$$

Figure 104 shows the IP3, the solution to equation 4, for the BBR as a function of  $\Delta\phi$  over the same range of interesting  $\Delta\phi$  values as in Figure 103. The other curve labeled MZ in Figure 104 is derived from Equation 6 by replacing the  $V\pi_{\text{equivalent}}$  from Figure 103 for  $V\pi$ . At two bias points in this region of  $\Delta\phi$ , the IP3 is better for the BBR as compared to the MZ. These local maxima of IP3 for the BBR does not occur exactly at the bias point where  $V\pi$  is minimal, but do both occur where the  $V\pi$  is enhanced as compared to the MZ. Figure 105 shows the same data as in Figure 104, with the scale of  $\Delta\phi$  changed to emphasize the region around the best

operating points for the BBR. For applications where linearity is more important than smallest  $V\pi$ , the BBR may be the superior option as compared to the MZ.



**Figure 104.** Third order intercept point (IP3) of the MZ as a function of radians or applied voltage, and of an MZ having the same  $V\pi_{\text{equivalent}}$ .



**Figure 105.** Third order intercept point (IP3) of the MZ as a function of radians or applied voltage over a smaller range than Figure 106, and of an MZ having the same  $V\pi_{\text{equivalent}}$ .

### 3.4 Conclusions

Photonic Systems developed a Broad-Bandwidth Resonant Modulator, in which two low-loss optical resonators act as a lever to reduce the effective  $V\pi$  by 25% for a  $V\pi=2.7$  V of the interferometric optical intensity modulation process relative to the  $V\pi$  of the optical phase modulator embedded within one of the two resonators. The integrated BBR showed good stability which allowed it to be biased like other modulators. The  $\mu$ -ring heater provided good thermal stability. Operation with the PSI bias controller reduced ripple amplitude while maximizing average peak response. To improve the performance of the integrated BBR, loss reduction is required in the phase modulator and the interface between the phase modulator and  $\mu$ -ring. Although the ring performance was good, the overall integrated loss was too high for significant  $V\pi$  reduction-function of both losses and mode mismatch. This reduced loss could be obtained by three different methods. First, ridge waveguides could be used to decrease the VL product. This has a potential of reducing  $V\pi$  by 20%. Also, the waveguides could have less loss with Mg doping. The second loss reduction could come from using other materials such as  $\text{SiO}_2$  or polymers. Finally, just as demonstrated by PSI in this program, an optical amplifier internal to the BBR can overcome the loss of the phase modulator.

Configuration	Objective	$V_p$	Bandwidth	Bias Controllability
<b>All fiber breadboard</b>	<b>1st experimental confirmation of BBR</b>	<b>1.8 V</b>	<b>200 MHz</b>	<b>Low</b>
<b>Hybrid Micro-ring</b>	<b>Demo of wide bandwidth</b>	<b>3.4 V</b>	<b>15 GHz</b>	<b>Low</b>
<b>Integrated Ring in LiNbO3</b>	<b>Demo of low <math>V_p</math></b>	<b>Unknown</b>	<b>Unknown</b>	<b>Unknown</b>
<b>Hybrid Micro-ring with EDWA</b>	<b>Demo of wide bandwidth</b>	<b>1.8 V</b>	<b>15 GHz</b>	<b>Low</b>
<b>Integrated Hybrid Microring</b>	<b>Demo of low <math>V_p</math> and wide BW</b>	<b>2.7 V</b>	<b>15 GHz</b>	<b>High</b>

We have demonstrated that models for BBR agree with experiment and low  $V\pi < 1.8$  V is achievable with an EDWA in the BBR.  $V\pi$  enhancement of  $< 1$  V in this system (lithium niobate/glass) is unlikely to be achieved without optical amplifier. Low loss is needed to get resonance and a strong resonance is needed to get significant  $V\pi$  enhancement. The  $\mu$ -ring works well, but losses in the  $\text{LiNbO}_3/\text{glass}$  system are high which limits  $V\pi$  enhancement. No

modulators available today can reach the RFLICs goal of achieving a  $V\pi$  in the range of 0.1-0.5 Volts which would result in zero RF insertion loss with the 1-10 mW of optical power available from conventional laser diode sources. Figure 106 shows the optical insertion loss must be of the order of 2 dB in the phase modulator arm in order to achieve a  $V\pi < 1V$ . Although decrease in optical loss can occur as previously discussed, to achieve the low loss of less than 2 dB, an optical amplifier would need to be part of the phase modulator arm.

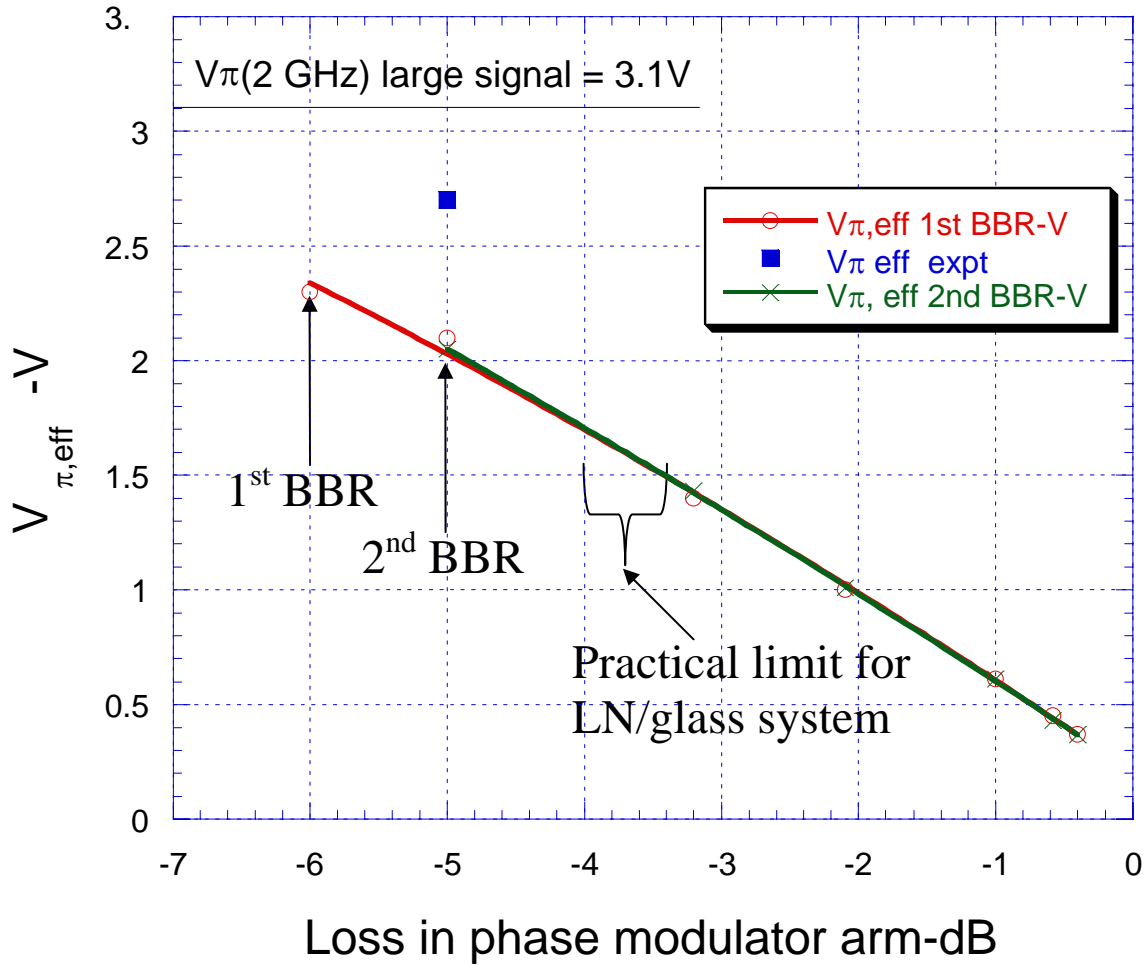


**Figure 106.** Model for  $V_{\pi, \text{eff}}$  vs.  $t_1$  (phase modulator arm loss) at 2 GHz.

## Appendix A - Published papers/Conference presentations

C. Cox, E. Ackerman, "The Role of Photonics in Future Phased Array Antennas – Keynote Address," *Workshop on Beamforming Technology and Applications*, July 26-27, 2000.

E. Ackerman, C. Cox, "Effect of Pilot Tone-based Modulator Bias Control on External Modulation Link Performance," *International Topical Meeting on Microwave Photonics (MWP 2000)*, September 11, 2000.

Photonic Systems, MIT, Sarnoff Corporation, and Columbia University, "High-Performance Analog Optical Links," *DARPA Optoelectronics Review*, October 16, 2000.

C. Cox, E. Ackerman, "Steps to the Photonic Antenna," *Analog Optical Signal Processing (AOSP) Study Group (DARPA/MTO)*, December 6, 2000.

R. Ram, C. Cox, "High Performance Microwave Optical Links," *International Conference on Communications, Computers, and Devices*, December 14-16, 2000.

C. Cox, E. Ackerman, "Photonics for Phased Array Systems (Invited Tutorial)," *IEEE Antennas and Propagation Society Meeting*, July 10-13, 2001.

C. Cox, E. Ackerman, "Photonics for RF Applications: Antenna Remoting, Photonics ADCs and Beamforming (Invited Tutorial)," *IEEE Gallium Arsenide Integrated Circuit Symposium (GaAs IC Symposium)*, October 21, 2001.

C. Cox, E. Ackerman, "Microwave Optical Links: Models, Measures, and Limits of Performance (Invited Tutorial)," *International Topical Meeting on Microwave Photonics (MWP)*, January 7-9, 2002.

C. Cox, E. Ackerman, "Microwave Photonic Links: Models, Measures and Limits of Performance (Invited Tutorial)," *Government Microcircuits Applications Conference (GOMAC)*, March 11, 2002.

C. Cox, "High Performance Analog Optical Links," *Government Microcircuits Applications Conference (GOMAC)*, March 12, 2002.

I. Gheorma, R. Osgood, "Fundamental limitations of optical resonator based high-speed EO modulators," *IEEE Photonic Technology Letters*, vol. 14, issue 6, pp. 795-797, June 2002.

T. Izuhara, R. Osgood, A. Roy, H. Bakhru, "Channel waveguides in thin films BaTiO<sub>3</sub> for low voltage TE/TM converter," *Conference of Lasers and Electro-Optics '02*, 2002.

C. Cox, "Design of broadband electro-optic modulator with very low  $V(\pi)$ ," *Government Microcircuits Applications Conference (GOMAC)*, March 31, 2003.

J. Prince, E. Ackerman, C. Cox, "Analog fiber-optic link technology," *Biophotonics/Optical Interconnects and VLSI Photonics/WBM Microcavities, 2004 Digest of the LEOS Summer Topical Meetings*, June 28-30, 2004.

W. Burns, F. Makrides, J. Prince, and C. Cox, "Design, Fabrication, and Measurements on a Broad Bandwidth Resonant (BBR) Modulator," *DARPA Meeting on RF Photonics*, August 8, 2006.

## ***Appendix B - List of Symbols, Abbreviations, and Acronyms***

ARROW – AntiResonant Reflector Optical Waveguide  
CW – continuous wave  
DBR – distributed Bragg reflector  
dqe – differential quantum efficiency  
I-V – Current-Voltage  
MIT – Massachusetts Institute of Technology  
MOCVD - Metalorganic Chemical Vapor Deposition  
PSI – Photonic Systems, Incorporated  
RF – radio frequency  
RFLICs – RF Lightwave Integrated Circuits  
SIMS – secondary ion mass spectroscopy  
UCSB – University of California at Santa Barbara  
UIUC – University of Illinois at Urbana-Champaign  
VCSEL – vertical cavity surface-emitting laser

## Appendix C - References

- 
- <sup>1</sup> C. Cox, H. Roussel, R. Ram, and R. Helkey, "Broadband, directly modulated analog fiber optic link with positive intrinsic gain and reduced noise figure," *Proc. IEEE International Topical Meeting on Microwave Photonics* (Princeton, New Jersey), 1998.
- <sup>2</sup> Y. Yamamoto, N. Imoto, *IEEE J. Quantum Electron.* **22**, 2032-2042 (1986).
- <sup>3</sup> Y. Yamamoto, S. Machida, *Phys. Rev. A* **35**, 5114-5130 (1987).
- <sup>4</sup> G. Bjork, *Phys. Rev. A* **45**, 8259-8267 (1992).
- <sup>5</sup> F. Rana, R. Ram, *Appl. Phys. Letts.* **76**, 1083-1085 (2000).
- <sup>6</sup> S. G. Patterson, G. S. Petrich, R. J. Ram, L. A. Kolodziejiski, *Electron. Letts.* **35**, 395-397 (1999).
- <sup>7</sup> E. Goobar, A. Karlsson, G. Bjork, P-J. Rigole, *Phys. Rev. Lett.*, Jan. 1993, **70**, pp. 437-440.
- <sup>8</sup> L. A. Coldren, S. Corzine, *Diode Lasers and Photonic Integrated Circuits*, John Wiley and Sons, New York (1995).
- <sup>9</sup> S. Machida, Y. Yamamoto, *Optics Lett.* **14**, 1045-1047 (1989).
- <sup>10</sup> Y. Yamamoto, H. A. Haus, *Phys. Rev. A* **45**, 6596-6504 (1992).
- <sup>11</sup> F. Jeremie, C. Chabran, P. Gallion, *J. Opt. Soc. Am. B* **16**, 460-64 (1999), *Appl. Phys. Lett.* **75**, 3614-3616 (1999).
- <sup>12</sup> L. Mawst, D. Botez, and C. Tu, *IEEE Photon. Technol. Lett.*, **4**, 11, (1992).
- <sup>13</sup> W. Burns, M. Howerton, and R. Moeller, "Broadband unamplified optical link with RF gain," *Proc. Photonics Systems for Antenna Applications Conf.* (Monterey, California, 1999).
- <sup>14</sup> E. Gordon and J. Rigden, "The Fabry-Perot electrooptic modulator," *Bell Sys. Tech. J.*, vol. 42, pp. 155-179, 1963.
- <sup>15</sup> C. Barron, C. Mahon, B. Thibeault, G. Wang, J. Karin, L. Coldren, and J. Bowers, "Asymmetric Fabry-Perot modulators with millimeter-wave (37GHz) frequency response," *Proc. 51<sup>st</sup> Annual Device Research Conf.*, pp. 233-234 (1993).
- <sup>16</sup> E. Gordon and J. Rigden, "The Fabry-Perot electrooptic modulator," *Bell Sys. Tech. J.*, vol. 42, pp. 155-179, January 1963.
- <sup>17</sup> M. Born and E. Wolf, *Principles of Optics*, New York: Pergamon Press, 1980.
- <sup>18</sup> I. Gheorma, R. Osgood, "Fundamental limitations of optical resonator based high-speed EO modulators," *IEEE Photonic Technol. Lett.*, vol. 14, issue 6, pp. 795-797, June 2002.